Modelling tokamak power exhaust and scrape-off-layer thermal transport in high-power fusion devices

MICHAEL ROBERT KNOX WIGRAM

Doctor of Philosophy

University of York

Physics

December 2019

Abstract

Managing the steady-state power loading onto the divertor target plates remains a major unresolved challenge facing tokamak fusion energy, that will be crucial for the success of the next generation of high-power reactor-level devices. This thesis will tackle two topics within this wide research area: assessing the performance of advanced divertor geometries in the context of the ARC reactor concept, and studying the impact of 'nonlocal' thermal transport on modelling predictions for the ITER tokamak SOL.

Numerical simulations are performed using UEDGE for the Super-X divertor (SXD) and X-point target divertor (XPTD) configurations proposed for the ARC reactor design. The SXD, combined with 0.5% fixed-fraction neon impurity concentration, produced passively stable, detached divertor regimes for power exhausts in the range of 80-108 MW. The XPTD configuration is found to reduce the strike-point temperature by a factor of $\sim$10 compared to the SXD for small X-point radial separations ($\sim 1.4\lambda_{q||}$). Even greater potential reductions are identified for separations of $\leq 1\lambda_{q||}$. Raising the separatrix density by a factor 1.5, stable detached divertor solutions were obtained that fully accommodate the ARC exhaust power without impurity seeding.

In the presence of steep temperature gradients, classical local transport theory breaks down, and thermal transport becomes nonlocal, depending on conditions in distant regions of the plasma. An advanced nonlocal thermal transport model is implemented into the 'SD1D' complex SOL code to create 'SD1D-nonlocal', and applied to study typical ITER steady-state conditions. Results suggest that nonlocal transport effects will have importance for the ITER SOL, with discrepancies observed between nonlocal/local transport model predictions in low-density scenarios. Heat flux models employing global flux limiters are shown to be inadequate to capture the spatially/temporally changing SOL conditions. An analysis of SOL collisionality and nonlocality suggests nonlocal effects will be significant for future devices such as DEMO and ARC as well.

Contents

List of Tables

List of Figures

Acknowledgments

This thesis and the research presented within it would not have been possible without the invaluable contributions of many of my collaborators and colleagues, in terms of the opportunities, assistance and support they gave to me throughout the course of my PhD. I would like to express my sincerest thanks and gratitiude to all of them, to whom I owe a great debt. Firstly, a deep thanks goes to my parents - Brian and Glynnis - who have supported and encouraged me greatly throughout this PhD, and continue to do so. It is unlikely I could have achieved what I have been able to without their continuous support and influence over the years.

One of the greatest opportunities I've had in my PhD was being able to visit and work with the team at the MIT Plasma Science and Fusion Center, who permitted me to work on modelling the divertor for their ARC reactor design, initially as a 10-week collaboratory project that then evolved into a longer collaboration in which much was achieved. This was only possible thanks to efforts of Dr Brian LaBombard, Dr Maxim Umansky and Prof Dennis Whyte, who enabled this project to go ahead and supported it throughout. I owe great thanks to Dr Brian LaBombard for effectively taking me on as one of his students and the excellent supervision he provided me in this project, that ensured rapid progress to meet deadlines in a short period of time, and from whom I greatly expanded my knowledge of MCF and the tokamak SOL. I thank Dr Maxim Umansky for all the training, support and expertise he provided for using the UEDGE code, fundamental for the project to be possible and without which could not have progressed as quickly nor achieved the extensive results that it did. I also thank Maxim for hosting me at LLNL for the UEDGE training, and for enduring my endless emails of UEDGE questions and issues since leaving the lab. And I thank Prof Dennis Whyte, who was my first contact at MIT, for enabling the project to go ahead in the first place. Thanks is given to the rest of the team also at the MIT PSFC who were involved - Drs Adam Kuang, Ted Golfinopolous, Jim Terry, Dan Brunner and others - for supporting the project with their knowledge and interesting discussions. The trips to MIT and LLNL and the continued collaboration thereafter were fantastic, both academically and personally, and will stay with me long into the future.

I thank my supervisor, Dr Christopher Ridgers, to whom I owe the opportunity to pursue

this PhD and research, for his guidance and encouragement over the last 4 years. Despite the trials and setbacks encountered in the projects, Chris endured my pessimisim when little appeared to be going right and remained positive and encouraging about my work throughout, which proved a great help in keeping myself positive and moving forward. I also thank Chris for the many interesting and enjoyable non-physics conversations we had over a wide range of topics, that were a welcome break from the PhD stresses and created a friendly atmosphere that I may not have had with another supervisor. I thank my co-supervisor Dr Benjamin Dudson for all his support in using BOUT++, integrating the Ji-Held model into SD1D for the project and helping solve my issues with the code, and for always being happy to help and discuss when I dropped by his office with questions. I give thanks to Prof Bruce Lipshultz for the interesting and useful discussions he provided for both the ARC divertor modelling and ITER nonlocal transport studies, and for the support he gave towards the work. And I'm grateful to both Dr John Omotani and Dr Jonathan Brodrick for their support in using and interpreting the Ji-Held model code in BOUT++.

And finally, a special thanks is given to Alan Sykes and Dr David Kingham of Tokamak Energy, and to Prof Richard Majeski of PPPL, who gave me my first opportunities in the world of fusion years ago through undergrad internships, that set me down the path to where I am today.

Declaration

The research presented in this thesis is my own, but certain work performed in support of these studies was carried out by other researchers. It is important to identify these contributions, and as such the work performed by others will be stated here, as well as at the relevant locations in the thesis text. For the ARC divertor modelling work in Chapter 5, the ARC MHD equiliria data required to produce the SXD and XPTD grids in UEDGE was generated by Dr Brian LaBombard using the ACCOME solver. The conversion of the resulting ARC MHD equilibria data to UEDGE format was performed by Dr Maxim Umansky, and in the more advanced cases of the XPTD he generated the UEDGE grids as well. For the studies of nonlocality in the ITER tokamak SOL (Chapters 6 and 7), the implementation of the Ji-Held nonlocal model into BOUT++ was originally performed by Dr John Omotani for his own research using the model. The C++ scripts for this implementation were used in this study in a minimally altered form. The intergration of these Ji-Held model scripts into the SD1D model to calculate the nonlocal heat flux and create 'SD1D-nonlocal' was performed by Dr Benjamin Dudson.

Some of the work in this thesis has been previously published or has been submitted to be published (at times verbatim). Specifically, for the ARC divertor modelling work the text, results and figures in Chapter 5, as well as some of background discussion in Chapter 4 and conclusions outlined in Chapter 8, have been published in:

- M.R.K. Wigram *et al* 2019, Performance assessment of long-legged tightly-baffled divertor geometries in the ARC reactor concept, *Nucl. Fusion*, **59**, 106052.

In addition, for the nonlocal ITER SOL work, the majority of Chapter 7 as well as parts of Chapter 6 and the conclusions outlined in Chapter 8 have been submitted to be published in:

- M.R.K. Wigram *et al* 2019, Incorporating nonlocal parallel thermal transport in 1D modelling of the ITER SOL, submitted to *Nucl. Fusion* (decision pending).

I declare that this thesis is a presentation of original work and I am the sole author. This work has not previously been presented for an award at this, or any other, University. All sources are acknowledged as References.

Decemeber 2019

Michael R K Wigram

Chapter 1

Introduction

1.1 Nuclear Fusion

With the world demand for energy increasing, and the supply of fossil fuels finite and being steadily depleted, new forms of power generation will be required to meet the energy needs of the future. Concerns over climate change from CO2-releasing forms of energy generation and the radioactive waste from nuclear fission plants makes clean, environmentally-friendly forms of energy generation desirable. Renewables energy technology is not at the stage where it can reliably meet energy demands on a large scale, and often have very low power densities that require large areas of land use. One potential technology in development, that could meet these challenges, is fusion power.

Nuclear fusion is the process that powers the Sun and other stars, occuring in the star's core under immensely high temperatures and pressures. Fusion is the opposite process to nuclear fission; whereas fission involves the decay of a heavy unstable nucleus (e.g. uranium, plutonium etc.) into two smaller products, fusion takes two light nuclei (e.g. hydrogen) and fuses them together into a single heavier nucleus. Both of these processes result in the release of energy, as can be seen when considering the binding energy of stable atomic nuclei (Figure 1.1) - the energy required to disassemle a nucleus into its constituent protons and neutrons. Nuclei with a higher binding energy are more stable and have a greater 'mass defect', where the mass of the nucleus is less than the sum of the masses for the individual nucleons. Both fission and fusion move the reaction products towards the binding energy peak (at ^{56}Fe), increasing the mass defect of the nuclei and releasing the equivalent amount of energy to the lost mass. The increase in binding energy is much greater for fusion reactions such as H→He

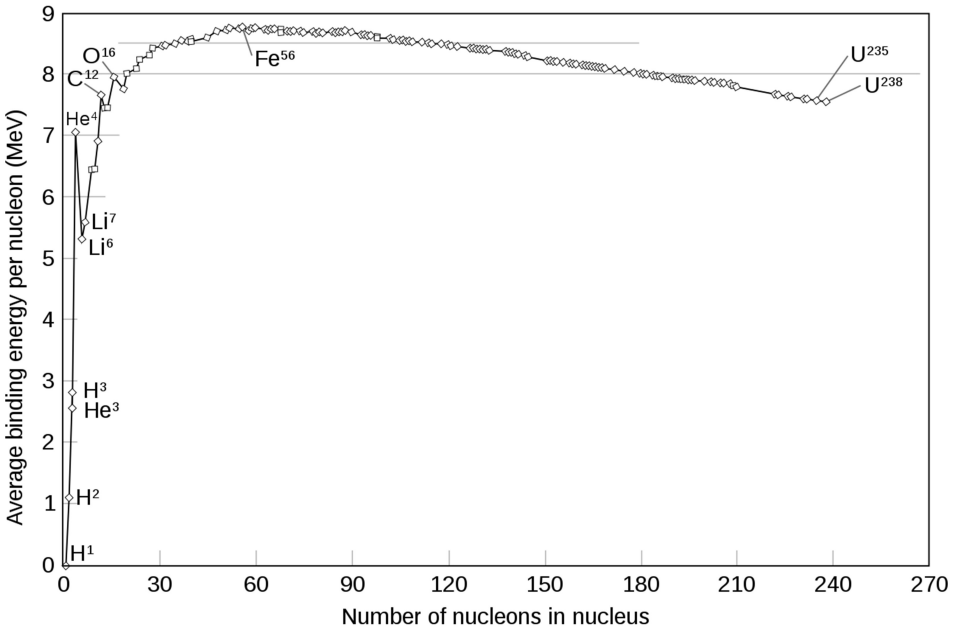

Figure 1.1: Average binding energy per nucleon for nuclei of different masses. Figure reproduced from: https://en.wikipedia.org/wiki/Nuclear_fusion

than it is anywhere else on the curve, an indication of the great potential fusion power has as a possible energy source.

There are several potential fusion reactions that could be considered for power generation, however the one most commonly considered to be applicable to a fusion reactor is the fusion of hydrogen isotopes deuterium (${}^2_1H$ or D) and tritium (${}^3_1H$ or T):

$$ {}^2_1H + {}^3_1H = {}^4_2He + n + 17.6MeV \tag{1.1}$$

For the energy released in the reaction in Equation 4.1, 1 kg of fusion fuel would produce 3.4x10^8 MJ [1] - an equivalent energy density of 6 million times that of natural gas. The fuel supplies of deuterium and tritium are large; deuterium is found naturally in water (1 in every 6700 hydrogen atoms), and hence the water in the world's oceans contain 4x10^{16} kg deuterium, which would supply the world's total electrical energy consumption for ∼10 million years (assuming 1/3 themal conversion efficiency) [2]; tritium is not naturally occuring in large quantities, but can be bred from lithium, of which there is a 62 million metric tonne estimated world resource on land [3], and more is stored in the oceans, enough for thousands of years of electrical energy demands [2]. The only waste product in the fusion reaction

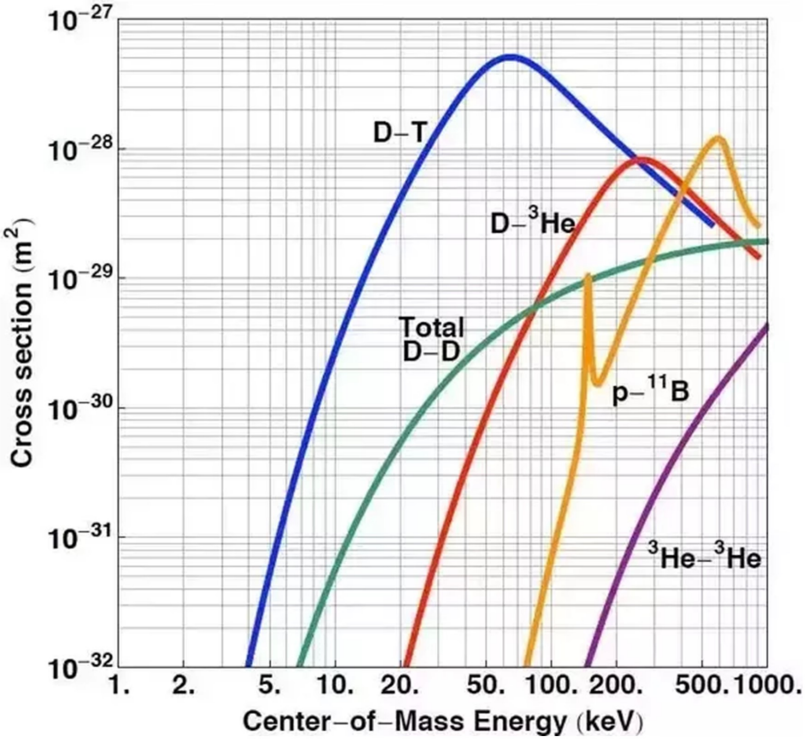

Figure 1.2: Reaction cross-sectional area σ (m^2) for different fusion reactions against center-of-mass energy (keV) of the reactants. Figure reproduced from: https://iec.neep.wisc.edu/operation.php

is helium, with some additional low/intermediate-level radioactive waste resulting from the neutron interactions with the reactor materials [4]. The high-energy density, abundant fuel reserves and the low levels of waste products makes fusion extremely attractive as a potential energy source.

In the drive to achieve net energy generation, it is sought to reach plasma 'ignition' - where the self-heating effects of the fusion reactions in the plasma are sufficient to maintain against energy losses, and the fusion reactions/plasma become self-sustaining, without requiring external heating. Considering the power balances within a plasma, the requirement for ignition is given by [5]:

$$n\tau_E > \frac{12}{\langle \sigma v \rangle} \frac{T}{\epsilon_\alpha}. \tag{1.2}$$

where n is the plasma density, T the temperature, $\langle \sigma v \rangle$ the reactivity function for the fusion reaction, ϵ_α the α-particle energy, and τ_E the energy confinement time, a quantity defining the energy loss rate of the plasma. The DT reaction is favoured for fusion for having the

combined properties of high energy released per reaction as well as having the highest reaction cross-sectional area σ (Figure 1.2) - and therefore the highest reactivity $\langle \sigma v \rangle$ - making it the easiest to achieve a burning fusion plasma with. Taking the α-particle energy of 3.5 MeV and the expression for the reactivity function as $\langle \sigma v \rangle = 1.24\text{x}10^{-24} T^2$ m^3s^{-1}, this can be written in a useful form of the fusion 'triple product':

$$nT\tau_E > 3\text{x}10^{21} m^{-3} keVs, \tag{1.3}$$

also known as the Lawson criterion [5]. This condition for ignition is highly difficult to achieve, with no fusion experiment to date having satisfied the Lawson criterion. Equation 1.3 also illustrates the strategies that can be taken to reach net fusion power, which are employed by the two main strands of fusion research: maximise the achieved triple-product by increasing the plasma density, as employed by inertial confinement fusion, or instead by improving the confinement of the plasma energy to maximise τ_E, which is the strategy utilised in magnetic confinement fusion.

1.2 Magnetic Confinement Fusion

Magnetic confinement fusion seeks to maximise the fusion triple product by improving the energy confinement of the plasma, hence maximising τ_e. In a magnetic field, the charged particles of the plasma are restricted in their radial motion relative to a magnetic field line by the Lorentz force, acting perpendicular to the magnetic field direction (Figure 1.3(a)). Plasma particles can freely move along the direction parallel to the field, but radially orbit the field line with an orbit radius of the Larmour radius, a function of the particle velocity, mass and the magnetic field strength. This constrained motion of the plasma particles is what provides greater particle and energy confinement in the plasma under magnetic confinement fusion.

Several device configurations have been explored to capitalise on the benefits of magnetic confinement, including magnetic mirror devices, magnetic pinches and stellarators. The most successful of these has been the tokamak (Figure 1.3(b)) [7] - a torus-shaped vessel within which the fusion plasma is contained, with a magnetic field applied in the toroidal direction. This allows the plasma particles to freely orbit around the torus vessel whilst restricting their radial motion, providing high particle/energy confinement as well as limiting the contact of

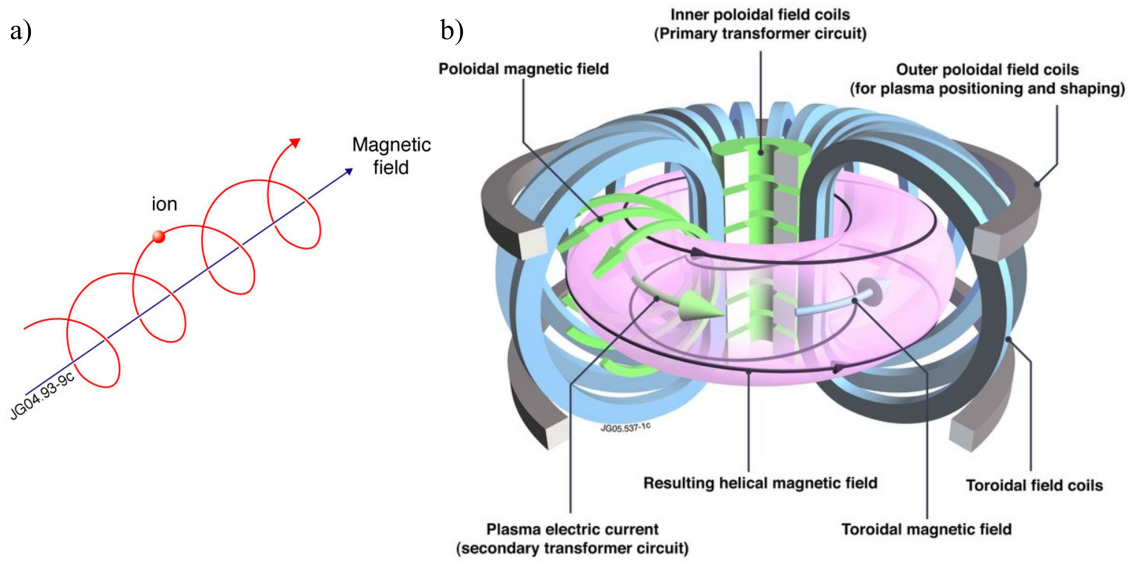

Figure 1.3: (a) Illustration of plasma particle gyromotion around a magnetic field line. (b) Schematic of a tokamak configuration, showing toroidal and poloidal field coils and magnetic field component directions. Images courtesy of EUROfusion.

the hot fusion plasma with the vessel walls and components, for which the high temperatures and energy fluxes would cause significant damage. External toroidal coils provide the toroidal magnetic field. In practice, the toroidal field alone is not sufficient to fully confine the plasma, due to the presence of radial drifts relating to the field curvature and electromagnetic drift effects [6], as well as turbulence. An additional poloidal component for the magnetic field is required as well. This field is mostly generated interally from the plasma, by driving a toroidal current in the plasma. Additional external poloidal field coils are also required, for plasma shaping and position control [8]. The magnetic field therefore has two components: the toroidal magnetic field B_ϕ and the poloidal magnetic field B_θ, making the field lines helical. Typically, in large aspect-ratio tokamaks, the poloidal field is small compared to the toroidal field ($B_\theta << B_\phi$).

Cross-sections of the tokamak toroidal vessel are given in Figure 1.4, with a 2D projection of magnetic flux surfaces shown in two different configurations - a 'limiter' and 'divertor' configuration. The core plasma is confined inside the closed magnetic flux surfaces in the centre. This core plasma is heated to $\sim 5 - 10$ keV, and typically has a plasma density on the order of 10^{20} m^{-3} [7]. Confinement of particles/energy is never perfect, with diffusion/turbulence driving transport radially outwards and across the 'last closed flux surface' (LCFS), otherwise known as the separatrix. This creates a particle and power exhaust flow-

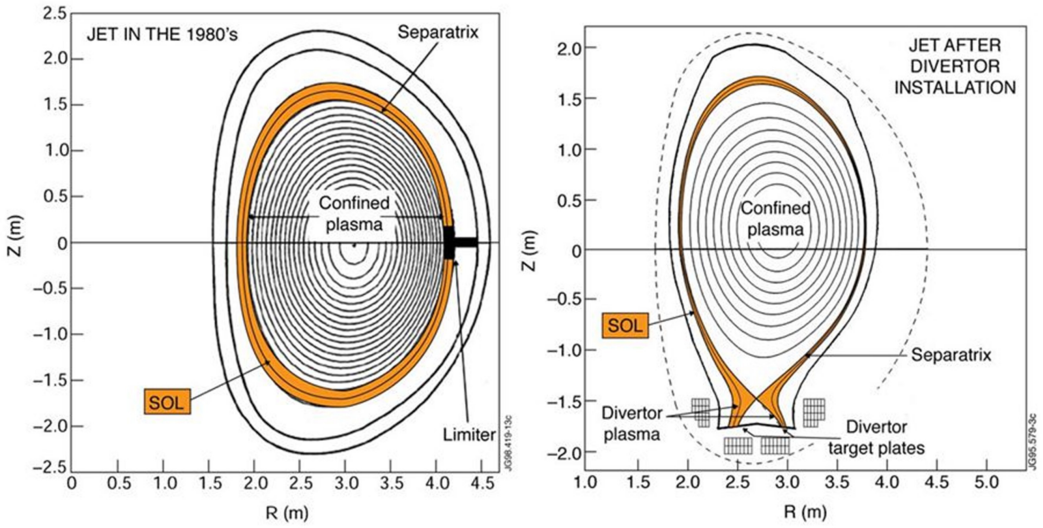

Figure 1.4: Cross-section of tokamak toroidal vessel for (left) limiter and (right) divertor configurations. Closed and open (SOL) magnetic flux surfaces are shown. Image courtesy of EFDA-JET.

ing into the open field line region outside the LCFS referred to as the'scrape-off-layer' (SOL). In the case of a limiter configuration, the LCFS is directly in contact with a material surface (and is in itself defined by the material surface) - either the vessel wall or a material 'limiter' that pertrudes out away from the vessel. Alteratively, shaping of the magnetic field can be performed so that these open field lines direct/divert the SOL plasma away from the vessel walls to specially designed target plates, designed to cope with the large power/particle fluxes being exhausted from the core. Such a scenario constitutes the 'divertor' configuration.

Of all the fusion devices to date, the tokamak has shown the greatest potential and made the greatest strides towards net fusion power, reaching fusion gain $Q = P_{fus}/P_{heat}$ orders of magnitude greater than in any other fusion device. The tokamak has therefore been the dominant focus for fusion energy research.

1.3 High-power reactors

1.3.1 Current/future devices

1.3.1.1 JET

The JET tokamak [9, 10] (Joint European Torus) is the world's largest and most powerful tokamak to date, with a major/minor radius of 2.96/1.0 m respectively, based in Culham,

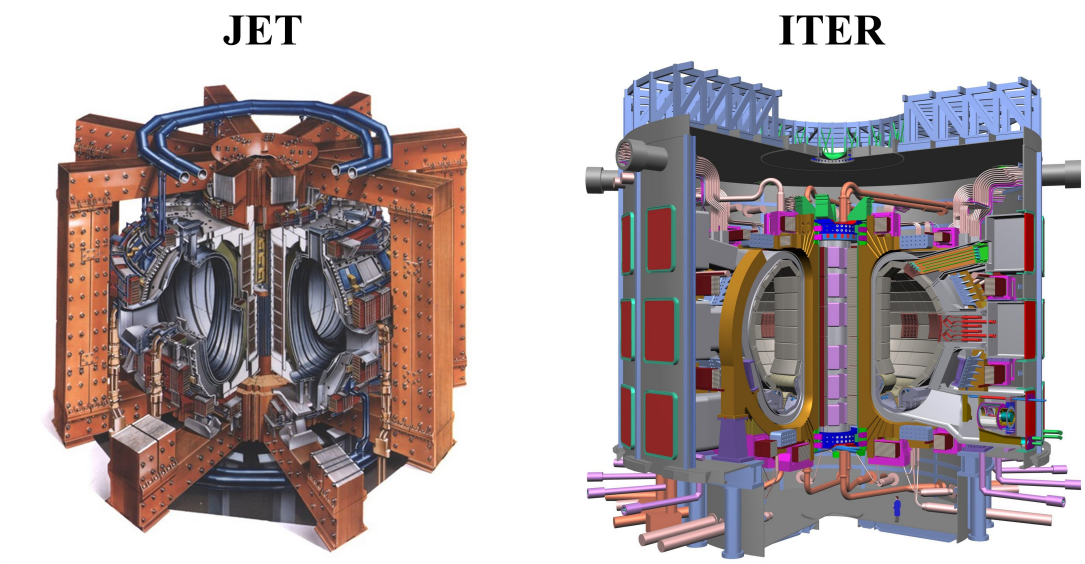

Figure 1.5: 3D diagrams for the JET (left) and ITER (right) tokamaks. Images courtesy of EFDA-JET and ITER respectively.

UK. The primary goals of the experiment were to investigate heating and confinement in reactor relevant plasmas, α-particle production and heating, and plasma-wall interactions [9]. It operates with magnetic fields up to 3.8 T, and with plasma currents up to a record of 7 MA (though more regularly operating at ~3 MA). Originally a limiter tokamak, it was transformed to a divertor setup, with divertor configurations proving the most promising for power exhaust handling and accessing high-performance 'H-mode' operation. As such JET has been used for a variety of divertor and target material studies, testing divertors with carbon and tungsten target materials. JET was the first tokamak to perform experiments using mixed D-T fuel. In 1997, DT experiments on JET reached 16.1 MW of fusion power generation, a fusion gain $Q = 0.62$ and a fusion triple product of 8.7x10^{20} keV s m^{-3} [11]. The first two of these are world records in fusion devices.

1.3.1.2 ITER

ITER [12] is the next major fusion experiment being built, which will become the new largest fusion tokamak in the world upon completion, currently under construction in Cadarache, France. It is a global collaboration, with a total of 35 nations participating and contributing to the project, including China, Russia, India, Japan, South Korea, the European Union and the US. The aim of the project is to demonstrate the feasibility of a fusion reactor and the required integrated systems, by achieving Q >1 for the first time, attaining and

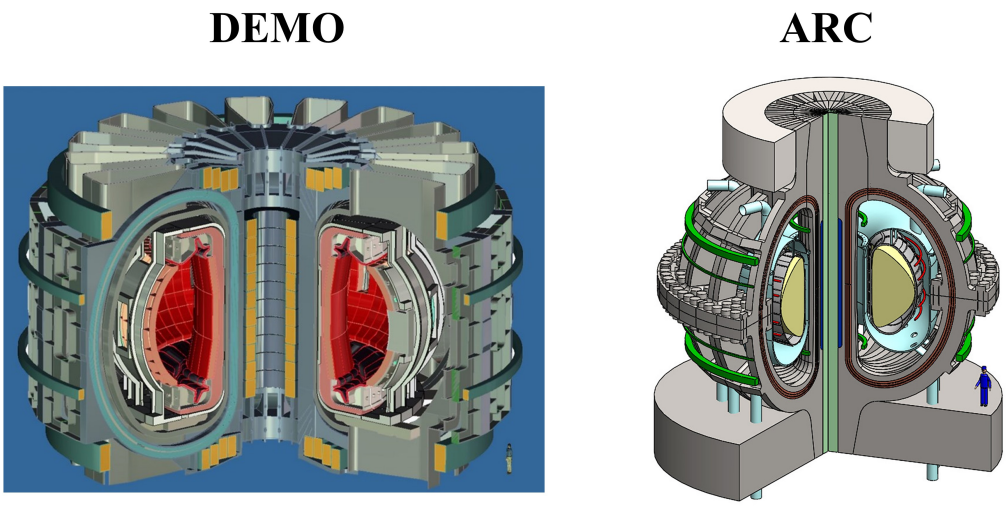

Figure 1.6: 3D diagrams for the European DEMO (left) and ARC (right) tokamaks. DEMO images courtesy of ITER. ARC figure reproduced from Reference [17] with permission from the author.

controlling fusion burn, demonstrating long-pulse techniques for steady-state operation and performing limited testing of the tritium breeder blanket technology [12]. ITER will have a major/minor radius of 6.2/2.0 m, and will operate with an on-axis field of 5.2 T. First plasma is scheduled for 2025, and the first DT experiements in 2035. At maximum power ITER is aiming to produce 500 MW fusion power for a period of 400 seconds, attempting to reach $Q \geqslant 10$. The research on many previous and currently operating tokamak experiements have/are contributing to the tokamak physics knowledge and understanding for ITER operation, particularly regarding research on JET [10], the current largest fusion device with the closest parameters to those predicted for ITER.

1.3.1.3 DEMO

Following the completion of the ITER project, the intended next step is to build a demonstration fusion pilot plant, referred to as DEMO. This reactor would build on the advances in physics and technology knowledge gained from ITER experiments, to create the first net-electrical-energy fusion device. The goal of DEMO would be to demonstrate the commercial viability of a functioning fusion reactor, to drive the next step towards the first commerical fusion reactors being deployed. To do so it must demonstrate the technology required to convert the fusion power generated into electrical power that can be delivered to the

grid, as well as demonstate regular and reliable maintenance of a fusion power plant. All current DEMO designs/studies are in the pre-conceptual stage, with a variety of different DEMO designs being proposed: Japanese DEMO [13], Korean K-DEMO [14], CFETR [15] and European DEMO (EU-DEMO) [16]. Taking EU-DEMO as an example, it would be a significantly larger device than previously attempted with a major radius of ∼9 m, would seek to generate on the order of 2GW fusion power at a Q=40, with pulses that last over 2 hours [16] - order of magnitude increases over what is intended to be achieved in ITER.

1.3.1.4 ARC

An alterative to the conventional path to fusion power, the ARC reactor [17] (Affordable, Robust, Compact reactor) is a conceptual tokamak design for a reduced size, cost and complexity demonstration fusion pilot power plant, proposed by researchers at Massachusetts Institute of Technology (MIT). As a pilot plant, ARC would produce 200-250 MWe of net-electrical power. Designed to operate at a comparable fusion power to ITER of 525 MW, it does so at a much smaller size (R_0 = 3.3 m) comparable to JET [17]. It achieves this by employing new high-temperature superconducting (HTS) technology for the toroidal field (TF) coils [18] to allow for high magnetic field operation (B_0=9.2T). The HTS technology also has the added benefit of supporting the use of resistive joints, allowing the TF coils to be demountable [18], which enables significant benefits in terms of component replacement and modular vessel construction. The reduced size and cost of this novel design makes it more economical, with potentially shorter development timeframes than other fusion reactor concepts [19]. ARC is not currently under construction - a smaller version 'SPARC' will be built first as a first step towards an ARC device.

1.3.2 Exhaust and modelling challenges facing high-power reactors

A number of significant scientific and engineering challenges remain to be overcome before fusion reactors and energy generation can become a reality. Two such challenges related to the power exhaust in the SOL, which will be the subject of the studies in this thesis, are outlined in the section.

1.3.2.1 Heat flux loading on divertor target plates

An important limiting factor for the design of future tokamak fusion devices is the thermal heat flux onto the divertor target plates. Fusion reactors will have exhaust powers of several 100 MW, which in some cases will be concentrated into a SOL heat flux width of just a few mm, presenting a daunting challenge for power exhaust management. For ITER, with a projected generated fusion power of $P_{fus} \sim 500$MW, modelling of the scrape-off-layer and divertor show an unmitigated peak heat flux of 40 MW m^{-2} at the divertor targets [20]. This could be significantly higher still if experimental scalings that predict ITER's SOL heat flux width to be $\sim$1 mm [21] prove to be correct. However, technological and materials factors for the divertor targets and cooling systems put limitations on the maximum tolerable heat flux, and the current accepted value for this maximum is only $\sim$10 MW m^{-2} [22] - well below the 40 MW m^{-2} anticipated for ITER.

Mitigation techniques will be employed to bring the ITER target heat flux within the 10 MW m^{-2} limit, including operating under partial divertor detachment - cooling the plasma at the divertor region until the plasma electrons/ions recombine to neutral hydrogen atoms - induced using impurity seeding and high neutral pressures [23–25]. However, there is significant uncertainty on whether these techniques will be adequate to handle the heat loads expected from future reactor-level devices like DEMO [26, 27], which will move to significantly higher fusion and exhaust powers than in ITER. Extensive materials research is being performed to improve the material capabilities of plasma facing components [20, 28]. Moreover, in order to suppress target erosion to acceptable levels for a reactor, fully detached divertor conditions will be required. Added to this requirement is a formidable divertor plasma control challenge - e.g. at no time during high power operation should the divertor plasma be allowed to re-attach to the target (or be limited to a very short length of time if it does occur), despite inevitable variations in power exhaust that are associated with transients (e.g. confinement transitions).

Advanced divertor configurations are proposed as potential solutions to the divertor power loading issue. These generally feature extended volumes for the divertor, additional poloidal field nulls, and shaping control beyond what is used for a standard vertical target divertor. However, these are yet to be demonstrated to be adequate to meet the demands of future reactors. The divertor heat flux problem therefore remains a huge challenge that is yet to be resolved.

1.3.2.2 Kinetic effects in collisionless plasmas

Accurate modelling of the thermal transport in the SOL is of vital importance, both in accurately predicting the heat flux through the SOL and onto the divertor targets, and in assessing the design and effectiveness of heat flux mitigation methods such as detachment. Currently large-scale modelling of the tokamak SOL has been built on a fluid description, which assumes locality and high collisionality of the plasma. However, it has long been known that in the presence of steep temperature gradients, classical local transport theory breaks down [29,30]. In low collisionality plasmas the thermal transport becomes 'nonlocal', depending on conditions in distant regions of the plasma due to the streaming of supra-thermal particles from upstream regions. The resulting nonlocal kinetic effects on the thermal transport, not captured in fluid simulations, have significant impacts on the temperature and heat flux profiles [29,31].

The necessary conditions can be found in SOL plasmas (as well as in laser heated plasmas relevant to inertial confinement fusion where this problem has recieved more attention [29–31]), where parallel temperature gradients can become steep approaching the divertor target plates [32]. As tokamaks move towards reactor devices and higher fusion powers, nonlocality is likely to play an increasingly important role, as higher upstream temperatures still need to be reduced to ∼few eV at the divertor target, requiring ever steeper temperature gradients. Nonlocal effects could therefore potentially have significant impact on plasma conditions across the SOL and the divertor target for high power devices, which have implications on the target plate conditions and the ability to achieve detached divertor operation. If nonlocal kinetic effects are not captured in SOL simulation codes used for future reactor designs, these designs may be fundamentally flawed and risk failure of the divertor systems/components. Accurately capturing nonlocality in thermal transport models is therefore a major challenge to be addressed in predictive modelling of the SOL.

1.4 Thesis outline

In this thesis, the divertor heat flux problem is investigated for the ARC reactor, performing 2D SOL simulations to assess the divertor designs proposed for the reactor, to determine if detachment can be obtained for the expected power exhaust and to investigate the physics of the advanced divertor geometry proposed. In addition, a reduced-kinetic nonlocal heat

flux model is implemented into a 1D complex SOL code, and the impact of incorporating nonlocal thermal transport in SOL modelling is assessed for the ITER reactor. Comparisons with results from JET and expected SOL conditions for DEMO and ARC are presented also.

This thesis is structured as follows: Chapter 2 provides background physics relevant to the tokamak SOL, divertors, and advanced divertor proposals. Chapter 3 details modelling techniques used for fluid simulations of the SOL, and outlines the 'SD1D' and 'UEDGE' codes used in this study. Chapter 4 describes the ARC fusion reactor concept, details of the design and divertor design, and the physics motivations behind them. In Chapter 5, the results of the ARC divertor modelling study are presented. Chapter 6 describes the theory of nonlocal transport and kinetic effects in the SOL, as well as discussing the 'Ji-Held' nonlocal model used in this study. Results of a 1D nonlocal transport study for ITER is presented in Chapter 7. Finally, a summary of this thesis and conclusions from the studies peformed are presented in Chapter 8.

Chapter 2

The tokamak SOL and divertor

2.1 The scrape-off-layer plasma

The tokamak scrape-off-layer, outside of the last-closed-flux-surface (LCFS), is at a much lower temperature than the core plasma, at several 10s to a few 100 eV upstream at the separatrix, and can drop to just a few eV at the divertor target plates. At these temperatures, many processes that are not relevant to the hotter core plasma become significant. For lower temperatures, recombination of plasma electrons and ions to form neutrals becomes important, with the neutral density in the plasma rising significantly. The high neutral density introduces many atomic processes to the plasma, including excitation, ionisation and charge exchange, which create additional particle, energy and momentum sources/sinks in the SOL. These atomic processes are summarised in Equations 2.1(a-e) [33]:

$$H^+ + e \rightarrow H \qquad \text{(recombination)}, \tag{2.1a}$$

$$H^+ + 2e \rightarrow H + e \qquad \text{(3-body recombination)}, \tag{2.1b}$$

$$H + e \rightarrow H^* + e \qquad \text{(excitation)}, \tag{2.1c}$$

$$H + e \rightarrow H^+ + 2e \qquad \text{(ionisation)}, \tag{2.1d}$$

$$H^+ + H \rightarrow H + H^+ \qquad \text{(charge exchange)}. \tag{2.1e}$$

Interactions of the plasma with material surfaces acts as a source of molecular hydrogen as well, introducing molecular process to the plasma [33]:

$$H_2 + e \rightarrow H + H + e \quad \text{(dissociation)}, \tag{2.2a}$$

$$H_2 + e \rightarrow H^+ + H + 2e \quad \text{(dissociative ionisation)}, \tag{2.2b}$$

$$H_2 + e \rightarrow H_2^+ + 2e \quad \text{(molecular ionisation)}, \tag{2.2c}$$

$$H_2^+ + e \rightarrow H + H \quad \text{(dissociative recombination)}, \tag{2.2d}$$

$$H_2^+ + e \rightarrow H^+ + H^+ + 2e \quad \text{(dissociative ionisation)}. \tag{2.2e}$$

The rates of these different reactions are functions of the plasma temperature and density, and all contribute to an evolving composition of the SOL plasma.

Impurity species are also present in the SOL, and can play an important role in SOL physics. The primary source of impurities is helium ash from the fusion reactions in the core, which must be exhausted through the SOL. High-Z impurities can also be present - either through deliberate injection or from plasma-surface interactions with plasma-facing components. Impurities undergo similar atomic and molecular processes to the hydrogen neutrals, but the dominant processes for the high-Z impurities tend to be excitation rather than ionisation, leading to photon emission and a loss of energy as radiation, significantly cooling the plasma [34]. This can be beneficial in terms of reducing the divertor target temperature and heat flux. However, impurity transport can see impurities travel long distances in the SOL, and up to the main plasma. Impurity contamination in the core has a dilution effect on the fusion fuel, reducing the fusion reaction rate, as well as radiating and cooling the core, which can significantly degrade energy confinement and make ignition more difficult, and can potentially cause disruption events from cooling of the core edge [34, 35]. Therefore, whilst impurities may be required for cooling the divertor plasma, it remains important to control the impurity transport and limit concentration in other regions.

2.2 The divertor SOL

For most current and future tokamak designs, a divertor configuration is employed. The divertor magnetic geometry is generated using an external poloidal field coil carrying a current I_D in the same direction as the plasma current I_P [36]. The resultant poloidal field

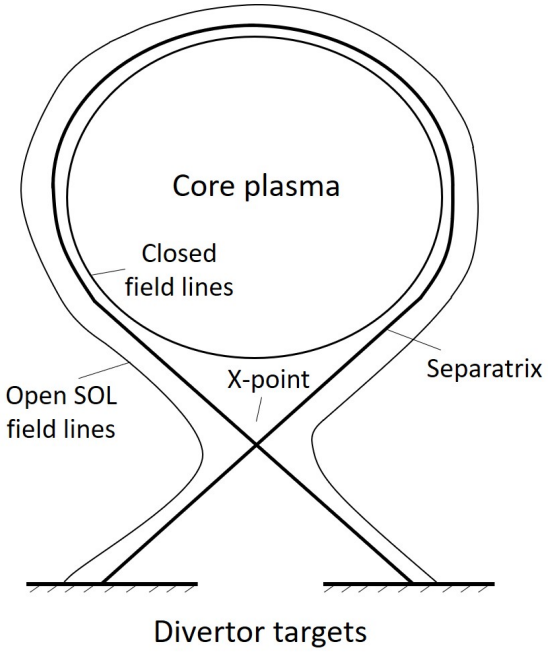

Figure 2.1: Schematic of divertor configuration magnetic geometry, with open and closed field line regions, separatrix and X-point, and divertor target plates labelled.

lines make a figure-of-eight shape. At some location between the current centres the poloidal fields from each source cancel, creating a magnetic null or 'X-point' (Figure 2.1) where the magnetic field is purely toroidal. The magnetic flux surface passing through the X-point is called the separatrix, which defines the last-closed-flux-surface (LCFS) for the plasma; within the separatrix, the flux surfaces are closed, containing the confined core plasma; outside the separatrix, magnetic flux surfaces are open and intersect with the divertor target plates, forming the divertor SOL. The connection length - the distance a plasma particle travels along a field line before striking a solid surface - on the separatrix is theoretically infinite [36] (due to $B_\theta = 0$ at the X-point), and SOL field lines that pass close to the X-point are extended to very long connection lengths.

There are many benefits that the divertor configuration provides over limiters, in particular moving the plasma-facing-components (i.e. divertor targets) away from direct contact with the main confined plasma. This allows better control and prevention of impurities/neutrals contamination of the main plasma from plasma-surface interactions (see section 2.2.1). The divertor configuration also allows for higher neutral compression towards the divertor targets, which enables more efficient and compact gas pumping systems required for removal of helium-ash impurity and for plasma density control [37]. In addition, the di-

vertor configuration allows for favourable access to improved energy confinement regimes such as H-mode, which is beneficial for achieving high core temperatures, fusion gain and triple-products required for plasma ignition (but also bring with them risks associated with Edge-Localised-Modes (ELMs) - instabilities that produce violent outbursts of particles and energy from the core into the SOL, causing significant damage to plasma-facing components - which need to be mitigated or avoided entirely for future fusion reactors to be successful). H-modes were first discovered in divertor tokamaks [38], and whilst H-mode has since been obtained with limiters, it is much harder to achieve and has typically lower τ_E [37]. For these reasons the divertor has become the preferred configuration for tokamak designs [22].

2.2.1 Plasma-surface interactions

Plasma-surface interactions (PSI) play an important role in SOL physics, with repercussions that can seriously impact the divertor and exhaust power management, as well as the fusion core performance and stability.

2.2.1.1 The plasma sheath

The divertor target surface acts as a particle sink to the plasma, with ions and electrons flowing down the open SOL field lines into the solid surface. The significant mass and inertia difference between the plasma electrons/ions leads to interesting physics at the plasma/surface boundary. The lower electron mass gives it a higher thermal velocity than the ions (by factor $\sqrt{\frac{m_i}{m_e}}$), which initially creates a greater flow of electrons into the surface. The resulting build-up of negative charge establishes an electric field in a thin region above the target surface, repelling and slowing the electrons and accelerating the ions until the flow of each species into the surface becomes equal. This region is known as the 'sheath' and provides important boundary conditions for the SOL plasma.

An important theoretical result for the sheath is given by the Bohm criterion, which helps define particle and energy transport through the sheath region. A simplified derivation of the Bohm criterion will be outlined in this section [39], for a 1D case with $T_i = 0$. Within the sheath quasineutrality no longer holds, such that $n_i \neq n_e$, and the electric field E in the sheath is defined by

$$\nabla \cdot \mathbf{E} = \frac{e}{\epsilon_0}(n_i - n_e). \tag{2.3}$$

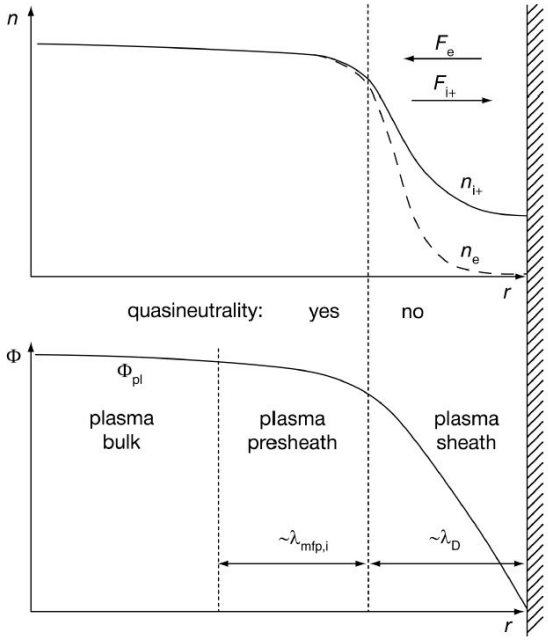

Figure 2.2: Illustration of the sheath and presheath regions in a plasma in their effects on the plasma ion/electron density and plasma potential. Figure reproduced from Reference [40].

With $\mathbf{E} = -\nabla\phi$, this gives Poisson's equation for the electric potential ϕ in the sheath as

$$\frac{\partial^2\phi}{\partial x^2} = -\frac{e}{\epsilon_0}(n_i - n_e). \tag{2.4}$$

The electron velocity distribution within the sheath is assumed to be approximately Maxwellian, so the electron density n_e takes a Boltzmann distribution given by

$$n_e = n_{se}\exp\left[\frac{e(\phi - \phi_{se})}{T_e}\right] \tag{2.5}$$

where n_{se} and ϕ_{se} are the density and potential at the 'sheath-edge'. ϕ_{se} describes the potential drop that occurs upstream of the sheath edge, in the plasma itself, due to the presence of the sheath. This region is referred to as the 'pre-sheath'. The impact of the sheath and presheath regions on the plasma ion/electron density and plasma potential are illustrated in Figure 2.2.

Assuming all ions originate at a location upstream of the sheath edge, for the case that $T_i = 0$, energy conservation gives us the relation

$$\frac{1}{2}m_i v_{se}^2 = -e\Delta\phi_{pre-sheath} = -e\phi_{se}. \tag{2.6}$$

Combined with particle conservation $n_i v_i = constant$, the ion density n_i is given by

$$n_i = n_{se}\left(\frac{\phi_{se}}{\phi}\right)^{1/2} \tag{2.7}$$

Thus, substituting Equations 2.5 and 2.7 into 2.4, Poisson's equation becomes

$$\frac{\partial^2\phi}{\partial x^2} = -\frac{e}{\epsilon_0}n_{se}\left[\left(\frac{\phi_{se}}{\phi}\right)^{1/2} - exp\left[\frac{e(\phi-\phi_{se})}{T_e}\right]\right]. \tag{2.8}$$

Defining $\delta \equiv \phi_{se} - \phi > 0$, the terms $(\phi_{se}/\phi)^{1/2}$ and $\exp[(e(\phi-\phi_{se})/T_e]$ can be expanded as:

$$\left(\frac{\phi_{se}}{\phi}\right)^{1/2} \approx 1 + \frac{1}{2}\frac{\delta}{\phi_{se}} = 1 - \frac{1}{2}\frac{\delta}{|\phi_{se}|} \tag{2.9}$$

$$exp\left[\frac{e(\phi-\phi_{se})}{T_e}\right] \approx 1 - \frac{e\delta}{T_e} \tag{2.10}$$

which gives

$$\frac{\partial^2\delta}{\partial x^2} \approx \frac{en_{se}\delta}{\epsilon_0}\left(\frac{e}{T_e} - \frac{1}{2|\phi_{se}|}\right). \tag{2.11}$$

This form is a 2nd-order differential equation. With the assumption that an oscillatory sheath potential ϕ is uphysical, in order for the solution to Equation 2.11 to be non-oscillatory the condition must be met that:

$$\frac{e}{T_e} \geq \frac{1}{2|\phi_{se}|} \tag{2.12}$$

which from Equation 2.6 becomes

$$m_i v_{se}^2 \geq T_e \tag{2.13}$$

or

$$v_{se} \geq c_s \tag{2.14}$$

where c_s is the sound speed $c_s = \sqrt{T_e/m_i}$. This is the Bohm criterion, showing that the ions must be accelerated by the pre-sheath and enter the sheath edge at a velocity greater than or equal to the sound speed.

Generalisation of the Bohm criterion to $T_i \neq 0$ gives the same result but with a corrected form of c_s to account for the ion temperature [39], such that

$$v_{se} \geq c_s = \left(\frac{T_e + \gamma T_i}{m_i}\right)^{1/2} \tag{2.15}$$

where γ is the ratio of specific heat, equal to 1 for isothermal flow, 5/3 for adiabatic flow with isotropic pressure, and 3 for 1D adiabatic flow. Exact numerical solutions of the full plasma/sheath domain finds that $v_{se} \approx c_s$ for plasmas where charge imbalances are small [41], and therefore this approximation is often adopted for sheath modelling.

The length scale of the sheath L_{sheath} can also be estimated using Equation 2.11, by approximating the equation to

$$\frac{\delta}{L_{sheath}^2} \approx \frac{en\delta}{\epsilon_0}\frac{e}{T_e}. \tag{2.16}$$

Rearranging this equation gives

$$L_{sheath} \approx \left(\frac{\epsilon_0 T_e}{e^2 n}\right)^{1/2} \equiv \lambda_D \tag{2.17}$$

where λ_D is the Debye length. For temperatures in the 10-30 eV range with $n = 10^{19}$ m^{-3}, then $L_{sheath} \approx 10\mu$m, showing how thin the plasma sheath is for typical tokamak edge conditions.

The sheath is not just a particle sink for the SOL plasma, but also an energy sink. As mentioned, within the sheath region the ions are accelerated by the electric potential and the electrons are repelled. This repulsion means that only electrons with energies high enough to overcome the sheath potential are able to pass through the sheath and be absorbed into the solid surface; the rest are reflected back into the SOL plasma.

In order to be absorbed into the solid surface, the electron must have a forward-directed kinetic energy greater than $|e\phi_{sf}|$, where ϕ_{sf} is the potential drop between the plasma and that at the solid surface. The net electron power flow at the sheath edge is therefore

$$q_{se}^e = (2T_e + e|\phi_{sf}|)\Gamma_{se} \tag{2.18}$$

where $\Gamma_{se} = n_{se}v_{se}$ is the particle flux through the sheath edge, since the absorbed electrons had an energy that was $e|\phi_{sf}|$ higher at the sheath edge than when they reach the solid surface [42].

It is therefore the high energy tail of the electron energy distribution that is lost from the SOL at the sheath boundary, which has a significant cooling effect on the SOL electrons (analogous to evaporative cooling), reducing T_e at the sheath edge. The electrons that are lost contribute to the negative charge build-up on the surface that accelerates the ions, so

in effect the electron energy is being transferred to heat the ions. Analysis of the energy distribution of the ions accelerated through the sheath gives the ion energy flux through the sheath edge [42] as

$$q_{se}^{i} \approx 2T_i\Gamma_{se}. \tag{2.19}$$

The total power flux through the sheath edge is typically written as

$$q_{se} \equiv q_{se}^{e} + q_{se}^{i} = \gamma_{SH}T_i\Gamma_{se}. \tag{2.20}$$

where γ_{SH} is the 'sheath heat transmission coefficient'. For conditions where $T_i \approx T_e$, this coefficient takes values of $\gamma_{SH} \approx 7 - 8$ [42].

2.2.1.2 Recycling

Whilst the divertor targets (and any plasma-facing surface, for that matter) are particle sinks for the plasma, they also serve as a particle source for neutral atomic and molecular hydrogen. Plasma ions that collide with the target surface are either backscattered back into the plasma or absorbed into the material surface. Backscattered particles are predominately neutral, with ions having picked up an electron from the surface through surface recombination, with a backscattered energy ∼30-50% of the incident ion energy [43]. Surface recombination is also an important source of heating, since much of the energy released goes into heating the wall. Hydrogen ions absorbed into the surface also neutralise, and diffuse around the material. Some hydrogen neutrals remain trapped in the material, but others diffuse back to the surface and re-enter the plasma, and can also be released from the material by further incoming flux of plasma particles and radiation. The ratio of the flux returning to the plasma to the incident flux is called the recycling coefficient. This can typically be in the range of 0.80-0.95 in tokamak devices, but in steady-state regimes can be as high as unity [43]. Neutral hydrogen that re-enters the plasma through recycling leads to a high neutral density around the divertor target plate, but from charge exchange and in certain conditions with long ionisation mean-free-paths these neutrals can travel far into the SOL and even into the main plasma before they are re-ionised.

2.2.1.3 Sputtering

Sputtering is another important PSI effect that provides a source of impurities to the plasma. Physical sputtering occurs where the an incident ion/neutral on a solid surface transfers sufficient energy to exceed the surface binding energy of the material, releasing surface atoms into the plasma. Chemical sputtering involves chemical reactions occuring between the ion/neutrals and the surface material, releasing the reaction products. Both sputtering process cause erosion of the material surface, introducing a source of high-Z impurities to the SOL. High-Z impurities radiate more strongly in the plasma, which can pose significant problems for fusion performance if they migrate to the core plasma. In addition, the rate of erosion from sputtering at the divertor target is expected to be a limiting factor to the divertor - and therefore the fusion reactor - operational lifetime. This strongly motivates keeping target edge temperatures low to minimise the sputtering yield. [34]

2.2.2 Attached plasma regimes - sheath and conduction limited SOL

For a SOL plasma with temperatures relatively high throughout the domain (with $T > 10$ eV at the sheath boundary), where the recombination rate and plasma neutral density remain low, the plasma in this case is in direct contact with the material surface and is said to be in an 'attached' regime. An important distinguishing property in such conditions is the presence or absence of a significant temperature decrease along the length of the SOL, which determines important properties of the divertor SOL.

2.2.2.1 The sheath-limited SOL

A SOL that is approximately isothermal in the parallel direction, with little or no significant temperature gradients, is described as being in the 'sheath-limited' regime. This can occur in situations where the parallel heat conductivity is high and weak temperature gradients are sufficient for conduction to carry the entirety of the power entering the SOL flux tube, or alternatively where parallel convection is high and carries the majority of the parallel power flux. Both scenarios reduce variation in temperature along the SOL length. In such conditions, the limiting factor for parallel heat flow through the SOL is the energy flow that can pass through the sheath (Equation 2.20) - hence the SOL is sheath-limited, with the sheath heat transmission properties defining the properties of the SOL plasma. Isothermal SOL temperatures are undesirable for tokamak operation - particularly for high power and

future reactor devices, upstream SOL temperatures are high (10s to few 100s eV), and maintaining these high temperatures at the divertor targets would lead to unacceptable power loading and erosion at the divertor target plates. Therefore the sheath-limited regime is not considered an appropriate operating regime for a fusion tokamak.

2.2.2.2 The conduction-limited SOL

In contrast, in conditions where the parallel heat conductivity is low and convection is not strong such that conduction dominates over convective transport, heat flow through the SOL is limited by the finite heat conductivity of the plasma ($\kappa_{||0}T_e^{5/2}$, where $\kappa_{||0} \approx 4.4\text{x}10^{-11}$ W m^{-1} K^{-1}) - hence referred to as the 'conduction-limited' regime - giving rise to large temperature gradients, necessary to sustain the required parallel heat flow. Such a scenario typically arises where the SOL collisionality is sufficiently high and/or there is a significant particle source downstream in the SOL near the divertor target region, such as ionisation of neutrals, reducing plasma flow and convective transport. In attached conditions where temperatures are high enough that recombination is low, the major downstream particle source is ionisation of recycled neutrals, and therefore the conduction-limited regime also gets referred to as the 'high-recycling regime'. Given the high upstream temperatures anticipated for reactor devices and the strong motivation to reduce the target temperature to low values to reduce divertor erosion, conduction-limited SOL conditions are much preferred as a tokamak divertor operating regime than the sheath-limited SOL.

2.2.3 Detachment

If the plasma temperature at the target drops to <5 eV, the neutral ionisation rate drops below ion-neutral friction processes, and if the temperature is reduced further to ~1 eV, volumetric recombination processes start to dominate, extinguishing the plasma at the target surface with the plasma density dropping to near zero [44] (Figure 2.3). Neutral gas builds up above the divertor target, and the particle and energy flux to the target is significantly reduced. In this regime, the plasma is said to be 'detached' from the divertor target, not in contact with the target solid surface but instead with a gaseous neutral target, with volumetric recombination replacing surface recombination as the plasma sink.

The characteristics of detachment can be summarised to three main features: a reduction in the ion current to the plate by recombination, a reduction of plasma pressure at the plate,

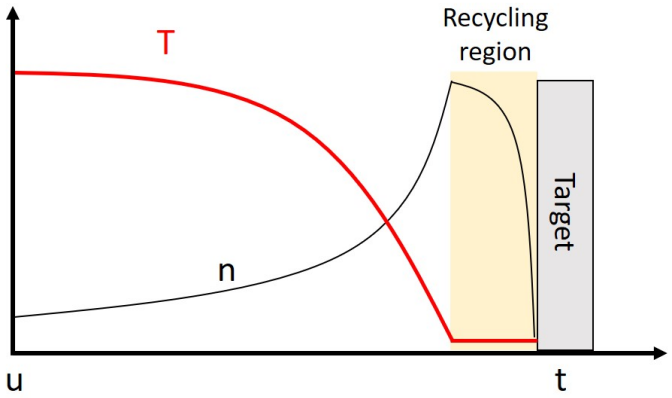

Figure 2.3: Illustration of plasma T and n profiles for a SOL in high-recycling, detached conditions. The stagnation and target boundary locations in the SOL are indicated by "u" and "t" respectively.

and a reduction in energy reaching the plate [124]. This makes plasma detachment attractive as a potential solution to mitigating the divertor heat load. The very low temperatures and reduced plasma flux to the target surface also reduces target plate erosion from decreased sputtering rates. These benefits give strong motivation to operate tokamaks in the detached regime, and as such methods to induce detachment by cooling the plasma are often employed in divertor designs, such as injection of neutral gas puffs and/or high-Z impurities (typically argon, neon or nitrogen), to enhance energy losses in the divertor region from radiation and ion-neutral interactions.

Experimental studies have been performed for detachment in large tokamaks such as JET, JT-60 and DIII-D [46]. For future reactor devices operating over long pulses, a detachment front would need to be controlled so that it does not move up to the core X-point and LCFS, where it can cause a MARFE - a radiation instability caused by cooling of the confined core plasma [47]. To this end, stable detached regimes are desired, where the detachment front finds equilibrium within the length of the divertor leg. Previous experiments with carbon plasma-facing components (PFCs) have shown that 'partially detached divertors' - where only a limited area of the SOL is detached from the target plate, whilst the rest remains attached - are more stable than fully detached [49], and this is the regime that has been adopted for the ITER divertor design. However, more recent experiments with metallic PFCs have shown the capability for stable full detachment of target plates [48].

2.2.4 Cross-field transport

Radial cross-field transport across the LCFS provides the primary particle/energy source into the SOL. In a simple SOL model with no additional sources, the radial particle flux $\Gamma_\perp$ must be balanced by the total parallel flux to the targets surfaces $\Gamma_{||} \approx nc_s$ (assuming that $v_{se} \approx c_s$). Expressing the perpendicular flux as $\Gamma_\perp = -D_\perp \frac{dn}{dx}$, the radial extent of the SOL can be roughly estimated as [50]

$$\lambda_n \approx \left(\frac{2D_\perp^{SOL} L}{c_s} \right)^{1/2} \tag{2.21}$$

where $D_\perp$ is the perpendicular diffusive transport coefficient. A similar estimate for the parallel power e-folding width $\lambda_{q||}$ of the SOL can be determined [51], again assuming flux across the LCFS is the only source/sink in the SOL, such that

$$\lambda_{q||} \approx \frac{2}{7} \frac{\chi_\perp n_{sep} T_{sep} A_p}{P_{SOL}} \tag{2.22}$$

where $\chi_\perp$ is the perpendicular thermal transport coefficient, n_{sep} and T_{sep} are the density and temperature at the separatrix, P_{SOL} is the power crossing the LCFS into the SOL and A_p is the core plasma surface area.

In neoclassical theory, radial particle and thermal transport is driven by radial gradients dn/dr and dT/dr, with a greater magnitude of transport than classical random-walk motion due to toroidal geometry and magnetic field line effects (e.g. banana orbits). In experiment, the values of $D_\perp$ and $\chi_\perp$ greatly exceed that predicted by neoclassical theory, and the radial transport is described as 'anomalous'. $D_\perp$ and $\chi_\perp$ are therefore empirical quantities, that need to be determined from experiment (or alternatively from full kinetic/gyro-kinetic simulations). The anomalous transport is thought to be driven by plasma turbulence, driven by kinetic micro-instabilities and transport of blob structures (high-density coherent plasma structures originating around the LCFS [53]) into/across the SOL. The discrepancy between the measured and neoclassical values of $D_\perp$ and $\chi_\perp$ can be over an order of magnitude in some cases [50], implying that plasma turbulence processes play a crucial role in radial transport in the SOL

2.2.5 Divertor geometry

A variety of different divertor designs are possible, and the divertor geometry can have significant effects on divertor performance and operation. Tilting of the target plates relative to the magnetic field lines is often employed as a strategy to reduce the power flux density, spreading the incident plasma power over a larger effective surface area at the target. Impinging angles (the angle the magnetic field lines intersect the target plate) as small as 1-2° have been considered [22]. Whether the target is vertically or horizontally tilted with respect to the magnetic field is also a factor to consider (Figure 2.4); recycled neutrals tend to take a trajectory in a direction normal to the target surface [44, 54]. Therefore, neutrals leaving a vertically tilted target leave with a horizontal trajectory, and take a path that passes throught the separatrix, the hottest region of the SOL plasma. The resulting ionisation of these neutrals has a significant cooling and fueling effect, reducing the temperature and raising the plasma density. Recycled neutrals from horizontally tilted plates, on the other hand, will take a vertical trajectory, away from the separatrix into cooler regions of the SOL, where the ionisation/cooling effect is less beneficial. Therefore vertically inclined target plates have become the norm for divertor designs.

Another important factor for divertor designs is if the divertor is 'open' or 'closed' (Figure 2.5). The divertor closure refers to the relative ability of recycled neutrals to be confined in the divertor region. A closed divertor places baffles at the edges of the SOL plasma near the divertor target, creating an enclosed divertor chamber. An open divertor configuration does not include these baffles. The baffles trap neutrals within the divertor volume, preventing their escape in the perpendicular direction to the magnetic field and reducing the transport of neutrals to the main chamber plasma. These effects act to increase the neutral pressure at the target plate, and the higher neutral pressures sustained in the closed divertor allows for greater ease of achieving detachment, with experimental studies showing divertor detachment being achieved at lower plasma densities compared to open configurations [52]. Since detached operation is desirable from a target plate power loading perspective, this is a significant benefit of the closed divertor geometry. The enclosed chamber also reduces impurity escape and transport, providing greater confinement of the impurities to the divertor region. However, despite these benefits, the baffles restrict diagnostic access to the divertor chamber region, and an open divertor may be advantageous from the perspective of experimental studies and analysis.

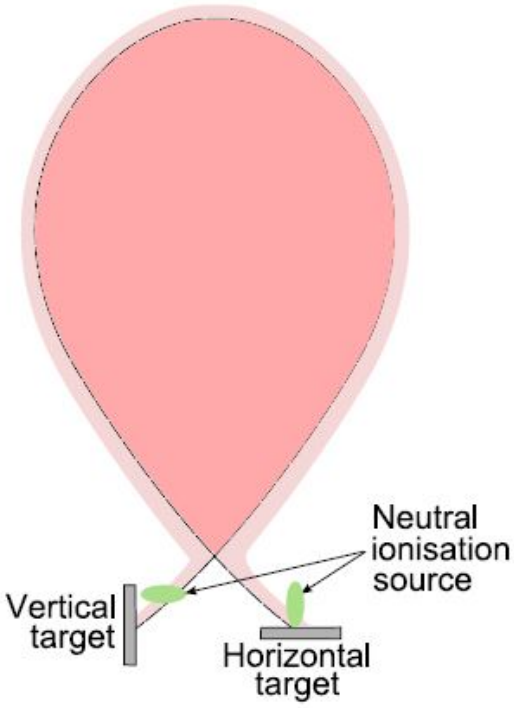

Figure 2.4: Illustration of the impact of vertical and horizontal target plate tilting on recycled neutral paths. Figure reproduced from Reference [55].

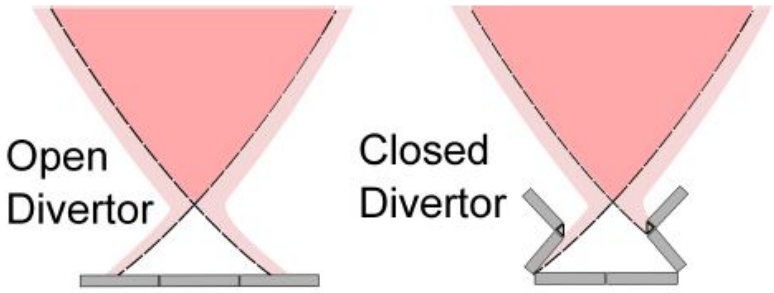

Figure 2.5: Illustration of open and closed divertor configurations. Figure reproduced from Reference [55].

2.3 The ITER divertor

A CAD diagram of the ITER divertor cassette is given in Figure 2.6 [56]. It features deep and baffled vertical inner and outer divertor targets. Inner and outer reflector plates are included as a protection for the structure in the event of strike point excursions. A dome structure is located under the X-point of the magnetic equilibrium, separating the inner and outer divertors, reducing neutral escape from the divertor region and improving pumping.

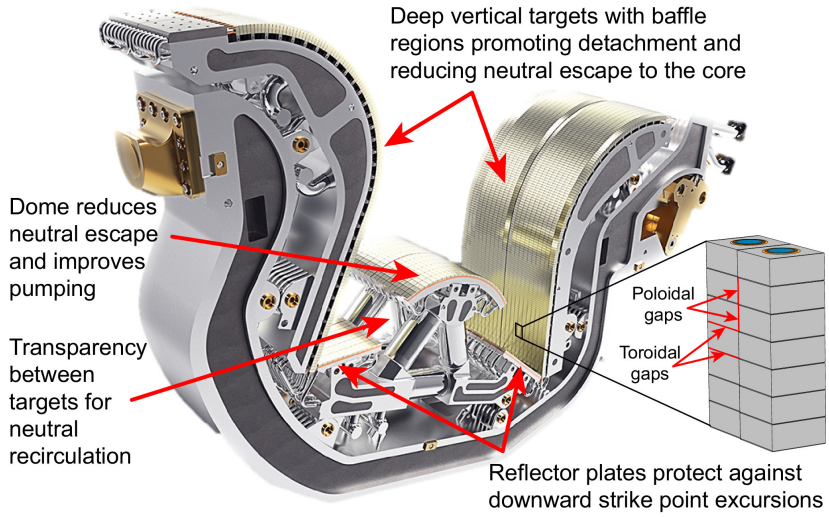

Figure 2.6: CAD diagram of the ITER divertor. Figure reproduced from Reference [56].

This dome structure is open to allow neutral flow between the targets, referred to as neutral recirculation, a process found to be effective in reducing in-out target power asymmetries under partially detached conditions [56].

Main chamber injection of neutral hydrogen gas puffs and impurities (either nitrgoen or neon) will be used to enhance radiation losses in the SOL, induce partial detachment and reduce the power loading experienced by the divertor targets. The heat flux is reduced further by a factor 4 from magnetic flux expansion [22] (where reductions in the magnetic field strength cause the magnetic flux surfaces to spatially expand to cover a larger area) and by a factor 2.5 from target inclination such that field lines intersect the target plate at a $\sim 2^{\circ}$ angle [57]. The target plates are constructed from specially designed tungsten monoblocks, that can tolerate steady-state heat fluxes up to $\sim$10 MW m^{-2} (though recent research and development of the monoblock design suggests heat fluxes up to 15 MW m^{-2} could potentially be handled [56]). The unmitigated heat flux density predicted for ITER at the target plates is $>$40 MW m^{-2}, and therefore the mitigation methods described above must reduce this to below the 10-15 MW m^{-2} acceptable value.

2.4 Advanced divertors

There is significant uncertainty on whether these techniques will be adequate to handle the heat loads expected from future reactor-level devices like DEMO [26, 27], which will move to significantly higher fusion and exhaust powers. Complex magnetic geometries have also been

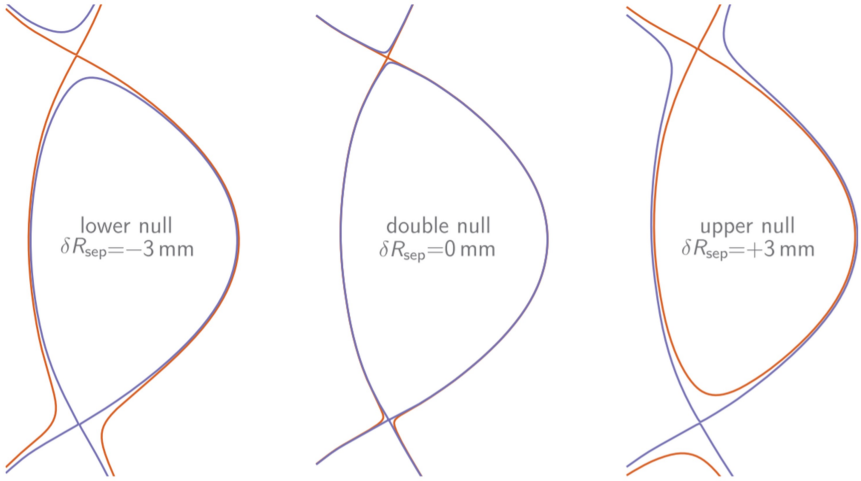

Figure 2.7: Illustration of double-null divertor configuration, showing primary and secondary separatricies. Figure reproduced from Reference [63].

proposed - with additional magnetic X-points within or close to the divertor plasma volume - in order to improve the power handling potential of the divertor SOL. A variety of advanced divertor configurations [58] and operational scenarios are being considered to address these challenges. Advanced divertor geometries generally feature extended divertor leg length and volume, additional magnetic X-points, and shaping control beyond that used for a standard vertical target divertor. Many of these designs have been studied computationally [59, 60] and have been or are presently being explored in proof-of-concept experiments, such as in the TCV tokamak [61]. A number of these designs are under assessment for application to DEMO [62].

2.4.1 Double-null

A double-null [63] divertor configuration puts two magnetic nulls at the core plasma, one above and one below, to enable operation with an upper and lower divertor configuration. Each X-point has its own separatrix, and if the two separatrices are spaced closely enough, the inner divertors become magnetically separated from the outer divertors and the plasma exhaust is split across two sets of targets, reducing the power loading received by any single divertor. In this configuration the vast majority of the exhaust power (>80% [63]) is delivered to the outer divertor targets, due to increased transport at larger R, reducing power loading on the inner divertor where B_T is highest. This greatly reduces the power loading requirements on the inner divertor.

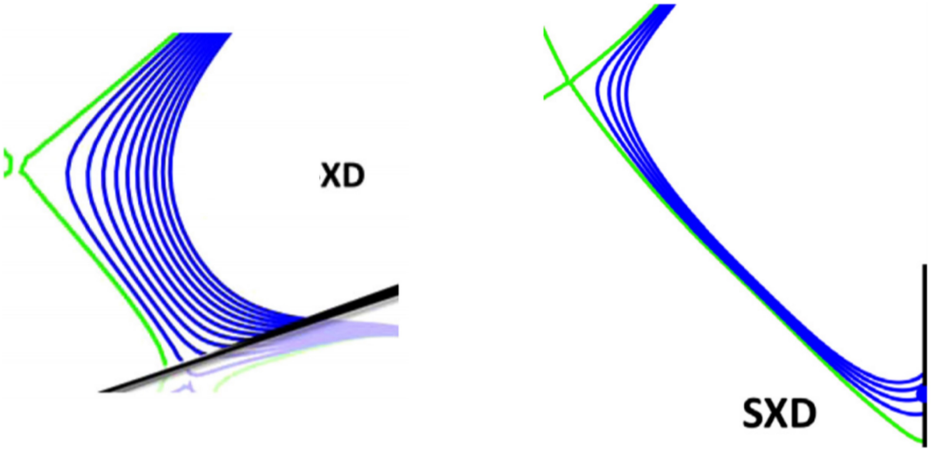

Figure 2.8: Illustration of the SOL magnetic flux surfaces in the X-Divertor (XD) and Super-X Divertor (SXD) configurations. Figure reproduced from [68].

If the radial separation between separatrices for the upper and lower divertor X-points is 0 (hence occupying the same separatrix), then the configuration is described as a perfectly balanced double-null. If the separation is not 0, then the double-null is biased towards the upper or lower divertor (with said divertor receiving a higher power loading). The separation must be kept with $\sim 2\ \lambda_q||$ in order to maintain the benefits of the double-null configuration [63]. This is within a few mm (or less) in a plasma several metres across, which presents a sigificant control challenge.

2.4.2 X-divertor

The X-divertor [64] puts an additional magnetic X-point downstream of the LCFS X-point, beyond the divertor target. This has the impact of both extending the connection length of the magnetic field lines in the SOL, as well as increasing the poloidal flux expansion of the magnetic field lines as they impact the divertor target. The magnetic flux surfaces 'flare' outwards, rather than contracting inwards as in a standard divertor configuration. This allows the plasma to wet a larger surface area on the target plate, and reduces the peak power loading density experienced at the target.

2.4.3 Super-X Divertor (SXD)

The 'Super-X Divertor' (SXD) [65] is a similar configuration to the X-divertor, using the same concept of placing a secondary X-point beyond the divertor target plate, but extends

the divertor leg length to create a long-legged divertor geometry. This further increases SOL connection length, and achieves not only increased flux expansion in the poloidal plane but in the toroidal plane as well, by placing the divertor target at larger major radius (since $B_\phi \propto 1/R$). The SXD is being implemented in the MAST-U tokamak design for an experimental assessment [66].

2.4.4 Snowflake divertor

It has been found to be also possible to create a second-order null of the poloidal magnetic field (where the magnetic field scales as r^2 with distance r from the null, as opposed to scaling with r for first-order null), by the incorporation of additional poloidal field coils. In this configuration, the separatrix forms a hexagonal structure, leading to the designated name for this configuration as 'snowflake' divertors [67]. The resulting field line structure has significant flux expansion, and long field line length in the vicinity of the X-point.

The second-order null is topologically unstable, however, and splits into two first-order nulls. Maintaining close proximity of these two nulls allows the features of the exact snowflake topology to be retained. Depending on the relative position of the two nulls and their separatricies, these configurations are labelled 'snowflake-plus' (SF+) or 'snowflake-minus' (SF-).

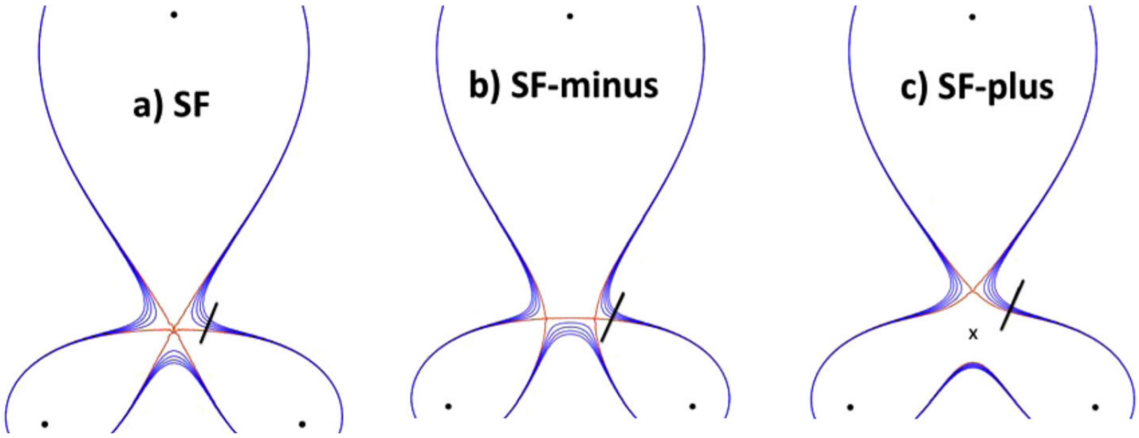

Figure 2.9: Illustration of the perfect snowflake divertor, snowflake-minus and snowflake-plus. Figure reproduced from [68].

2.4.5 X-Point Target Divertor (XPTD)

A recent proposed divertor geometry is the X-point target divertor (XPTD) [69]. This has a similar geometry to the SXD, where an additional poloidal magnetic field null is formed at the end of an extended outer divertor leg, only in this case the X-point is formed within the plasma volume as a "virtual target". With control of X-point location, the divertor X-point intercepts the SOL flux tubes carrying the highest parallel heat flux density $q_{||}$, splitting the plasma exhaust into two channels and diverting them to two separate targets in the divertor volume. This configuration has similarities to the SF+/-, except without maintaining close physical proximity of the two magnetic nulls.

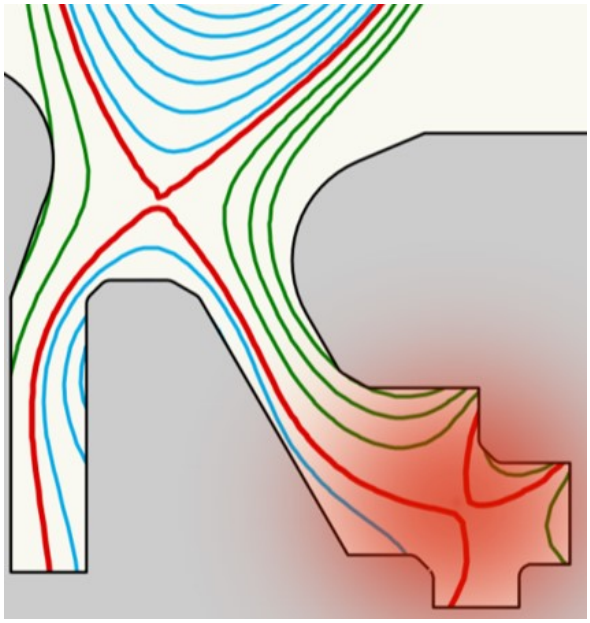

Figure 2.10: Illustration of the X-Point Target Divertor (XPTD) configuration. Figure reproduced from [70].

Chapter 3

Modelling the tokamak SOL

Kinetic theory describes the behaviour of the plasma in terms of the evolution of the single-particle distribution function $f(\mathbf{x}, \mathbf{v}, t)$, where $\mathbf{x}$ and $\mathbf{v}$ are the particle position and velocity respectfully at time t. The Fokker-Plank equation gives a fundamental first-principles description of a plasma in terms of the distribution functions of each plasma species [71]:

$$\frac{\partial f_\alpha}{\partial t} + \mathbf{v} \cdot \nabla f_\alpha + \frac{Z_\alpha e}{m_\alpha} (\mathbf{E} + \mathbf{v} \times \mathbf{B}) \cdot \nabla_{\mathbf{v}} f_\alpha = \left(\frac{\partial f_\alpha}{\partial t} \right)_c \tag{3.1}$$

where Z_α and m_α are the atomic number and mass of plasma species α, $\mathbf{E}$ and $\mathbf{B}$ are the acting electric and magnetic field vectors in the plasma, and $\left(\frac{\partial f_\alpha}{\partial t}\right)_c$ is the Fokker-Plank collision operator, describing the Coulomb interactions between plasma particles of all species on scales of order of the Debye length. However, whilst the kinetic equation describes the exact evolution of the single-particle distribution function over time, it is often too computationally demanding to numerically solve in simulation modelling, due to the large 6-dimensional phase space of f and the nonlinearity of the force and collision terms. A fluid description of the plasma is typically employed to determine large-scale plasma behaviour, which is significantly less computationally demanding.

3.1 SOL fluid description/Braginskii equations

A fluid model describes the plasma in terms of averaged quantities such as the particle density $n(\mathbf{x}, t)$, fluid velocity $u(\mathbf{x}, t)$, and pressure $p(\mathbf{x}, t)$. A set of fluid equations for the plasma can be obtained by taking moments of Equation 3.1 - multiplying Equation 3.1 by a function

$\phi(\mathbf{v})$ and integrating over velocity space [71, 72]. The functions of interest here are $\phi(\mathbf{v}) = 1$, $m_\alpha \mathbf{v}$ and $m_\alpha v^2/2$, as these give the conservation equations for particles, momentum and energy.

3.1.1 Particle conservation - continuity equation

Taking $\phi(\mathbf{v}) = 1$, the moment equation of Equation 3.1 becomes the continuity equation for plasma particles (since the Fokker-Plank collision operator conserves particles, $\int \left(\frac{\partial f_\alpha}{\partial t}\right)_c d^3v = 0$):

$$\frac{\partial n_\alpha}{\partial t} + \nabla \cdot (n_\alpha \mathbf{u}_\alpha) = 0 \tag{3.2}$$

where density and fluid velocity are defined by

$$n_\alpha = \int f_\alpha d^3v, \quad \mathbf{u}_\alpha = \frac{1}{n_\alpha} \int f_\alpha \mathbf{v} d^3v. \tag{3.3}$$

Note: The RHS of Equation 3.2 is only zero if there are no particle sources or sinks. In a real SOL plasma this is not the case (due to neutral processes and interactions with material surfaces outlined in Chapter 2), and Equation 3.2 is modified such that RHS$\neq$0 to include source/sink terms.

3.1.2 Momentum conservation equation

Taking $\phi(\mathbf{v}) = m_\alpha \mathbf{v}$, Equation 3.1 becomes:

$$\frac{\partial}{\partial t}(n_\alpha m_\alpha \mathbf{u}_\alpha) + \nabla \cdot \left(\int f_\alpha m_\alpha \mathbf{v}\mathbf{v} d^3v \right) = Z_\alpha e n_\alpha (\mathbf{E} + \mathbf{u}_\alpha \times \mathbf{B}) + \mathbf{F}_\alpha \tag{3.4}$$

where $\mathbf{F}_\alpha = \int m_\alpha \mathbf{v} \left(\frac{\partial f_\alpha}{\partial t}\right)_c d^3v$ is the rate of momentum transfer between species due to collisions. Using the relative velocity $\mathbf{v}' = \mathbf{v} - \mathbf{u}_\alpha$ and defining the pressure p_α and temperature T_α as

$$p_\alpha = n_\alpha T_\alpha = \int f_\alpha \frac{m_\alpha v'^2}{3} d^3v', \tag{3.5}$$

the $\int f_\alpha m_\alpha \mathbf{v}\mathbf{v} d^3v$ term can be written as

$$\int f_\alpha m_\alpha \mathbf{v}\mathbf{v} d^3v = n_\alpha m_\alpha \mathbf{u}_\alpha \mathbf{u}_\alpha + p_\alpha \mathbf{I} + \mathbf{\Pi}_\alpha \tag{3.6}$$

where $\mathbf{I}$ is the unit matrix and

$$\mathbf{\Pi}_\alpha = \int f_\alpha m_\alpha \left(\mathbf{v}'\mathbf{v}' - \frac{v'^2}{3}\mathbf{I} \right) d^3v' \tag{3.7}$$

is the traceless viscosity tensor. Using this and Equation 3.2, the final momentum conservation equation becomes

$$n_\alpha m_\alpha \left(\frac{\partial \mathbf{u}_\alpha}{\partial t} + \mathbf{u}_\alpha \cdot \nabla \mathbf{u}_\alpha \right) + \nabla p_\alpha + \nabla \cdot \mathbf{\Pi}_\alpha = Z_\alpha e n_\alpha (\mathbf{E} + \mathbf{u}_\alpha \times \mathbf{B}) + \mathbf{F}_\alpha \tag{3.8}$$

3.1.3 Energy conservation equation

Taking $\phi(\mathbf{v}) = m_\alpha v^2/2$, Equation 3.1 becomes:

$$\frac{\partial}{\partial t} \left(\int \frac{1}{2} m_\alpha v^2 f_\alpha d^3v \right) + \nabla \cdot \left(\int \frac{1}{2} m_\alpha v^2 f_\alpha \mathbf{v} d^3v \right) = Z_\alpha e n_\alpha \mathbf{E} \cdot \mathbf{u}_\alpha + Q_\alpha \tag{3.9}$$

where $Q_\alpha = \int \frac{1}{2} m_\alpha v^2 \left(\frac{\partial f_\alpha}{\partial t} \right)_c d^3v$ is energy gained by species α due to collisions with other species (or the 'heat exchange term'). Again taking the relative velocity $\mathbf{v}' = \mathbf{v} - \mathbf{u}_\alpha$ and recalling the definitions for temperature and $\mathbf{\Pi}_\alpha$, we can rewrite the terms such that

$$\int \frac{1}{2} m_\alpha v^2 f_\alpha d^3v = \int \frac{1}{2} m_\alpha v'^2 f_\alpha d^3v' + \frac{1}{2} n_\alpha m_\alpha u_\alpha^2 = \frac{3}{2} n_\alpha T_\alpha + \frac{1}{2} n_\alpha m_\alpha u_\alpha^2 \tag{3.10}$$

and

$$\int \frac{1}{2} m_\alpha v^2 f_\alpha \mathbf{v} d^3v = \mathbf{q}_\alpha + \left(\frac{5}{2} n_\alpha T_\alpha + \frac{1}{2} n_\alpha m_\alpha u_\alpha^2 \right) \mathbf{u}_\alpha + \mathbf{\Pi}_\alpha \cdot \mathbf{u}_\alpha, \tag{3.11}$$

where

$$\mathbf{q}_\alpha = \int \frac{1}{2} m_\alpha v'^2 f_\alpha \mathbf{v}' d^3v' \tag{3.12}$$

is the heat flux. Using the results of Equations 3.11 and 3.13, then Equation 3.9 becomes

$$\frac{\partial}{\partial t}\left(\frac{3}{2}n_\alpha T_\alpha + \frac{1}{2}n_\alpha m_\alpha u_\alpha^2\right) + \nabla\cdot\left[\mathbf{q}_\alpha + \left(\frac{5}{2}n_\alpha T_\alpha + \frac{1}{2}n_\alpha m_\alpha u_\alpha^2\right)\mathbf{u}_s + \mathbf{\Pi}_\alpha\cdot\mathbf{u}_\alpha\right] = Z_\alpha e n_\alpha \mathbf{E}\cdot\mathbf{u}_\alpha + Q_\alpha \tag{3.13}$$

Taking [Equation 3.13 - Equation 3.8 $\cdot\mathbf{u}_\alpha$], and using the continuity equation in Equation 3.2, the final result for the energy conservation equation is given as

$$\frac{3}{2}n_\alpha\left(\frac{\partial T_\alpha}{\partial t} + \mathbf{u}_\alpha\cdot\nabla T_\alpha\right) + \nabla\cdot\mathbf{q}_\alpha + n_\alpha T_\alpha\nabla\cdot\mathbf{u}_\alpha + \mathbf{\Pi}_\alpha : \nabla\mathbf{u}_\alpha = Q_\alpha - \mathbf{F}_\alpha\cdot\mathbf{u}_\alpha. \tag{3.14}$$

3.1.4 Braginskii equations

The results of the above analysis - Equations 3.2, 3.8 and 3.14 - are collected and rewritten here, and together comprise the fluid description of a plasma [71]:

$$\boxed{\frac{\partial n_\alpha}{\partial t} + \nabla\cdot(n_\alpha\mathbf{u}_\alpha) = 0} \tag{3.15a}$$

$$\boxed{n_\alpha m_\alpha\left(\frac{\partial\mathbf{u}_\alpha}{\partial t} + \mathbf{u}_\alpha\cdot\nabla\mathbf{u}_\alpha\right) + \nabla p_\alpha + \nabla\cdot\mathbf{\Pi}_\alpha = Z_\alpha e n_\alpha(\mathbf{E} + \mathbf{u}_\alpha\times\mathbf{B}) + \mathbf{F}_\alpha} \tag{3.15b}$$

$$\boxed{\frac{3}{2}n_\alpha\left(\frac{\partial T_\alpha}{\partial t} + \mathbf{u}_\alpha\cdot\nabla T_\alpha\right) + \nabla\cdot\mathbf{q}_\alpha + n_\alpha T_\alpha\nabla\cdot\mathbf{u}_\alpha + \mathbf{\Pi}_\alpha : \nabla\mathbf{u}_\alpha = Q_\alpha - \mathbf{F}_\alpha\cdot\mathbf{u}_\alpha} \tag{3.15c}$$

These fluid equations for particle, momentum and energy conservation in a plasma are expressed in unknown plasma variables of density n, flow velocity u and temperature T, that can be solved for. The density, flow velocity and temperature can be referred to as the zeroth, first and second fluid moments (defined in Equations 3.3 and 3.5). However, Equations 3.15(a-c) are dependent on higher-order moments also, with additional terms of $\mathbf{q}_\alpha$, $\mathbf{\Pi}_\alpha$, $\mathbf{F}$ and Q_α. These need to be determined in order to close the fluid equations. To determine these quantities exactly would require solving the kinetic equation, for which a complete solution is not possible, but using simplifying physical assumptions allows for an expansion procedure to calculate the closure terms, most famously performed by Braginskii [71], and the final plasma equations incorporating these closures are hence termed the *Braginskii equations*.

The principle assumptions used by Braginskii are as follows [71]:

- The distribution function can be expanded about a Maxwellian distribution function,

such that

$$f_\alpha = f_\alpha^{(0)} + \delta f_\alpha \tag{3.16}$$

where $f_\alpha^{(0)}$ is the Maxwellian part given by

$$f_\alpha^{(0)} = \frac{n_\alpha}{(2\pi T_\alpha/m_\alpha)^{3/2}} \exp\left[-\left(\frac{m_\alpha}{2T_\alpha}(\mathbf{v}' - \mathbf{u}_\alpha)\right)\right] \tag{3.17}$$

and δf_α is a small correction to the Maxwellian.

- Both $\mathbf{u_e}$ and $\mathbf{u_i}$ are of the order of the thermal ion velocity v_{ti}, but their difference need not be. The velocity difference in the perpendicular direction must be small in comparison, such that

$$u_{i||} \sim u_{e||} \sim v_{ti}, \qquad v_{ti} \gg u_{i\perp} - u_{e\perp}. \tag{3.18}$$

- The plasma is in the collisional limit, such that

$$\frac{\rho_\alpha}{L_\perp}, \frac{\lambda_\alpha}{L_{||}} \ll 1 \tag{3.19}$$

where ρ_α and λ_α are the gyro-radius and mean-free-path, and $L_\perp$ and $L_{||}$ are perpendicular and parallel scale lengths, and

$$\frac{\partial}{\partial_t}, \omega_{d\alpha} \ll \nu_\alpha \tag{3.20}$$

where $\omega_{d\alpha}$ and ν_α are drift and collision frequencies.

Using these assumptions, Braginskii derived the closure terms as follows (for a simple plasma with a single ion species) [71, 73]: since the total momentum change from collisions between species is zero, $\sum_i \mathbf{F}_i = -\mathbf{F}_e$, where the rate of momentum transfer from ions to electrons is

$$\mathbf{F}_e = \mathbf{F}_u + \mathbf{F}_T \tag{3.21}$$

with $\mathbf{F}_u$ and $\mathbf{F}_T$ being the friction and thermal forces respectively, given by

$$\mathbf{F}_u = -\frac{m_e n}{\tau_e}(0.51 U_{||} + U_\perp) \tag{3.22}$$

$$\mathbf{F}_T = -0.71 n \nabla_{||} T_e - \frac{3}{2} \frac{n}{|\omega_{ce}| \tau_e} \hat{\mathbf{b}} \times \nabla T_e \tag{3.23}$$

where $\mathbf{U} = \mathbf{u}_e - \mathbf{u}_i$ is the relative electron/ion velocity, τ_e is the electron collision time, $\hat{\mathbf{b}}$ is the unit vector parallel to the magnetic field, and ω_{ce} is the electron gyrofrequency.

The electron heat flux term is given by

$$\mathbf{q}_e = \mathbf{q}_{e,u} + \mathbf{q}_{e,T} \tag{3.24}$$

where $\mathbf{q}_{e,u}$ and $\mathbf{q}_{e,T}$ are the convective and conductive heat flux components, with

$$\mathbf{q}_{e,u} = n T_e \left(0.71 U_{||} + \frac{3/2}{|\omega_{ce}| \tau_e} \hat{\mathbf{b}} \times \mathbf{U} \right) \tag{3.25}$$

and

$$\mathbf{q}_{i,T} = \frac{n T_e \tau_e}{m_e} \left(-3.16 \nabla_{||} T_e - \frac{4.66}{\omega_{ce}^2 \tau_e^2} \nabla_{\perp} T_e - \frac{5/2}{|\omega_{ce}| \tau_e} \hat{\mathbf{b}} \times \nabla T_e \right), \tag{3.26}$$

and the ion heat flux term is given by

$$\mathbf{q}_{e,T} = \frac{n T_i \tau_i}{m_i} \left(-3.9 \nabla_{||} T_i - \frac{2}{\omega_{ci}^2 \tau_i^2} \nabla_{\perp} T_i - \frac{5/2}{\omega_{ci} \tau_i} \hat{\mathbf{b}} \times \nabla T_i \right). \tag{3.27}$$

The heat exchange terms give the ion energy increase as

$$Q_i = \frac{3 m_e}{m_i} \frac{n}{\tau_e} (T_i - T_e) \tag{3.28}$$

and the electron energy increase as

$$Q_e = -\mathbf{F} \cdot \mathbf{U} - Q_i. \tag{3.29}$$

The components of the viscosity tensor given for the ions $\mathbf{\Pi}_i$ and electron $\mathbf{\Pi}_e$ are detailed and complex, and for the sake of brevity are not presented here, but can be found in Reference [73].

3.2 1D SOL modelling - SD1D

The SD1D model [74] in the BOUT++ framework evolves a 1-dimensional (1D) form of the Braginskii plasma fluid equations, solving the equations for plasma density n, parallel

momentum density $m_i n u_{||}$ and static pressure $p = 2enT_e$. The plasma model consists of the following equations:

$$\frac{\partial n}{\partial t} = -\nabla \cdot (\hat{\mathbf{b}} u_{||} n) + S_n - S \tag{3.30a}$$

$$\frac{\partial}{\partial t}\left(\frac{3}{2}p\right) = -\nabla \cdot \mathbf{q} + u_{||}\partial_{||} p + S_p - E - R \tag{3.30b}$$

$$\frac{\partial}{\partial t}(m_i n u_{||}) = -\nabla \cdot (m_i n u_{||} \hat{\mathbf{b}} u_{||}) - \partial_{||} p - F \tag{3.30c}$$

$$j_{||} = 0 \tag{3.30d}$$

$$T_i = T_e = \frac{1}{2}\frac{p}{en} \tag{3.30e}$$

$$\mathbf{q} = \frac{5}{2} p \hat{\mathbf{b}} V_{||} - \kappa_{||e} \hat{\mathbf{b}} \partial_{||} T_e \tag{3.30f}$$

where $u_{||}$ is the plasma parallel flow velocity, T_e/T_i are the electron/ion temperatures respectively, $\mathbf{q}$ is the heat flux, $\kappa_{||e}$ is the electron heat conduction coefficient (equal to the Spitzer-Härm thermal conductivity, $\kappa_{||e} = \kappa_{SH}$), $j_{||}$ is the plasma current density, and $\hat{\mathbf{b}}$ gives the unit vector for the direction of the magnetic field. The partial differential in this context is the parallel derivative defined as $\partial_{||} \equiv \hat{\mathbf{b}} \cdot \nabla$. The model assumes equal electron and ion temperatures and velocities, such that only a single set of fluid equations are required to model the plasma species. This assumption is not true for the SOL in general – in experiments and modelling it is found that generally $T_i > T_e$ [75, 76], with the two species being thermally decoupled due to their differences in mass and mobility. However, the assumption $T_i \approx T_e$ is often employed to simplify 1D models when using them to probe other aspects of the physics, as well as to increase computational efficiency when doing so. Since the energy equation is tailored to electron thermal conduction (which carries the majority of the conducted heat flux due to the higher mobility of the electrons), T_i is likely to be underestimated in this model, and since interactions with neutrals and impurities are strong functions of T_i the model will lose accuracy in this area.

Source terms in the equations are given by S_n and S_p for the particle and pressure sources respectively, where S_p is related to the internal energy source by $S_E = \frac{3}{2}S_p$. These terms represent particle and energy transport across the LCFS into the SOL domain. Terms S, R, E and F provide transfer channels for particles, momentum and energy due to recombination, ionisation, charge-exchange processes, radiation and elastic collisions. In the SD1D code,

these rates are given by:

$$R_{rc} = n^2\langle\sigma v\rangle_{rc} \quad \text{(recombination)} \tag{3.31a}$$

$$R_{iz} = nn_g\langle\sigma v\rangle_{iz} \quad \text{(ionisation)} \tag{3.31b}$$

$$R_{rc} = nn_g\langle\sigma v\rangle_{cx} \quad \text{(charge-exchange)} \tag{3.31c}$$

$$R_{el} = nn_g\langle\sigma v\rangle_{el} \quad \text{(elastic collisions)} \tag{3.31d}$$

where n_g is the neutral gas density, and $\langle\sigma v\rangle_{rc}$, $\langle\sigma v\rangle_{iz}$, $\langle\sigma v\rangle_{cx}$ and $\langle\sigma v\rangle_{el}$ are the reaction rates for recombination, ionisation, charge-exchange and elastic collisions respectively. These cross-sections are calculated in the model from semi-analytical expressions, except for the recombination rates which are calculated from a look-up table of coefficients.

The transfer channels are then defined as follows:

- S gives the net recombination (i.e. plasma sink/neutral source):

$$S = R_{rc} - R_{iz} \tag{3.32}$$

- R gives plasma energy losses due to radiation processes:

$$R = (1.09T_e - 13.6\text{eV})R_{rc} + E_{iz}R_{iz} + (1\text{eV})R_{ex} + R_{z,imp} \tag{3.33}$$

  where E_{iz} is the ionisation energy, and R_{ex} and $R_{z,imp}$ are the excitation and impurity radiation respectively. The $1.09T_eR_{rc}$ term is due to 3-body recombination, which becomes a source of plasma heating below a temperature of around 5.25eV [77].

- E is the energy transfer to neutrals from recombination, ionisation, charge exchange and elastic collision processes:

$$E = \frac{3}{2}T_eR_{rc} - \frac{3}{2}T_gR_{iz} + \frac{3}{2}(T_e - T_g)R_{cx} + \frac{3}{2}(T_e - T_g)R_{el} \tag{3.34}$$

  where T_g is the neutral gas temperature.

- F is the ion friction momentum losses due to charge exhange and recombintation:

$$F = m_iu_{||}R_{rc} - m_iu_{g||}R_{rc} + m_i(u_{||} - u_{g||})R_{cx} + m_i(u_{||} - u_{g||})R_{el} \tag{3.35}$$

where $u_{g||}$ is the neutral gas parallel velocity.

A fluid-diffusive neutral model is employed, with neutrals being evolved with their own equivalent set of fluid equations for neutral density, momentum and pressure:

$$\begin{aligned} \frac{\partial n_g}{\partial t} &= -\nabla\cdot(\mathbf{b}u_g n_g) + \nabla\cdot(D_g\nabla n_g) + S - n_g/\tau_g \\ \frac{\partial}{\partial t}\left(\frac{3}{2}p_g\right) &= -u_g\partial_{||}p_g + \nabla\cdot(\kappa_g\nabla T_g) + \nabla\cdot(D_g T_g\nabla n_g) + E - \nabla\cdot\left(\frac{5}{2}p_g u_g\right) \\ \frac{\partial}{\partial t}(m_i n u_g) &= -\nabla\cdot(m_i n u_g \mathbf{b}u_g) - \partial_{||}p + F \end{aligned} \tag{3.36}$$

where D_g is the neutral diffusion coefficient

$$D_g = v_{g,th}^2/(\nu_{cx} + \nu_{gg}) \tag{3.37}$$

and κ_g is the neutral gas heat conduction coefficient, defined by

$$\kappa_g = n_g v_{g,th}^2/(\nu_{cx} + \nu_{gg}) \tag{3.38}$$

where $v_{g,th} = \sqrt{eT_g/m_i}$ is the neutral thermal velocity, ν_{cx} is the charge-exhange frequency and ν_{gg} is the neutral-neutral collision frequency. Only neutral atoms are included in this neutral model, so molecular neutral processes are not included. The V_g is an effective parallel velocity, given by the sum of a parallel flow and parallel projection of a perpendicular diffusion [74]:

$$u_g = u_{g||} - \left(\frac{B_\phi}{B_\theta}\right)^2 \frac{\partial_{||}p_g}{(\nu_{cx} + \nu_{gg})m_i n_g}. \tag{3.39}$$

SD1D models half the tokamak SOL (Fig. 3.1), from stagnation point (plasma flow $u_{||} = 0$, assumed to be at the outboard midplane) to the divertor target. A source region is defined between the upstream stagnation boundary and a specified X-point location, defining the spatial extent of source terms S_n and S_p. Symmetry (zero flow) boundary conditions are applied at the upstream boundary, corresponding to:

$$\partial_{||}n = 0 \quad \partial_{||}p = 0 \quad \partial_{||}T = 0 \quad u_{||} = 0 \quad nu_{||} = 0 \tag{3.40}$$

At the downstream boundary, a plasma sheath edge boundary is employed, using the Bohm

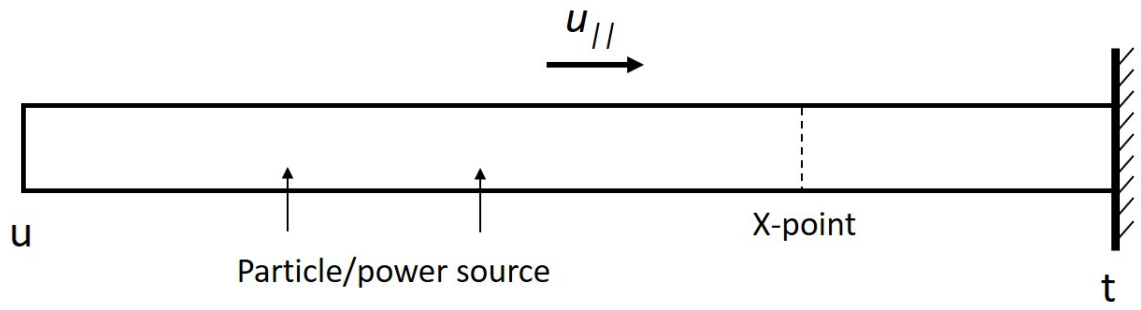

Figure 3.1: Illustration of SD1D simulation domain, modelling the SOl from stagnation point u to divertor target t. The X-point location and plasma flow $u_{||}$ direction are labelled.

condition on the plasma velocity

$$u_{||} \geq c_s = \sqrt{\frac{e(T_e + \gamma T_i)}{m_i}} \tag{3.41}$$

where γ is the ratio of specific heats (= 5/3 for adiabatic flow), and energy flow across the sheath boundary defined by

$$q_{e||} = \gamma_{SH} T_e n_i u_{||} \tag{3.42}$$

where γ_{SH} is the sheath heat transmission factor [42]. Boundary conditions at the target for n and p can be set to linear extrapolation of variables (free-floating), Neumann (zero-gradient) or constant flux conditions.

Recycling at the target plate is included in the model, creating a source for the neutrals at the target boundary. The recycled neutral flux is given by

$$\Gamma_n = -R_p \Gamma_i \tag{3.43}$$

where R_p is a user-specified recycling fraction. The injected neutrals are given a parallel momentum away from the target with a thermal speed corresponding to the Frank-Condon energy (3.5 eV) [43].

3.3 2D SOL modelling - UEDGE

UEDGE [78–80] is a 2-dimensional (2D) collisional edge-plasma transport fluid code that can be used for detailed 2D SOL simulation and analysis. The code solves a 2D form of the Braginskii equations, with the addition of ad hoc anomalous/turbulence-driven transport for the radial direction across the magnetic field using specified transport coefficients. Transport parallel to the magnetic field is classical (Braginskii/Spitzer-Härm), with flux limiters applied to prevent transport becoming unphysically large. The code equations are solved for variables of plasma density, plasma flow velocity, electron and ion temperatures and the electrostatic potential, and are solved on a curvilinear (or sometimes cartesian or cylindrical) mesh generated in the UEDGE code, based on poloidal flux surface data from an MHD equilibrium. In addition to the plasma species, UEDGE also includes a fluid-neutral model and can model plasma impurities either using its multi-species ion model or using a "fixed-fraction" impurity model. The discussion of the UEDGE code in this section closely follows that in References [79] and [80].

The 2D form of the Braginskii equations solved by the UEDGE code are a reduced set of Equations 3.15, consisting of five differential equations that couple five unknowns [81]: n_i, $u_{||}$, T_e, T_i, and ϕ in the poloidal plane, where ϕ is the electrostatic potential. The plasma electric field comes from $\mathbf{E} = -\nabla\phi$. The equations for plasma continuity, parallel momentum and energy are as follows:

- Ion continuity equation:

$$\frac{\partial}{\partial t}n_i + \frac{1}{V}\frac{\partial}{\partial x}\left(\frac{V}{h_x}n_i u_{ix}\right) + \frac{1}{V}\frac{\partial}{\partial y}\left(\frac{V}{h_y}n_i u_{iy}\right) = \langle\sigma_i v_{te}\rangle n_e n_g - \langle\sigma_r v_{te}\rangle n_i n_g \qquad (3.44)$$

  where x and y are defined for the poloidal and radial directions respectively. The terms $\langle\sigma_i v_{te}\rangle$ and $\langle\sigma_r v_{te}\rangle$ are reaction-rate coefficients for ionization and recombination respectively, calculated from data look-up tables based on plasma density/temperatures, and n_g gives the neutral density. Terms for $h_x \equiv 1/||\nabla x||$ and $h_y \equiv 1/||\nabla y||$ represent metric coefficents accounting for the local grid geometry, and $V = 2\pi R h_x h_y$ is the toroidal geometry volume element at major radius R. For brevity of presentation, the metric coefficients are not shown through the remaining equations. Assuming quasi-neutrality, $n_e = n_i$, and therefore the electron continuity equation is not required to be solved in addition to that for the ions.

- Ion parallel momentum equation:

$$\begin{aligned}\frac{\partial}{\partial t}(m_i n_i v_{i||})+\frac{\partial}{\partial x}\left(m_i n_i v_{i||}u_{ix}-\eta_{ix}\frac{\partial v_{i||}}{\partial x}\right)+\frac{\partial}{\partial y}\left(m_i n_i v_{i||}u_{iy}-\eta_{iy}\frac{\partial v_{i||}}{\partial y}\right)\\ =\frac{B_x}{B}\left(-\frac{\partial P_p}{\partial x}\right)-m_i n_g \nu_{cx}(v_{i||}-v_{g||})\end{aligned} \tag{3.45}$$

  where $P_p = P_e + P_i$ is the plasma pressure, $\eta_{ix} = (B_x/B)^2\eta_k$ is the classical viscosity, and $\eta_{iy} = m_i n \Upsilon_{ak}$ the anomalous viscosity. The inertialess electron momentum equation has been used to eliminate the parallel electric field and the ion-electron friction term, which are replaced by the P_e component of P_p [81]. $\nu_{cx} = n_i\langle\sigma_{cx}v_{ti}\rangle$ gives the hydrogen ion-neutral charge exchange frequency, and $v_{g||}$ is the neutral hydrogen parallel velocity. Flux-limiters are applied to all classical viscosities and thermal conductivities in order to prevent unphysically large values for conditions where mean-free-paths are long. These flux-limiters are user-defined, by setting values for limiter coefficients that define the maximum values these quantities can take. The choice of these coefficients is usually guided by previous kinetic simulation results.

- Electron energy equation [81]:

$$\begin{aligned}\frac{\partial}{\partial t}\left(\frac{3}{2}n_e T_e\right)+\frac{\partial}{\partial x}\left[C_{ex}n_e u_{ex}T_e-\kappa_{ex}\frac{\partial T_e}{\partial x}-0.71 n_e T_e\frac{B_x}{B}\frac{J_{||}}{e n_e}\right]\\ +\frac{\partial}{\partial y}\left(C_{ey}n_e u_{ey}T_e-\kappa_{ey}\frac{\partial T_e}{\partial y}\right)\\ =\left[u_{ix}\frac{\partial P_e}{\partial x}-u_{iy}\frac{\partial P_i}{\partial y}-u_{iw}\frac{B_x}{B}\frac{\partial P_e}{\partial x}\right]+\mathbf{E}\cdot\mathbf{J}-K_q(T_e-T_i)+S_{Ee}\end{aligned} \tag{3.46}$$

  The poloidal heat conductivity is given by the classical Spitzer-Härm conductivity in the direction of the field lines, $\kappa_{ex} = (B_x/B)^2\kappa_{||}$. The radial conductivity is anomalous, given by $\kappa_{ey} = n\chi_e$ where χ_e is a user-specified radial thermal transport coefficient, and K_q is the collisional energy exchange coefficient. The velocity u_{iw} is in the binormal direction to B and the radial direction ($\hat{\mathbf{i}}_{||}\times\hat{\mathbf{i}}_y$), only used when cross-field drifts are included. Convection coefficients $C_{ex,ey}$ take typical values of 5/2 or 3/2.

- Ion energy equation:

$$\begin{aligned}\frac{\partial}{\partial t}\left(\frac{3}{2}n_iT_i\right)+\frac{\partial}{\partial x}\left[C_{ix}n_iu_{ix}T_i-\kappa_{jx}\frac{\partial T_e}{\partial x}\right]+\frac{\partial}{\partial y}\left(C_{iy}n_iu_{iy}T_i-\kappa_{jy}\frac{\partial T_i}{\partial y}\right)\\ =[\mathbf{u}_i\cdot\nabla P_i]+\eta_{ix}\left(\frac{\partial v_{ij||}}{\partial x}\right)^2+\left(\eta_{iy}\frac{\partial v_{i||}}{\partial y}\right)^2\\ +K_{qj}(T_e-T_i)+\frac{1}{2}m_iv_{i||}^2n_i\nu_{iz}+S_{Ej}\end{aligned} \tag{3.47}$$

  Thermal conductivity and viscosity coefficients are again classical in the poloidal direction and are anomalous in the radial direction. $C_{ix,iy}$ take typical values of either 5/2 or 3/2 again also. The equation has an implied sum over the ion and neutral species using the j indicies, with $T_g = T_i$.

In the above equations, the poloidal ion velocity component is given by

$$u_{ix}=\frac{B_x}{B}v_{i||}+v_{x,E}+v_{ix,\nabla B}, \tag{3.48}$$

where the second term on the RHS is for the $\mathbf{E}\times\mathbf{B}/B^2$ drift and third term is the sum of the curvature and ∇B drifts. The radial ion velocity is given by

$$u_{iy}=-\frac{D_a}{n_i}\frac{\partial n_i}{\partial y}+V_a+v_{y,E}+v_{iy,\nabla B}+v_{iy,vis}, \tag{3.49}$$

where D_a and V_a are the user-specified anomalous particle transport coefficients characterizing turbulence-driven transport. The third and fourth terms on the RHS of Equation 3.49 are the radial components of the cross-field drifts as in Equation 3.48, and the last term is an anomalous viscous drift that gives a connection between the electrostatic potential on neighbouring magnetic flux surfaces. The electron velocities take the same form as for the ion velocities, including anomalous diffusion and convection terms as well as the terms for the cross-field drifts. The electron perpendicular viscosity is neglected due to their much smaller gyroradii.

The equation in UEDGE to solve for the electrostatic potential is obtained by the subtraction of the ion and electron continuity equations, assuming quasineutrality ($n_i = n_e$):

$$\nabla\cdot\mathbf{J}(\phi)=\frac{\partial}{\partial x}(J_x)+\frac{\partial}{\partial y}(J_y)=0 \tag{3.50}$$

where $\mathbf{J}$ is the current density (excluding the magnetization current) given by

$$\mathbf{J} = \left[ne(\mathbf{v}_{i,\nabla B} - \mathbf{v}_{e,\nabla B}) \cdot \hat{\mathbf{i}}_x + J_{||}\frac{B_x}{B}\right]\hat{\mathbf{i}}_x + ne(v_{i,y1} - v_{e,y1})\hat{\mathbf{i}}_y \tag{3.51}$$

where the parallel current density $J_{||}$ is

$$J_{||} = \frac{en}{0.51 m_e \nu_e}\frac{B_x}{B}\left(\frac{1}{n}\frac{\partial P_e}{\partial x} - e\frac{\partial \phi}{\partial x} + 0.71\frac{\partial T_e}{\partial x}\right), \tag{3.52}$$

and ν_e is the electron collision frequency.

Boundary conditions for the parallel ion velocity at the divertor target plates use the Bohm sheath condition, whose generalization to include $\mathbf{E}\times\mathbf{B}$ drifts is given by

$$u_{i||}\alpha + u_{Ew} = \pm\alpha c_s \tag{3.53}$$

where $\alpha \equiv |B_x/B| \ll 1$, c_s is the sound speed given by $c_s = [(T_e + T_i)/m_i]^{1/2}$, and u_{Ew} is the velocity component arising from $\mathbf{E}\times\mathbf{B}$ drifts. Energy boundary conditions at the targets are given in terms of the ion/electron energy fluxes $\Gamma_{Ei,e}$, where the energy fluxes at the target are given by

$$\Gamma_{Ei,e} = b_{Ei,e} n_i T_{i,e} u_{i,ex} \tag{3.54}$$

where $b_{Ei,e}$ are ion/electron energy transmission factors. These factors can be computed by the UEDGE code using the sheath potential condition, consistent with the parallel current at the plates.

The boundary condition for ϕ is determined by the sheath potential ϕ_s. The potential at the plasma sheath is $\phi_p + \phi_s$, with the target plate assumed to be conducting and at a potential ϕ_p, and ϕ_s is given by

$$\phi_s = \frac{-T_e}{e} ln\left[2\sqrt{\pi}\left(\frac{J_{||} - en_i u_{i||} - en_i u_{we}/\alpha}{en_i v_{te}}\right)\right] \tag{3.55}$$

where $v_{te} \equiv (2T_e/m_e)^{1/2}$ and u_{we} is the electron velocity component in the binormal direction $(\hat{\mathbf{i}}_{||} \times \hat{\mathbf{i}}_y)$.

Radial boundary conditions for the first wall and private flux region (PFR) can be set to Neumann or Dirichlet conditions for variables of n_i, T_e and T_i. This allows for their values to user defined at the boundary, or to be free-floating values with an "extrapolation"

condition on the variables. The parallel velocity at the boundary is typically taken to have zero radial derivative ($\partial u_{||}/\partial y = 0$), a "no-slip" condition so that v_i takes values consistent with nearby plasma dynamics. At the radial boundaries, ϕ is dominated by parallel currents, so a constraint on ϕ is employed by using boundary conditions of $E_y = 0$ and $\partial E_y/\partial y = 0$. On the core-edge boundary, particle and energy fluxes can be specified, or values of n_i, T_e and T_i can be specified along the boundary. The no-slip $\partial u_{||}/\partial y = 0$ is applied again, and ϕ is set to be poloidally constant, where the value of this constant is determined to ensure no net current through this boundary.

In addition to the plasma equations, the neutral model employed in UEDGE have their own set of fluid equations (where g labels hydrogen atoms):

- Neutral continuity equation

$$\frac{\partial}{\partial t}n_g + \frac{\partial}{\partial x}(n_g v_{gx}) + \frac{\partial}{\partial y}(n_g v_{gy}) = -\langle\sigma_i v_{te}\rangle n_e n_g + \langle\sigma_r v_{te}\rangle n_i n_g \tag{3.56}$$

- Neutral parallel momentum equation

$$\begin{aligned}&\frac{\partial}{\partial t}(m_g n_g v_{g||}) + \frac{\partial}{\partial x}\left(m_g n_g v_{g||}u_{gx} - \eta_{gx}\frac{\partial v_{g||}}{\partial x}\right) + \left(m_g n_g v_{g||}u_{gy} - \eta_{gx}\frac{\partial v_{g||}}{\partial y}\right)\\ &= \frac{B_x}{B}\left(-\frac{\partial P_g}{\partial x}\right) + m_i n_g \nu_{cx}(v_{i||} - v_{g||})\end{aligned} \tag{3.57}$$

  where η_{gx} and η_{gy} are the viscosities determined by charge-exchange collisions, given by $D_g = T_g/(m_g\nu_{cx})$ with T_g being the neutral gas temperature. Viscosities are again flux-limited to prevent unphysically large values in conditions of long mean-free paths. For the case of atomic hydrogen neutrals considered here, $m_g = m_i$.

As in the case for the ions, the neutral velocity has components for motion parallel to the B field as well as in the directions perpendicular to B from charge-exchange and ionisation processes. A simple diffusive treatment of the neutral transport gives the neutral velocity as

$$\mathbf{v}_g = -\frac{\nabla(n_g T_g)}{m_i n_g(n_i\langle\sigma_{cx}v_{ti}\rangle + n_e\langle\sigma_i v_{te}\rangle)}. \tag{3.58}$$

From this, the poloidal neutral velocity is given by

$$u_{gx} = \frac{B_x}{B}v_{i||} - \frac{B_z}{B}v_{gw} \tag{3.59}$$

where B_z is the toroidal B-field, and v_{gw} is the perpendicular component of $\mathbf{v}_{\perp g}$ in the binormal direction $(\hat{\mathbf{i}}_{||} \times \hat{\mathbf{i}}_y)$. And for the radial neutral velocity

$$u_{gy} = \hat{\mathbf{i}}_y \cdot \mathbf{v}_{\perp g}. \tag{3.60}$$

At the divertor plate boundaries, the incident ion flux is recycled as neutral gas, such that the poloidal neutral flux into the domain at the plates is given by

$$\Gamma_{n,x} = -R_p \Gamma_{i,x} \tag{3.61}$$

where R_p is a specified recycling fraction at the plate. The first wall and PFR boundaries can also be set to recycle incident radial ion fluxes as neutral gas, using the same Equation 3.61 in the y direction and a specified recycling fraction for these surfaces.

In addition to the plasma and neutral equations, UEDGE supports the inclusion of impurities and impurity transport with a multi-species fluid model, with each plasma species having their own set of fluid equations. However, in this study only the "fixed-fraction" impurity model will be employed - without impurity fluid equations and where the impurity species density is set to a specified fraction of the local plasma density - and therefore the impurity fluid model will not be detailed here.

3.4 Numerical methods

Both SD1D and UEDGE employ an implicit time stepping scheme, based on backward differentiation formula methods.

3.4.1 Backward differentiation formulae

Backward differentiation formulae (BDF) [82] are numerical integration methods used for stiff ordinary differential equations. These formulae are linear multistep methods that give an approximation to a derivative of a variable $y(t)$ at time t_n in terms of its function values at t_n and at earlier times. The simplest form of BDE is the backward Euler method, derived by considering the integration of the differential equation $\frac{dy}{dt} = f(t, y)$ from t_n to $t_{n+1} = t_n + h$,

$$y(t_{n+1}) - y(t_n) = \int_{t_n}^{t_{n+1}} f(t, y(t))dt, \tag{3.62}$$

where h is a timestep interval. Applying the right-hand rectangle method to the right hand side, and using that $y_n \approx y(t_n)$, the formula for the backward Euler method is obtained:

$$y_{n+1} = y_n + hf(t_{n+1}, y(t_{n+1})), \tag{3.63}$$

The backward Euler method is the first order BDF. Higher order BDF methods exist, given by the generalised formula

$$\sum_{k=0}^{s} a_k y_{n+k} = h\beta f(t_{n+s}, y(t_{n+s})), \tag{3.64}$$

where s is the order number, and a_k and β are coefficients depend on the method order. As an implicit method, the method requires the solution to a nonlinear algebraic equation for the unknown y_{k+s} term. This can be done using a variation of Newton's method.

3.4.2 Newton-Krylov method

3.4.2.1 Newton's method

Newton's method [83] is an algorithm that finds the roots of a real-valued function, starting from an initial guess and using this to find successively better approximations to the root over iterations. The most basic form of Newton's method can be illustrated with a single-variable function $f(x)$, where $f(x)$ is a differentiable function with values in real numbers. If we have a curret approximation x_n, then a formula for a better approximation can be derived using the equation for the tangent to the curve $y = f(x)$ at x_n, which is given by

$$y = f'(x_n)(x - x_n) + f(x_n) \tag{3.65}$$

where f' denotes the derivative of f. The x-intercept of this equation is taken as the next approximation x_{n+1}, such that

$$0 = f'(x_n)(x_{n+1} - x_n) + f(x_n). \tag{3.66}$$

Rearranging gives the solution for the next approximation as

$$x_{n+1} = x_n - \frac{f(x_n)}{f'(x_n)}. \tag{3.67}$$

Starting with an initial guess value of x_0, the Newton method will usually converge to the root, provided the initial guess is close enough to the unknown root, and $f(x)$ is well-behaved in the region and $f'(x) \neq 0$. For a multiplicity of 1 for the root, the convergence is at least quadratic, leading to fast convergence. However, convergence can fail if the initial guess is too far from the solution. In practice this can limit the timestep.

Newton's method can be generalised to solve systems of k unknowns and k nonlinear equations to find the roots of continuously differentiable functions F. Instead of dividing by $f'(x)$, it is necessary for this to left-multiply with the inverse of the Jacobian matrix $J_F(x_n)$, such that

$$x_{n+1} = x_n - J_F(x_n)^{-1} F(x_n) \tag{3.68}$$

where $F(x) = \{F^1, F^2, ..., F^i, ..., F^k\}$ and $x = \{x^1, x^2, ..., x^i, ..., x^k\}$. The Newton method iteration is terminated when the normalised residual drops below a specified tolerance, $\|F(x_n)\|/\|F(x_0)\| < \text{tol}_{res}$. The Jacobian matrix can be very large, and for nonlinear problems will change in time. The direct inversion calculation is slow (order n^3 in general), but can also have large rounding errors for large systems. It is therefore advantageous to avoid explicitly inverting or even calculating J_F if possible.

3.4.2.2 Krylov subspace methods

Krylov subspace methods [83] are iterative methods for solving large systems of linear equations of the form

$$Ax = b \tag{3.69}$$

where A is a matrix and x and b are vectors. The order-r Krylov subspace for a matrix A and vector b is the subspace spanned by the images of b for the first r powers of A:

$$K_r(A, b) = \text{span}\{b, Ab, A^2b, ..., A^{r-1}b\}. \tag{3.70}$$

Iterative methods utilising the Krylov subspace have the benefit that they avoid direct calculation of large matricies and working with matrix-matrix operations, instead only requiring matrix-vector products to carry out the iteration and working with the resultant vectors. The Generalised Minimal Residual method (GMRES) [84] is a commonly applied method that takes this approach, and there are a variety of other iterative methods that utilise a

Krylov subspace [83].

3.4.2.3 Newton-Krylov method

The Newton-Krylov method [83] allows for faster computation and execution of the Newton algorithm, by bypassing the calculation of the inverse Jacobian in the iteration formula and solving the equations in a Krylov subspace. Equation 3.68 can be re-written in the form

$$J_F(x_n)(x_{n+1} - x_n) = -F(x_n) \tag{3.71}$$

using the Jacobian matrix rather than the inverse-Jacobian. In this form the equation can be solved using a Krylov subspace method (such as GMRES) with the Jacobian matrix-vector product, which can be approximated for a vector v using a first-order Taylor expansion as

$$Jv \approx \frac{[F(x + \epsilon v) - F(x)]}{\epsilon} \tag{3.72}$$

where ϵ is a small perturbation. The benefit of using the Newton-Krylov method is that Newton-like nonlinear convergence of the solution can be obtained without the large computational cost of forming and storing the Jacobian matrix, only requiring the calculation of the Jacobian-vector product approximated by Equation 3.72.

3.4.3 SD1D - finite differencing methods

The SD1D model evolves the 1D model equation outlined in section 3.2 over time using the CVODE solver package [85], which solves stiff ordinary differential equation systems using backward differentiation formulae of varying order between 1 and 5. The nonlinear components in this method are solved for using various versions of a modified Newton's method or Newton-Krylov method, the latter using preconditioned Krylov iterative methods including GMRES, BiCGStab and TFQMR [85].

The model equations are solved on a 1D discretised grid (Fig. 3.2) using finite difference methods [74], with all variables defined at the same location on cell centres. Advection terms are solved using a flux-splitting MinMod upwinding method, where terms taking the form of $\nabla \cdot (\hat{\mathbf{b}} u f)$ are implemented as fluxes through cell boundaries:

$$\nabla \cdot (\hat{\mathbf{b}} u f) \approx \frac{1}{J \Delta y}[F_{i+1/2} - F_{i-1/2}] \tag{3.73}$$

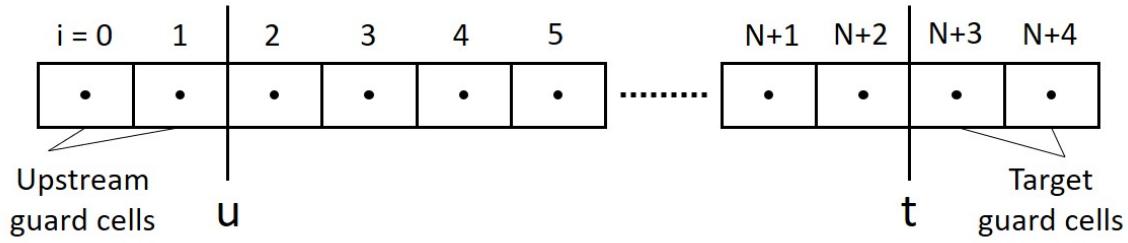

Figure 3.2: Diagram showing the SD1D simulation grid. The grid consists of N+4 cells in total, with N cells within the defined simulation domain and two guard cells either side of the domain boundaries. Plasma variables are defined on cell centres, and fluxes calculated through cell boundaries.

where F is the flux, f is the variable being advected, J is the coordinate system Jacobian (proportional to the cross-section area of the flux tube) and i is the cell number. Fluxes at the boundaries are calculated by linear interpolation of the velocities to the cell boundaries:

$$u_{i+1/2} = \frac{1}{2}(u_i + u_{i+1}), \tag{3.74}$$

with f being reconstructed on the left and right cell boundaries as f_i^L and f_i^R:

$$f_i^L = f_i - \frac{1}{2}s \qquad f_i^R = f_i + \frac{1}{2}s \tag{3.75}$$

where the slope s is limited using the MinMod method:

$$s = \begin{cases} 0 & \text{if sign } (f_{i+1} - f_i) \neq \text{sign } (f_i - f_{i-1}) \\ f_{i+1} - f_i & \text{if } |f_{i+1} - f_i| < |f_i - f_{i-1}| \\ f_i - f_{i-1} & \text{otherwise.} \end{cases} \tag{3.76}$$

Fluxes are then calculated from the upstream value of f:

$$F_{i+1/2} = \begin{cases} J_{i+1/2} f_i^R u_{i+1/2} & \text{if } u_{i+1/2} > c_s \\ J_{i+1/2} f_{i+1}^L u_{i+1/2} & \text{if } u_{i+1/2} < -c_s \\ \frac{1}{2} J_{i+1/2}[(u_{i+1/2} + c_s) f_i^R + (u_{i+1/2} - c_s) f_{i+1}^L] & \text{otherwise} \end{cases} \tag{3.77}$$

where c_s is the sound speed and $F_{i+1/2}$ has been split to handle waves propagating in different directions. All operators other than the advection terms are solved using second-order central

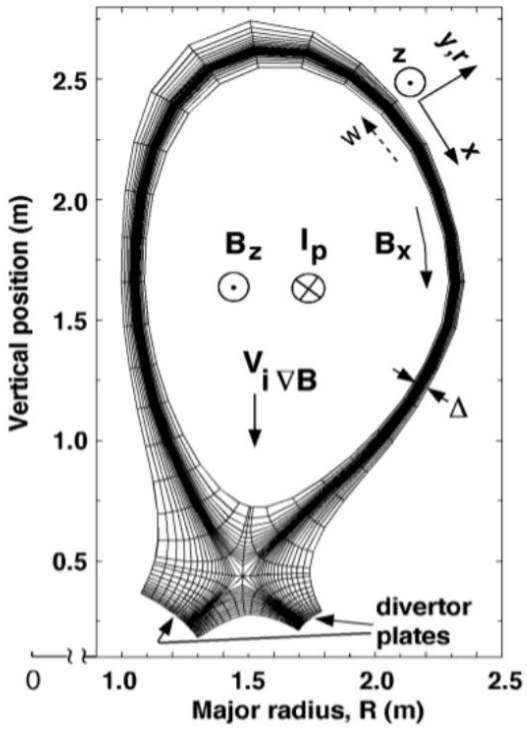

Figure 3.3: Example UEDGE simulation grid for DIII-D. Figure reproduced from [87].

differencing methods.

3.4.4 UEDGE - finite volume methods

A backward differential formula method and both Newton and Newton-Krylov iteration algorithms are implemented into the UEDGE code [80]. The model equations are solved using finite-volume methods on a 2D curvilinear mesh (eg. Fig. 3.3) generated by the code from MHD equilibrium data. Finite-volume methods [86], similar to finite difference methods, are methods for solving partial differential equations on a discretised mesh geometry, calculating variable values at cell centres using fluxes through the cell surfaces.

Consider a generalised partial differential equation

$$\frac{\partial \mathbf{u}}{\partial t} + \nabla \cdot \mathbf{F}(\mathbf{u}) = S \tag{3.78}$$

where $\mathbf{u}$ is a vector of state variables, $\mathbf{F}$ is the corresponding flux tensor and S is a source term. The spatial domain is sub-divided into finite cells, with cell index i. Taking the volume

integral over the volume of cell v_i, Equation 3.78 becomes

$$\int_{v_i} \frac{\partial \mathbf{u}}{\partial t} dv + \int_{v_i} \nabla \cdot \mathbf{F}(\mathbf{u}) dv = \int_{v_i} S dv. \tag{3.79}$$

Integrating the first term to get the volume average of the state variables $\bar{\mathbf{u}}_i$, and to the second term applying the divergence theorem

$$\int_V \nabla \cdot \mathbf{X} dV = \int_X \mathbf{X} \cdot \hat{\mathbf{n}} dX \tag{3.80}$$

where $\hat{\mathbf{n}}$ is the unit vector normal at the boundary pointing outward, this equation becomes

$$v_i \frac{\partial \bar{\mathbf{u}}_i}{\partial t} + \oint_{A_i} \mathbf{F}(\mathbf{u}) \cdot \hat{\mathbf{n}} dA = \int_{v_i} S dv. \tag{3.81}$$

where A_i represents the surface area of cell i. Integration of S becomes trivial if source terms are considered to be constant across the cell volume. As with the finite difference method previously, fluxes and variable values at the boundaries can be reconstructed by interpolation.

Chapter 4

ARC reactor

4.1 Compact fusion reactor concept and ARC design

The ARC reactor [17] (Affordable, Robust, Compact reactor) is a conceptual tokamak design for a reduced size, cost and complexity demonstration fusion pilot power plant, proposed by reseachers at MIT. A 3D design projection is shown in Figure 4.1. It is designed to operate at a fusion power comparable to ITER of ∼500 MW, but doing so at a compact size, with major radius of $R_0 = 3.3$ m, comparable to JET [17]. In contrast to ITER, however, ARC would be a net-energy producing machine, producing 200-250 MWe. The key physics that allows the design to achieve this high fusion power at such a compact size relies on new High-Temperature Superconductor (HTS) technology, that enable higher magnetic field operation. The ambition in this design choice was that a compact, high magnetic field, superconducting device might offer access to both high fusion gain Q as well as net electric gain $Q_e > 1$.

One of the key motivations for ARC is the desire to reduce the cost and time it takes to construct large fusion experiments and future pilot plant reactors, to accelerate the development of fusion as a viable energy source. Size is a key driver of reactor cost - with materials costs scaling with volume and fabrication costs scaling with large components that require specialist manufacturing. The cost of large fusion projects such ITER run into the 10s of $billion. Devices of smaller size and more modest cost, it is argued, allow for more rapid progress and development cycles for fusion devices, enabling fusion energy to be achieved in a faster timeframe. One of the main goals for the authors of the ARC design study was therefore to minimise the reactor size.

Fundamental to the design of any magnetic fusion reactor is the scaling equation [5] for

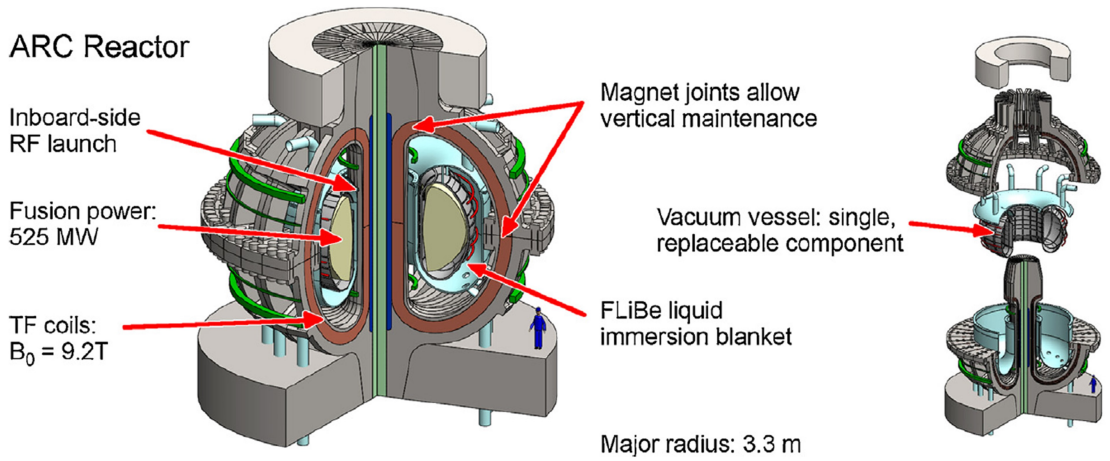

Figure 4.1: 3D ARC reactor design projection, with demountable toroidal magnetic field coils [17]. Figure reproduced from Reference [17] with permission from the authors.

fusion power P_f (for constant aspect ratio),

$$P_f \propto \beta_N B_0^4 R_0^3 \tag{4.1}$$

where β_N is the normalised plasma beta. The strategies that emerge from this scaling to maximise P_{fus} are therefore: (1) to increase β_N, (2) increase the magnetic field B_0, or (3) increase the reactor size R_0. Increasing β_N comes at the risk of exciting MHD modes [88] and increasing the frequency of disruptions in devices if increased close to or past its intrinsic β_N limit ($\beta_N \approx 2.8\%$ [89]). Previously, limits in the technology for the toroidal field (TF) coils and the currents they could sustain was seen as a major obstacle to the high B_0 strategy, and hence the high R_0 approach has been the strategy that motivates the ITER and future DEMO designs. However, the introduction of HTS TF coils, which can carry significantly higher critical current densities, may prove a game-changer in the ability to unlock the high B route to fusion power [19]. Maximising the fusion volumetric power density $\frac{P_f}{V_P} \propto \beta_N B_0^4$, which ultimately reduces the required size of the reactor, is a requirement for achieving economical fusion power plant designs.

The HTS coils in the ARC design use REBCO (Rare Earth Barium Copper Oxide) superconducting tape. High temperature superconductors can achieve superconductivity at much higher critical temperatures than conventional low-temperature superconductors (LTS) (>80 K as opposed to <30 K). REBCO superconductors have significant advantages

over LTS materials, including a larger tolerance in operating temperature, ability to deal with higher resistive heat loads within the coil, and significant reductions in the required cryogenic power required to maintain superconducting temperatures [18]. REBCO HTS can also achieve much higher critical current densities than standard Nb_3Sn superconductors, and can do so in high local magnetic field conditions, making them attractive as a fusion TF coil material that can permit significantly higher B_0 operation [18], essential for small reactor designs.

Another novel feature of the ARC reactor design that is enabled by the REBCO coils' ability to support resistive joints (with resistance $\sim$2 nΩ [90]) is that the TF coils can be made demountable [18]. Figure 4.1 shows locations of proposed joints at the top and middle of the TF coils, allowing the coils to be detached, and the entire inner vessel can be lifted into and out of position as a singular modular component. With conventional TF coils technology, in construction of a tokamak the vessel must be built in segments, and the TF coils must be large enough for these segments to slot between them for assembly. With demountable coils/joints this is no longer necessary, meaning the TF coils, which are the most expensive component of a reactor [91], can be made smaller [17]. The ability to make the vacuum vessel as a singular module also presents great potential benefits: the simplicity of construction and testing of components is greatly increased, and the relative ease and speed at which the vessel can be installed or removed with the TF coils detached minimises the maintenance that must be performed within the TF volume, and allows greater ease for replacing and repairing damaged components. In addition, the modular nature allows ARC to test a variety of different vacuum vessel configurations, testing different materials, components, divertor designs etc. This allows ARC to be flexible as a Fusion Nuclear Science Facility (FNSF), allowing more speculative and innovative designs to be tested.

The key ARC reactor parameters that resulted from the design effort are given in Table 4.1, reproduced from Table 1 in Reference [17]. These parameters puts ARC well within the four principal stability conditions: edge safety factor (kink limit) [92], Greenwald fraction (density limit) [93], normalized beta (pressure limit) [88], and elongation limits [94, 95]. This should result in greater core plasma stability and make ARC less prone to disruptions, minimising damage of internal components from disruption events, which need to be avoided as a tokamak FNSF/Pilot plant.

In terms of confinement regime, ARC is designed to operate in I-mode [96] - an improved

Design parameter	Symbol	Value
Fusion power	P_f	525 MW
Total thermal power	P_{tot}	708 MW
Plant thermal efficiency	ν_{elec}	0.40
Total electrical power	P_e	283 MW
Net electrical power	P_{net}	190 MW
LHCD coupled power	P_{LH}	25 MW
ICRF coupled power	P_{IC}	13.6 MW
Power multiplication factor	Q_e	3.0
Major radius	R_0	3.3 m
Plasma semi-minor radius	a	1.13 m
Plasma elongation	κ	1.84
Plasma volume	V_P	141 m^{-3}
Toroidal magnetic field	B_0	9.2 T
Peak on-coil magnetic field	B_{max}	23 T
Plasma current	I_P	7.8 MA
Bootstrap fraction	f_{BS}	0.63
Tritium breeding ratio	TBR	1.1
Avg. temperature	$\langle T \rangle$	14 keV
Avg. density	$\langle n \rangle$	1.3 x 10^{20} m^{-3}
On-axis temperature	T_0	27 keV
On-axis density	n_0	1.8 x 10^{20} m^{-3}
Greenwald fraction	f_{Gr}	0.67
Toroidal beta	β_T	1.9%
Internal inductance	l_i	0.67
Normalised beta	β_N	2.59
Safety factor at $r/a = 0.95$	q_{95}	7.2
Edge safety factor	q_a	4.7
Minimum safety factor	q_{min}	3.5
Fusion power wall loading	P_f/S_b	2.5 MW/m^2
Energy confinement time	τ_E	0.64 s
H89 confinement factor	H_{89}	2.8
H98(y,2) confinement factor	$H_{98,y2}$	1.8
G89 gain factor	G_{89}	0.14

Table 4.1: List of significant ARC design parameters. Table reproduced from Reference [17] with permission from the authors.

confinement regime which possesses H-mode-like energy confinement but with L-mode-like particle confinement [96], with a corresponding pedestal in the temperature profiles and lack of a pedestal for the density. The L-mode-like particle confinement has significant advantages for a reactor operating mode, allowing for quicker removal of impurities from the core plasma (e.g. helium ash), and critically prevention of build-up of impurities [97] and lack of density pedestal [98] means that ELMs do not occur. ELMs are violent outbursts of particles and energy from the core into the SOL, which cause significant damage to plasma-

facing components. They need to be avoided or mitigated in a reactor scenario, so operating in an ELM-free regime makes I-mode attractive. I-mode does have it's own high-frequency instability, the weakly coherent mode, however these are much weaker in energy output than ELMs [99]. To access I-mode, the magnetic field needs to be setup in the unfavourable $B\times\nabla B$ configuration (where the ion $B \times \nabla B$ drift points away from the primary X-point, which has a higher power threshold for L-H transitions [99]), which allows transition to I-mode as an intermediate mode between L-mode and H-mode, rather than transitioning straight from L-mode to H-mode in the favourable Bx∇B configuration. The window for accessing I-mode before it transitions to H-mode is wider as magnetic field strength is increased, making I-mode operation a good match for the high-field ARC design [99].

The core temperature and density profiles for ARC in Reference [17] were generated using experimental scalings based on Alcator C-Mod I-mode profiles. To calculate the density profile, the authors set an almost triangular profile to achieve $n_0/n_{e,average}$ ~1.3, equal to the average of the C-Mod data [96] from 0< ρ <1, where $\rho = r/a$. The line-averaged density was kept below 90% of the Greenwald density limit. The gradient was rolled off to zero inside of $\rho = 0.05$, and at the plasma edge the constant slope dn/dr is extended to $\rho = 1$. This is applicable to ARC as it is consistent with the lack of a particle transport barrier in the edge that is characteristic of I-mode (and makes it distinct from H-mode). These properties give ARC an edge density at the separatrix of 1x10^{20} m^{-3}. The electron temperature profile was constructed inwards from $\rho = 1.0$, with the edge temperature being set to 200 eV (based on parallel heat conduction limits of the two-point model [100]), and experimentally observed C-mod scalings for ∇T in regions 0.95< ρ <1.0 and 0< ρ <0.95 used to construct the profiles inwards from there. The final density and temperature profiles obtained by the authors are shown in Figure 4.2. There is substantial uncertainty in assuming that C-mod data and gradient-scalings will scale to a reactor like ARC, particularly given that ARC will operate in very different power regimes. The use of the two-point model to estimate the edge temperature of 200 eV is questionable also - high-power devices like ARC are likely to have a low collisionality SOL, violating assumptions of the two-point model that would typically lead to underestimates for the upstream separatrix temperature. However, without reason to suggest otherwise it is assumed that the profiles/scaling obtained in C-Mod are plausible for ARC. How sensitive the ARC design and performance is to the assumed profiles is unclear.

It is natural to draw comparisons for ARC with the ITER tokamak, given it also produces

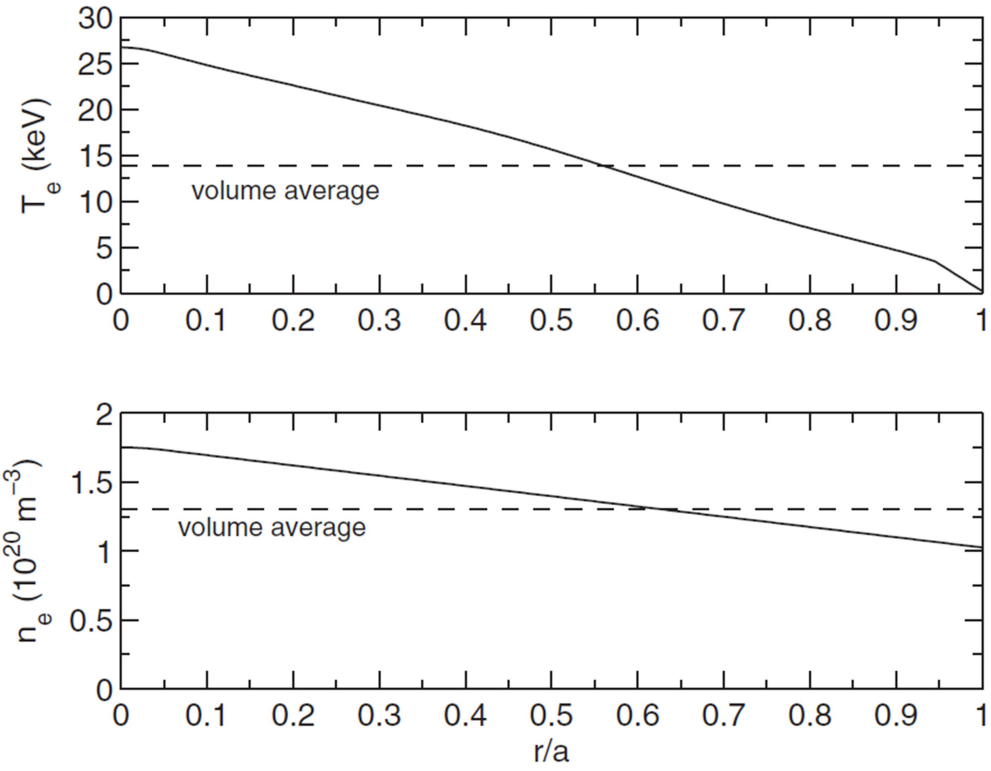

Figure 4.2: Radial profiles of electron temperature (top) ad electron density (bottom) in ARC. Figure reproduced from Reference [17] with permission from the authors.

a similar total fusion power (500 MW) with a similar shaping ($a/R \sim 0.33$), but doing so at a lower magnetic field $B_0 \sim 5.3$ T and a significantly larger size ($R_0 = 6.2$ m). ARC is able to achieve this same high fusion power at reduced size due to the high B_0 enabled by the REBCO HTS technology, as already discussed. But the ARC design is able to go beyond the design goals of ITER, with the REBCO HTS technology allowing ARC to be a net-energy producing device that achieves a FNSF/pilot-plant-relevant areal fusion power density (∼3 MW/m^2) in a device with roughly a tenth of ITER's volume. Additionally, as a result of the high toroidal field, the ARC design has double the safety factor of ITER, making it more robust against disruptions [17]. This also permits a high bootstrap fraction of ∼63%, while staying below the beta limit, a desirable quality for improving current drive efficiency and getting to high Q necessary for a pilot power plant device.

Whilst the ARC reactor is an interesting design with a number of attractive features, it is important for it to be to viewed in the context of the significant challenges it faces before the design as outlined in Ref [17] is feasible. Principal amongst these is the HTS technology and

demountable coil joints; these are unproven technologies in the infancy of their development, with unique challenges compared to conventional LTS coils. The grain orientation of the superconductor material creates anisotropies in the superconducting properties of the REBCO tapes in the presence of external magnetic fields; the critical current I_c can be degraded by factor 4-5 for perpendicularly aligned B-field [90, 102], which compromises the high-field capabilities of the HTS coils. The performance of the HTS coils under neutron irradiation is also a concern - experiments show I_c drops below the non-irradiated state for neutron fluxes $\geq$3x10^{22} m^{-2} (with neutron energies well below the 14 MeV value for DT fusion) [103] and compared to LTS materials HTS have a lower threshold to neutron irradiation damage [90], so ensuring the coils can be adequately shielded in a high fusion power reactor environment becomes a concern. In addition, quench events - localised termination of the magnet superconducting properties that return to the normal resistive state, creating 'hot-spots' that can cause burnouts of the HTS coil - need to be detected and controlled, with adequate quench protection systems still to be developed [90]. The HTS joint technology in particular is at an early stage of development for application to fusion TF coils, and there remain serious questions as to the ability to successfully restore the connections and electrical insulation between hundreds of coil windings with every 'remounting' [90], as well as for the continuity of the mechanical support structures required for the coils/joints to survive the large electromagnetic forces on the coils associated with the high-field/current operation [17, 90]. Many aspects of the ARC design depend on the features enabled by the HTS coils/joints, and therefore this technology needs significant further development and to be demonstrated on a large scale before they can be successfully applied to the ARC TF coils.

In addition to the HTS challenges, a number of aggressive assumptions are made for the ARC physics and technology [17]. The $H_{98,y2}$ confinement factor of 1.8 quoted in Table 4.1 is very high, that not even high-performance H-modes have yet achieved [104]. To achieve the 200-250 MWe net power quoted for the device, this would require recovery of some of the thermal power from the divertor, which is challenging with current technology. A lower hybrid current drive (LHCD) system is employed in the design for efficient current drive at mid-radius positions, but the LHCD system specified at 8 GHz in the ARC design has yet to be demonstrated [17]. The breeder blanket material, liquid FLiBe, has favourable thermodynamic and neutron irradiation properties for a reactor but is intrinsically corrosive, and how this will impact vacuum vessel and blanket tank lifetimes is not well understood [17].

Whilst it is not uncommon to assume improvements in state-of-the-art technology when considering future reactor designs, the outlined issues show that significant R&D advances are required in order for the ARC design to be a success.

4.2 ARC divertor design

In the original ARC design paper [17], it was not attempted to incorporate a divertor or power exhaust solution at that stage. Some consideration was given to how the ARC exhaust challenge compared to other current and future devices using a simple metric, $P_{SOL}/2\pi R_0 \lambda_{SOL}$. Given λ_{SOL} is not known with any certainty for future machines, this metric is split into an upper and lower limit: upper limit given by $\lambda_{SOL} \sim 1/B_p$ (Eich scaling [21]), and lower limit assuming $\lambda_{SOL} \sim 2\pi a\sqrt{(1+\kappa^2)/2}$ (pressure limited SOL [101]). Results of this comparison are given in Table 4.2, with the metrics shown in the last two rows. These results indicated that the challenge facing ARC in power exhaust will be greater than that for ITER, but less than some commerical power plant designs (appropriate for a pilot-plant).

	ARC	ARIES-AT	JET	C-Mod	ITER
Major radius, R_0 (m)	3.3	5.2	2.92	0.67	6.2
Aspect ratio, $\frac{1}{\epsilon}$	3	4	3.07	3.05	3.1
Minor radius, a (m)	1.13	1.3	0.95	0.22	2
Elongation, κ	1.84	2.2	1.81	1.68	1.75
On-axis magnetic field, B_0 (T)	9.2	5.8	3.6	5.4	5.3
Plasma current, I_p (MA)	7.8	12.5	4	1.5	15
P_{heat} (MW)	143	389	28.9	8	150
$1/B_p$ (T^{-1})	1.07	0.89	1.74	1.01	0.95
$P_{SOL}B_p/R_0$ (MW*T/m)	41.0	84.2	5.69	11.8	25.5
P_{SOL}/S_p (MW/m^2)	0.67	0.85	0.18	1.00	0.21

Table 4.2: Inter-machine comparison of divertor heat-loading metrics. S_p is the plasma surface area, $S_p = 4\pi^2 a R_0 \sqrt{(1+\kappa^2)/2}$. Table reproduced from Reference [17] with permission from the authors.

A follow-on study [105] has since been performed to address the incorporation of a divertor and power exhaust management into the ARC design. The goal of this study was to "explore and exploit these features for heat exhaust management with a conceptual design that includes an advanced divertor, while also retaining the essential features of the original ARC design: overall plasma geometry (major radius, minor radius, elongation), double-null divertor magnetic topology, demountable toroidal field (TF) coils, FLiBe liquid immersion blanket, and 525 MW DT fusion power" [105]. The paper also highlights the point that

the study focused on steady-state operation, not addressing issues ARC may face during start-up/shut-down phases or during disruptions.

Key to this study was the implementation of the divertor. Anticipating the increased heat flux challenge of ARC over conventional divertor technology and configurations in ITER, an advanced divertor was deemed necessary. The configuration chosen was a long-legged, tightly baffled geometry, with a magetic geometry for an X-point Target Divertor (XPTD) configuration. The XPTD was chosen for the previous success observed in UEDGE modelling results for this configuration. Modelling of this concept for the ADX (Advanced Divertor eXperiment) divertor test tokamak indicated that it could access passively stable, fully detached divertor regimes over a broad range of parameters [112]. A factor of 10 enhancement in peak power handling compared to conventional divertors has been obtained in some cases.

The resulting divertor design from this study [105] is shown in Figure 4.3. The ACCOME MHD equilibrium code [106] was used to generate the desired magnetic equilibria, iterating through coil placements and currents to produce a design that met the design goals of the divertor implementation. The final coil positions are shown in Figure 4.3. Open and closed magetic flux surfaces are shown inside the vacuum vessel volume, showing the double null configuration and the secondary magnetic X-points at the end of the long leg divertor channels. These long leg divertors were implemented by carving out space from the FLiBe blanket that existed in the original ARC design, meaning this did not affect TF coil size or core plasma volume. This was achieved whilst still retaining a tritium breeding ratio greater than 1 (only a minor reduction from 1.1 to 1.08 [105]), and with the FLiBe blanket still providing the necessary shielding to not impact coil lifetime estimates. In addition, the increased length of the divertor leg was found to reduce the high-energy neutron flux in the divertor significantly, which would reduce neutron damage to the divertor and extend component lifetime. This arises from the advantage in geometry of placing $\sim$1 m of FLiBe along the line-of-sight for neutrons in the core plasma and the divertor [105].

Previous work by Lackner and Zohm [107] had called into question the practicalities of incorporating advanced divertor configurations into reactor designs, on the basis that they would occupy too much volume inside the toroidal field coils, or the arrangement of poloidal field coils needed to produce them would be incompatible with coil current limits and/or neutron shielding requirements. The approach taken in the development of the ARC divertor design in Figure 4.3 demonstrates how these problems may be potentially overcome.

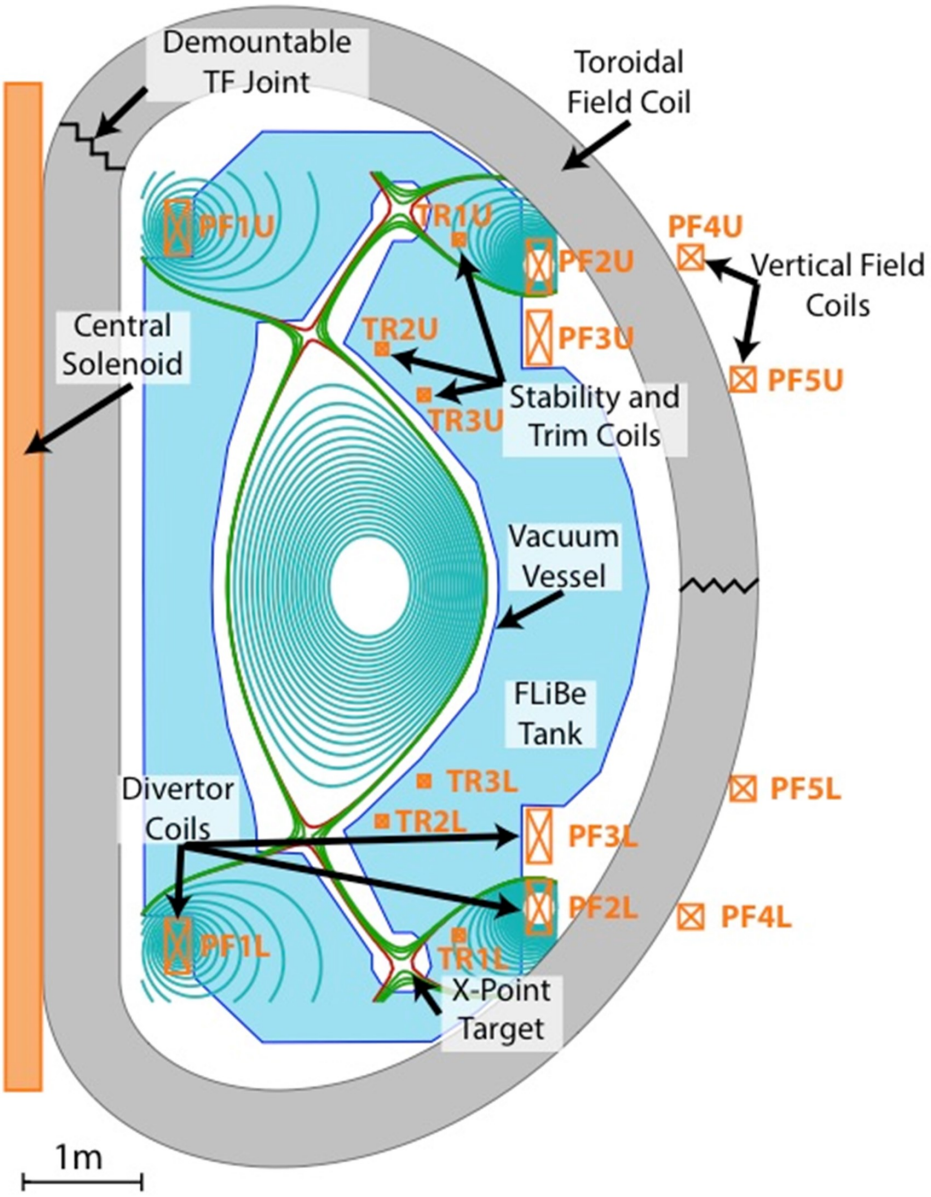

Figure 4.3: Schematic diagram of the proposed ARC long-legged X-point target divertor [105], with closed (blue) and open SOL (green) magnetic field lines shown. Figure reproduced from Reference [105] with permission from the authors.

In particular the HTS technology is key to this, with their ability to support resitive joints and segmentation of the TF coils, allowing for the PF coils to be placed inside the TF coil volume whilst still being sufficiently shielded to neutron damage by the blanket. Many tokamaks have PF coils placed within the TF coils, such as DIII-D [108], Alcator C-Mod [109] and TCV [110], which are used to enhance plasma shaping capabilities, which is necessary to facilitate the incorporation of the complex XPTD magnetic geometry.

The 'Eich scaling' - the empirical scaling for H-mode power decay width $\lambda_{q||}$ - predicts a $\lambda_{q||}$ of only ~ 0.4 mm for the ARC reactor [21]. At first glance this would make it appear that the divertor challenge in ARC is more severe than in lower field tokamaks, which will have intrinsically larger $\lambda_{q||}$ due to the $B_T^{-0.8}$ dependence of the Eich scaling - referring back to the $P_{SOL}B_p/R_0$ metric in Table 4.2 we see the ARC exhaust challenge quantified by this metric is significantly greater than that for current devices or ITER. However, a detailed study by Reinke [111] shows that high B enables access to higher core and edge densities, by enabling operation at higher plasma current I_p without violating safety factor q limits and hence increasing the Greenwald density limit $n_G \sim I_p/\pi a^2$, which is a significant benefit for achieving detached divertor operation. Taking the case of ARC, its high magnetic field allows it to attain the areal power density needed for a reactor ($\sim$2.5 MW m^{-2}) based on economic considerations but at significantly reduced total power levels [19] and consequently total power exhaust levels. The total exhaust power for ARC is estimated to be only $\sim$ 93 MW [105], assuming a 35% core radiation fraction. The net effect is that the parallel heat flux entering into the divertor is expected to be similar to that of larger, low field devices (12 to 40 GW/m^2) that achieve similar areal power loading, despite the smaller $\lambda_{q||}$. So to a first approximation, it is argued, that power exhaust in ARC may be neither more nor less difficult than in much larger devices with similar mission (net-energy production) and lower field.

However, despite these arguments, it was not at all obvious that any plausible divertor heat flux handling scenario will be possible in the ARC reactor, without implementing excessive levels of impurity seeding. In addition, whilst the XPTD may have shown a factor of 10 enhancement in peak power handling compared to conventional divertors in the ADX study, the question remains as to how the XPTD will actually perform in the context of a reactor such as ARC. It is therefore necessary to perform a full modelling study of the ARC edge plasma and divertor response, to explicitely model the ARC SOL thermal transport in order to fully assess the viability of the ARC reactor power exhaust handling solution. The next chapter presents the first study (and its results) attempting to model the ARC SOL and make this performance assessment, first for a simplified Super-X divertor configuration (SXD) and then for the actual X-point target divertor (XPTD) being proposed.

Chapter 5

ARC Divertor Modelling

5.1 UEDGE ARC SOL physics model

The tool used to perform this divertor study for ARC is the 2D edge transport code UEDGE. UEDGE is a well-established edge fluid simulation code [78, 79, 113], which has been extensively used for interpretation of tokamak edge data [114–116] and for modelling of advanced divertors [117]. Most recently, UEDGE has been applied to modelling X-point target divertors in the ADX (Advanced Divertor eXperiment) concept [112], making it an ideal tool for extending the study of X-point target divertors to ARC.

The ARC design study employed the ACCOME MHD equilibrium solver [118,119], which allows for a self-consistent computation of magnetic equilibria accounting for non-inductive current drive. The reference magnetic equilibrium used for this study corresponds to the ARC operation design point described in Chapter 4 and Reference [105], with poloidal coils currents specified in Table 1 and power exhaust in Table 8 of that reference.

ARC employs an upper- and lower-divertor configuration for double-null operation (Figure 4.3). The magnetic equilibria data from ACCOME (generated by Dr Brian LaBombard) were converted to a UEDGE gird format (primarily by Dr Maxim Umansky) and used to implement a lower-half-domain ARC geometry into UEDGE for two divertor setups: a) Super-X Divertor (SXD), and b) secondary X-point target divertor (XPTD). Figure 5.1 shows UEDGE grids generated for each case. Both configurations are considered in these modelling studies to see how they compare with each other for ARC. For exploration of the XPTD magnetic geometry (discussed in Section 4), currents in poloidal field coils PF2L and PF2U were varied about the design point value, generating magnetic equilibria with AC-

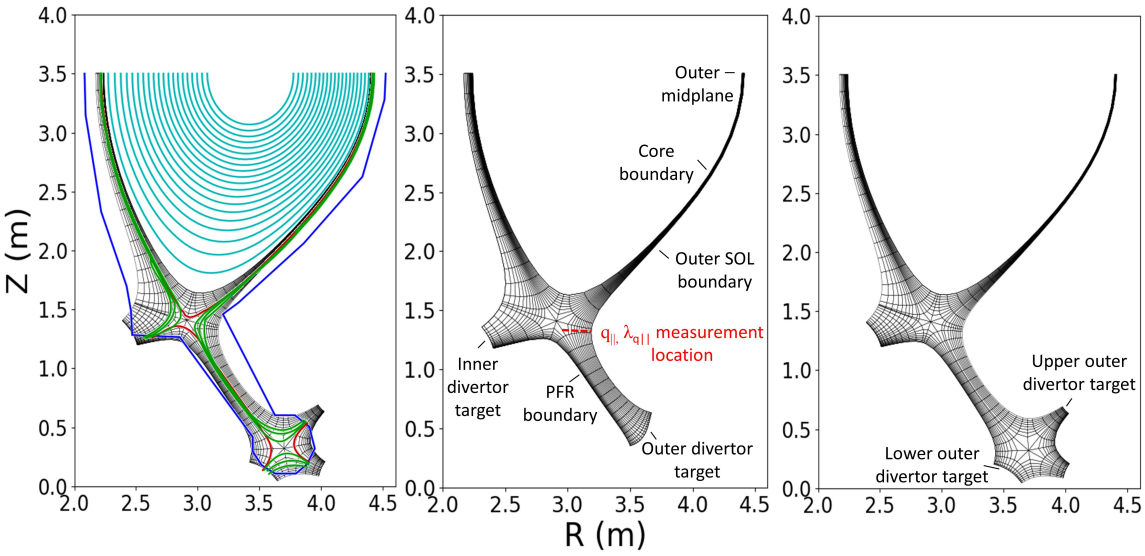

Figure 5.1: Schematic diagram of UEDGE ARC SOL/divertor grid mapped over ARC magnetic geometry (left), with closed field lines given in cyan, open SOL field lines shown in green and red, and the location of the reactor first wall given by the blue line. Plots of simulation grids for the SXD (middle) and XPTD (right) geometries, with labelled simulation boundaries and midplane location shown. The parallel heat flux profile $q_{||}$ (sum of ion and electron contributions) entering into the divertor and its characteristic e-folding width, $\lambda_{q||}$, is measured at the location of the red dashed line.

COME that produced UEDGE grids with magnetic separation between main and divertor X-point flux surfaces varying from 1.6 to 0.5 mm, mapped to the outer midplane.

In the UEDGE model for ARC used here, the radial particle transport is specified by a diffusion and convection model, given by the equation:

$$\Gamma_{\perp} = -D\nabla n + v_{conv} n \tag{5.1}$$

where $\Gamma_{\perp}$ is the radial particle flux density, D is the diffusion coefficient and v_{conv} is the convective pinch velocity. This form of combined diffusion and convection velocity for anomalous radial transport has been previously used in UEDGE modelling studies [120]. Radial electron/ion energy transport is simulated by a diffusive model, with a specified diffusion coefficient profile, $\chi_{i,e}$, taking the simplifying assumption that the ion and electron thermal diffusivities are equal.

The ARC operational design point parameters [17] combined with empirical characterizations of transport behavior in the SOL and divertor were used to determine plausible values for D, v_{conv} and $\chi_{i,e}$. ARC is designed to operate in I-mode [96] - an improved confinement

regime with energy confinement comparable to H-mode but with particle confinement similar to L-mode, with a corresponding pedestal in the temperature profiles and lack of a pedestal for the density. The thermal and particle transport models were therefore tuned to produce midplane density and temperature profiles that are representative of I-mode on the basis of what is observed in Alcator C-Mod and plausible for ARC.

The SOL density profile in Alcator C-Mod has been well documented [121,122] in a variety of regimes - L-Mode, EDA H-Mode, and ELM free H-modes - and certain features like the formation of a density shoulder on the low field side were found to always be present, resulting in a "main-chamber recycling" regime at higher densities [123]. The underlying mechanism is associated with the ballistic motion of interchange-unstable filamentary plasma structures that form in the edge [124]. A large body of experimental evidence accumulated from many tokamaks and other devices [125] indicate that this ubiquitous phenomenon should also appear in ARC. To reproduce these features for the ARC simulations, the diffusion coefficient D was set to 0.025 $m^2 s^{-1}$ throughout the domain, and a profile for v_{conv} was adjusted to produce a targeted midplane density profile: last-closed-flux surface (LCFS) density at the ARC design value of $n_{LCFS} \sim 10^{20}$ m^{-3}, a decay length of $\lambda_n \sim 5.5$ mm, and a flattened density profile ("density shoulder") at 10 mm radial distance into the SOL (see Figures 5.2 and 5.3). This SOL density profile and separatrix value are based on I-mode density profile data that has previously been obtained in Alcator C-Mod under high-field operation [96]. Data from Alcator C-mod is particularly applicable (compared with other machines) in the context of ARC, since it was able to access the high-B and high-density conditions relevant to the ARC design (albeit at lower power), and I-mode shot data with upstream profiles was available that showed/justified the features in the density profile described (again with the caveat that the I-mode shot was at much lower power than in ARC). Whilst there is substantial uncertainty in assuming these profiles will scale to a reactor like ARC, in the absence of reason to suggest otherwise we assume what has been achieved in Alcator C-Mod will be attainable in ARC for the purpose of this study. Noting that the core density is at a Greenwald fraction of 0.67, we explore the effect of increasing the separatrix density above this design point value in Section 5.4. The assumptions of operating in I-mode, with L-mode-like particle confinement and no pedestal in the core density profile as mentioned above, motivate the ARC separatrix density of 10^{20} m^{-3}, equal to the edge density of the core profiles given in [17]. Based on the sensitivities found, the divertor challenge would be

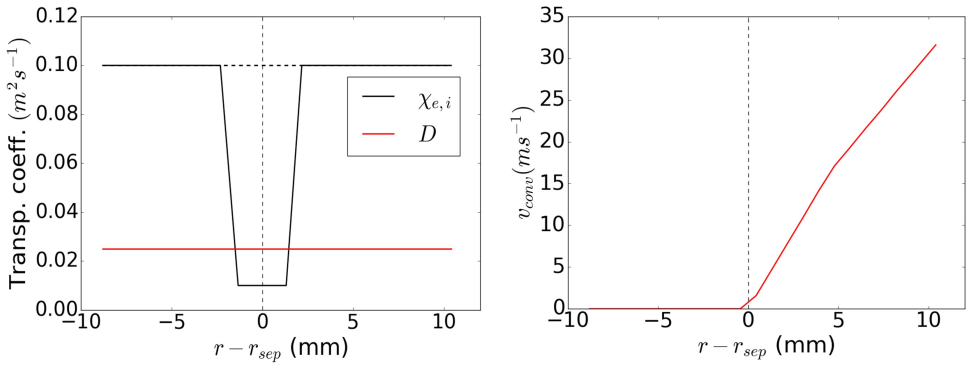

Figure 5.2: Outer midplane profiles for D, $\chi_{i,e}$ and v_{conv} defined for the UEDGE transport model, plotted as a function of distance from the separatrix into the scrape off layer when mapped to the outer midplane.

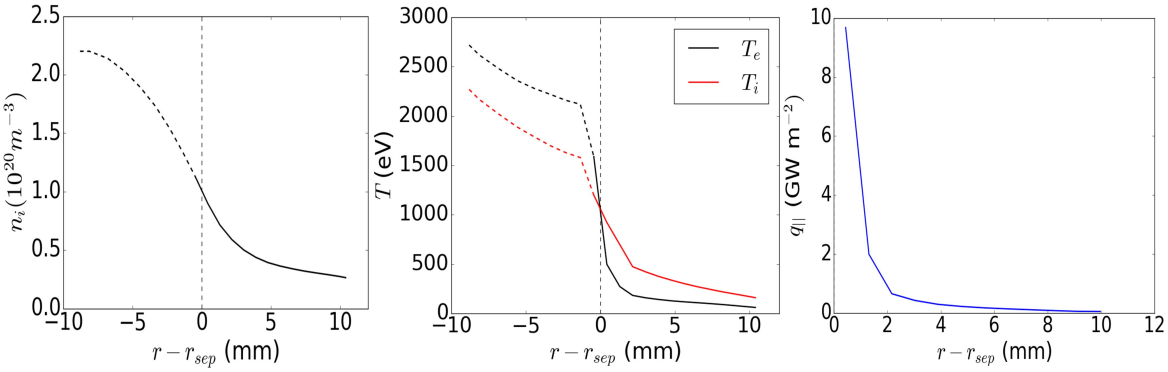

Figure 5.3: Outer midplane profiles for n, T_e and T_i, as well as $q_{||}$ profile at the primary X-point location (see Fig. 2), produced for the ARC I-mode model, plotted as a function of distance from the separatrix into the scrape off layer when mapped to the outer midplane. The dashed line sections inside the separatrix do not represent the core profiles postulated in ARC, but instead serve to establish the required boundary conditions at the separatrix. Parameters are shown for a SXD simulation. For this case, the peak value of $q_{||}$ entering into the divertor is approximately 10 GW m^{-2}, with $\lambda_{q||} \sim 0.55$ mm.

clearly more severe at lower separatrix density, as may be obtained with a H-mode plasma assuming a separatrix density that is 1/3rd of the core density [126].

Experimental evidence of plasma blobs in the divertor region [127, 128] indicate that the transport physics of the upstream SOL - interchange dynamics driven by the magnetic curvature and plasma pressure gradient - is also at play in the divertor leg. We therefore apply the v_{conv} profile shown in Figure 5.2 uniformly along the magnetic flux surfaces on the low-field-side (LFS), extending from the outer midplane down to the divertor target plate. The value of D was set to 0.25 m^{2}s^{-1} in the outer divertor leg below the main plasma X-

point, to allow for a plausible rate of particle diffusion into the private flux region. In Section 5.4, we examine the sensitivity of our model results to variation in the v_{conv} and D in the outer divertor leg. On the high-field-side (HFS), v_{conv} was set to zero throughout the SOL, as no density shoulder or convective radial flux is observed experimentally on the HFS [129].

A base value for the power exhaust crossing the LCFS into the SOL, P_{SOL}, was taken as 105 MW for this ARC model. This value was decided early on in this study before the 93 MW value given in Ref [105] and Chapter 4 was known, by estimating it simply as equal to 1/5th of fusion power (i.e. the α-power) and assuming core radiation power approximately equals the heating power. Given this slightly exceeds the 93 MW specified in Ref [105] (which assumed 35% core radiation fraction), taking 105 MW as the target for the divertor handling is an increase in the divertor burden, which allows for some head-room for the ARC design in case the core radiation is lower than assumed in Ref [105]. Ion/electron energy diffusion coefficients of $\chi_{i,e} = 0.1$ m^{2}s^{-1} are set throughout the domain (a typical value observed experimentally in H-mode plasmas [131]), with exception of the LCFS region in which a transport barrier (i.e. reduced $\chi_{i,e}$ value) is applied. Note that previous studies have found spatially constant $\chi_{i,e}$ was sufficient to match experimentally observed midplane temperature profiles in C-Mod L-mode plasmas [133], but a transport barrier is required here to achieve the narrow $\lambda_{q||}$ anticipated and to reproduce the shape of observed H/I-mode SOL temperature profiles. Based on the Eich empirical scaling law [21] and a recent extension of the heat flux width database to include I-mode plasmas [181], we anticipate that the heat flux width in ARC at its operational design point will be $\lambda_{q||} \sim 0.4$ mm. To attempt to create this value, an energy transport barrier is created ~1 mm on either side of the separatrix on the low-field side (LFS) of the confined plasma by decreasing $\chi_{i,e}$ to 0.01 m^{2}s^{-1} (note though that as LCFS grid resolution changes across various SXD/XPTD grids implemented, this value requires adjusting - see Sections 5.3 and 5.4). The parallel heat flux profile $q_{||}$ (i.e. the sum of electron and ion heat flux densities) across the entrance to the divertor leg is measured to verify the e-folding width of 0.4 mm when mapped to the outer midplane (see measurement location as the dashed line in Figure 5.1 and resultant profile in Figure 5.3). On the high-field side (HFS), the transport barrier was enhanced by decreasing $\chi_{i,e}$ further to 0.005 m^{2}s^{-1}. This creates an approximate 10:90 split of exhaust power across the separatrix to the HFS:LFS, consistent with observations from near-double-null I-mode plasmas on C-Mod [134] as well as MAST double-null operation [135]. This energy transport

barrier in $\chi_{i,e}$ is only applied at the interface between open and closed magnetic flux surfaces in the main-chamber region, and not in the divertor legs.

A reproduction of plasma profiles in ARC's core and pedestal regions is not attempted for this study of the SOL and divertor, and dashed line sections of the midplane profiles (Figure 5.3) inside the separatrix do not represent the core profiles postulated for ARC in [17]. These instead serve to establish the required boundary conditions at the separatrix mentioned for the SOL profiles above. Density at the core plasma boundary is set to obtain a fixed density at the separatrix of nominally 1x10^{20} m^{-3}. Equal electron and ion powers entering the domain are also specified at the core plasma boundary to obtain the total desired power crossing the LCFS (where total power in these half-domain simulations is taken as half of the total exhaust power entering the SOL in the full ARC domain, P_{SOL}). Neumann boundary conditions are applied to the edge/private flux region (PFR) boundaries in the form of radial linear extrapolations to the guard cells for both plasma density and for electron/ion temperature. It is worth noting that the edge boundary in this case represents a region in the far SOL, rather than a first wall boundary, since the simulation grid did not reach the reactor first wall (see Figure 5.1). Target plates employ a plasma sheath boundary condition. Neutral recycling was set to 100% at both target and edge/private-flux-region (PFR) boundaries (for particle balance and wall saturation in steady-state operation [136]), with neutrals being included in the UEDGE diffusive model [114]. To simulate just a lower-half domain for ARC, we assume up-down symmetry in the divertor response, and as such a symmetry condition was implemented at the poloidal midplane boundaries. This required performing the UEDGE simulations without particle drifts; drift effects introduce up-down asymmetries that would be incompatible with such a symmetry condition. Using the described model, UEDGE was run to produce converged steady-state solutions for all results shown in this thesis.

5.2 ARC Super-X Divertor

5.2.1 Without impurity seeding

This physics model is initially applied to the SXD geometry for the ARC 'base-case', i.e., a DT plasma with 105 MW of exhaust power crossing the LCFS into the SOL and with no impurity seeding to enhance radiation in the divertor. The SXD grid format included 54x19 poloidal/radial grid cells (with an additional guard cell either side of the domain

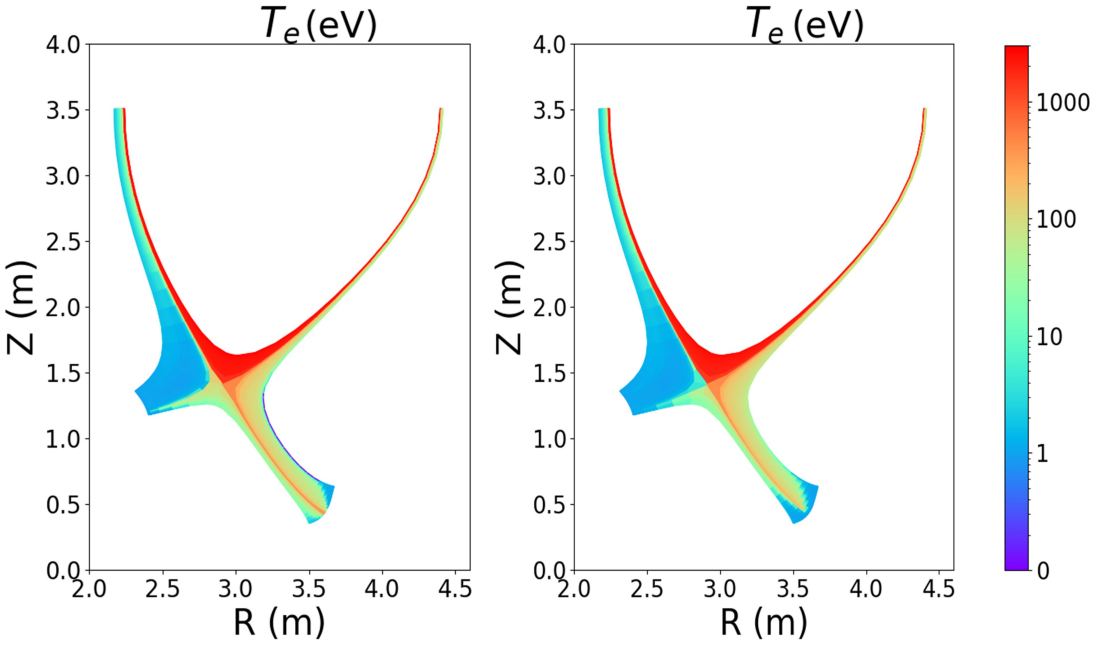

Figure 5.4: 2D T_e plots for ARC SXD steady-state solutions, for P_{SOL} = 105 MW both without impurity seeding (left) and with 0.5% neon impurity fraction (right).

in each dimension). Radial grid cells were clustered around the separatrix to attempt to maximise resolution in this region - with a radial resolution obtained of ∼0.75 mm at the LCFS. This is lower resolution than would be desired for this problem - with an Eich $\lambda_{q||}$ of 0.4mm, this implies our simulations will be radially under-resolved with respect to the heat flux. Indeed, the parallel power decay width $\lambda_{q||}$ obtainable from the $\chi_{e,i}$ transport barrier proved to be resolution limited to $\sim$ 0.55 mm, marginally greater than the 0.4 mm value desired. Attempts to increase the resolution by reducing cell separation or increasing the number of cells were unsuccessful due to failure of the UEDGE grid generator to construct these grids. The reason for this gird generator failure is unclear, and this remains an issue to be resolved. With no alternatives available, this study was forced to continue with the resolution specified, and accept the uncertainty in the results that this brings.

A 2D T_e plot is given in Figure 5.4 for the converged UEDGE solution for the ARC base-case. The parallel power decay width of $\sim$ 0.55 mm resulted in a narrow high temperature, high power flux intensity region in the near SOL outside the separatrix, that extends down to the divertor plate. The peak $q_{||}$ at the X-point entering the divertor region was measured to be $\sim$ 10 GWm^{-2} (see Figure 5.3). Peak electron temperature at the outer target plate for this base case are in excess of 300 eV (whilst the inner target remains detached), far above

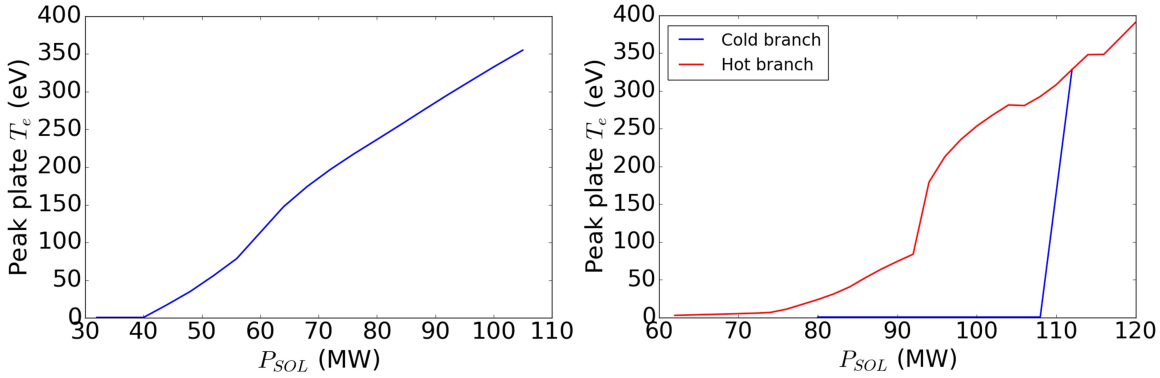

Figure 5.5: SXD power scan results showing peak outer plate T_e (eV) against exhaust power P_{SOL} (MW) for 0% neon fraction (left) and 0.5% neon fraction (right).

what target materials could be expected to survive.

In practice, core radiation may result in the exhaust power entering the SOL from the core being less than the 105 MW assumed in this case (i.e. 93 MW for the ARC operational design point value). Keeping all other parameters/conditions fixed, a power scan was performed by steadily reducing P_{SOL}, to determine the power window for which stable detachment could be obtained. The results are shown in Figure 5.5(left). Stationary detached solutions (defining detachment where plate T_e <1 eV) are obtained for the power window of 32-40 MW. Below 32 MW, the solution develops an X-point MARFE - the detachment front moves up the entire divertor leg and into the core plasma.

5.2.2 With 0.5% Neon impurity seeding

To improve the power handling performance of the ARC SXD setup, a 0.5% neon (Ne) impurity was introduced in the "fixed fraction" model - where impurity concentration is set at a percentage of the plasma electron density throughout the domain - to increase radiation energy losses of the plasma in the SOL. Ne was chosen as the impurity species for investigation as it a) is a strong SOL radiator but also a low Z species, giving it relatively minimal impact for core radiation or fuel dilution b) recycles 100% on plasma-facing material surfaces and c) does not react to produce ammonia in the reactor, like nitrogen. A power scan was repeated, the results of which are shown in Figure 5.5(right). The results produced a bifurcation in solutions with two branches: a hot and a cold branch. The cold branch is accessible by gradually ramping up input power (P_{SOL}) and neon impurity fraction in tandem from an initially unseeded detached solution (i.e. $P_{SOL} < 40MW$ in Figure 5.5),

maintaining detachment until 0.5% Ne fraction is obtained. This branch shows detachment can be obtained at much higher P_{SOL} with the presence of the Ne impurity, now with a P_{SOL} window of 80-108 MW. Below 80 MW, the cold branch solutions develop an X-point MARFE. Increasing P_{SOL} above 108 MW results in transition to the hot branch, after which a reduction in P_{SOL} does not result in a transition back to a detached solution, but plate temperatures remain hot until P_{SOL} <62 MW where the hot branch solutions MARFE. Such bifurcations have previously been observed in UEDGE solutions [114], and have also been studied analytically [137].

A plot of T_e for a detached case (with $P_{SOL} = 105$ MW) is shown in the right-hand plot in Figure 5.4. The same narrow, high temperature region is observed in the temperature profile, but now with distinct regions dropping to T_e <1 eV for both the inner and outer target plates. Figure 5.6 shows the same plot with annotation of the peak power flux densities to different boundaries, from combined plasma and radiation power loadings. The peak power flux density measured was 6.4 MW m^{-2} to the outer target plate, lower than the 10 MW m^{-2} accepted as the maximum power flux that can be accommodated by a solid wall. This is despite the presence of a high-intensity Ne radiation front directly above the target plate

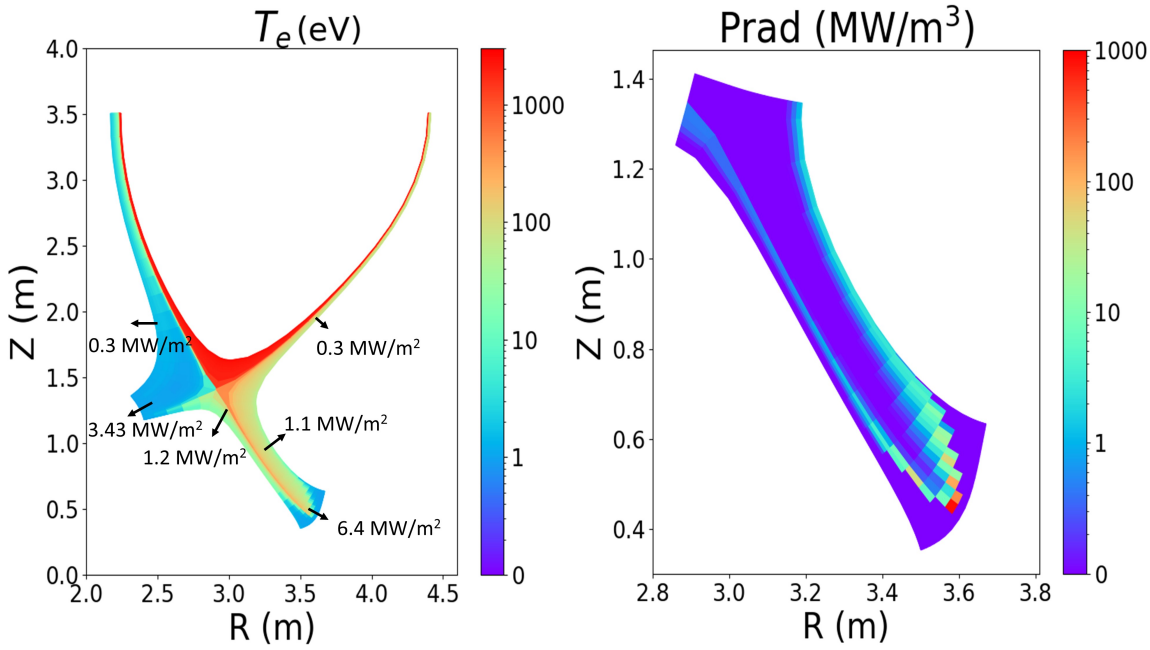

Figure 5.6: 2D plots for $P_{SOL} = 105$ MW, 0.5% Ne impurity detached SXD solution of (left) T_e with annotated peak power flux densities to the boundaries, for combined plasma and radiation power loadings, and (right) neon impurity radiation emissivity, with a peak value of 855 MW m^{-3}.

(Figure 5.6(right)), with a peak emissivity of 855 MW m^{-3}.

The large detachment power threshold hysteresis effect between the Ne seeded cold/hot branches could be due in part to the fixed fraction impurity model used here, coupling the impurity radiation power directly to the plasma density and the attached/detached conditions at the target plate. Investigating if this effect persists (or alternatively increases/decreases in magnitude) when modelling impurities with a full fluid model of their own would be an interesting further study and should be pursued.

5.2.3 Convergence testing

Convergence testing for the simulation grids should be performed in order to have confidence in the results obtained. The SXD grid was used for this testing since the method of construction for the XPTD grids made them not suitable for this task (specifically the grid generator method required the two X-point separatrices to be consistently separated by two radial grid cells, and as such changes to the grid structure would change the underlying magnetic geometry of the simulation). This convergence testing was performed by attempting to double poloidal/radial grid resolution for the base (no impurity) $P_{SOL} = 105$ MW ARC scenario, and monitor any changes to the numerical results.

Doubling the number of poloidal grid cells (providing 108x19 poloidal/radial cells) had little impact on the simulation results. Plasma variables values changed by $< 3\%$, and repeating a power scan as in Figure 5.5 showed the detachment threshold to be unchanged at 40MW (within the resolution of the scan performed, ± 2 MW). These results increased confidence that the simulations were well resolved poloidally.

As already alluded to earlier in Section 5.2, significant difficulties were encountered in generating grid with higher radial resolution. Doubling the number of radial grid cells (providing 54x38 poloidal/radial cells) caused the UEDGE grid generator to fail in grid construction. In order for the grid generator to successfully produce grids with these dimensions, the cell clustering around the separatrix had to be reduced. Grids with 54x38 cells could then be produced, but the resulting grids had approximately the same physical resolution at the separatrix of $\sim$0.75 mm. Given this is the region of greatest interest with regards to radial resolution, and the resolution in this region has not changed (with the far SOL being the beneficiary of the extra cells), this makes an unsatisfactory convergence test. Therefore the grid generation issues prevented a meaningful convergence test from being performed for the

radial resolution, and this remains an area of significant uncertainty associated with these results.

5.3 ARC X-Point Target Divertor

The same physics model described in Section 5.2 was applied to the XPTD geometry. To accommodate the extra length of simulation domain, the number of poloidal grid cells was increased to 86 (i.e. creating grids of 86x20 poloidal/radial cells). Several XPTD grids were implemented in UEDGE with different primary and divertor X-point radial separations, ranging from 1.6 mm to 0.50 mm (mapped to outer midplane). A different grid generator method is used for construction of the XPTD grids than the SXD, and this generator was able to successfully create grids with LCFS resolutions down to ∼0.25mm (below which this generator also started to fail). The XPTD grids consistently have two radial grid cells separating the two X-point separatricies, and hence reducing the radial X-point separations corresponds to increasing the resolution around the LCFS. Anticipating a decrease in $\lambda_{q||}$ as the LCFS becomes better resolved (since the previous SXD model was resolution limited to $\lambda_{q||}$∼0.55mm), the depth of the transport barrier was adjusted on the LFS to $\chi_{i,e} = 0.02$ m^2s^{-1}.

Scans of P_{SOL} are repeated for the various XPTD grids without any Ne impurity seeding, and results are plotted alongside the SXD power scan results for comparison (Figure 5.7). Power scans are performed for both decreasing P_{SOL} from the attached 105 MW base scenario (a "downswing" power scan) and for increasing P_{SOL} from a low-power, detached state (an "upswing" scan). Peak $q_{||}$ at the primary X-point increases from ∼9 to 15 GWm^{-2} across XPTD grids with narrowing X-point spacing and corresponding increasing resolution at the LCFS. A ∼30-40% increase in $\lambda_{q||}$ is observed over a power scan for the fixed transport model at the transition to the detached divertor regime across all grids. Such $\lambda_{q||}$ broadening under detached divertor conditions has been observed in experimental studies [138].

The results show slight gains in detachment threshold for the XPTD geometries over the SXD, however values of $q_{||}$ and $\lambda_{q||}$ were not kept fixed as described further below. The 1.6mm X-point separation grid increases the detachment threshold for the downswing power scan (solid line) from $P_{SOL} = 40$ to 46 MW, and then for smaller X-point separations in the range of 0.84-0.50mm, detachment threshold cluster in the range of $P_{SOL} = 52$-56

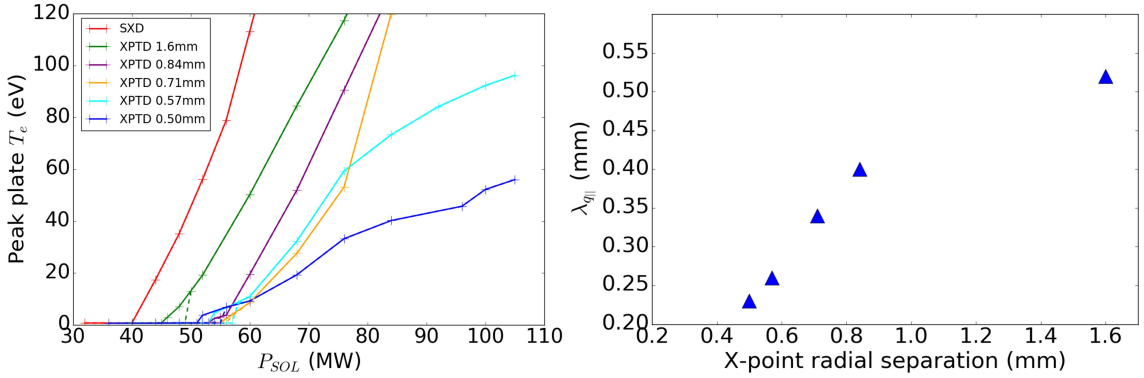

Figure 5.7: (Left) Peak outer target T_e vs exhaust power P_{SOL}, for SXD and XPTD grids with radial X-point separations ranging from 1.6 mm to 0.50 mm. "Downswing" power scan solutions are shown with solid line and "upswing" scans by the dashed lines. (Right) Measured $\lambda_{q||}$ against X-point radial separation for XPTD cases with fixed $\chi_{i,e}$ transport model. The SXD case had $\lambda_{q||} \sim 0.55$ mm.

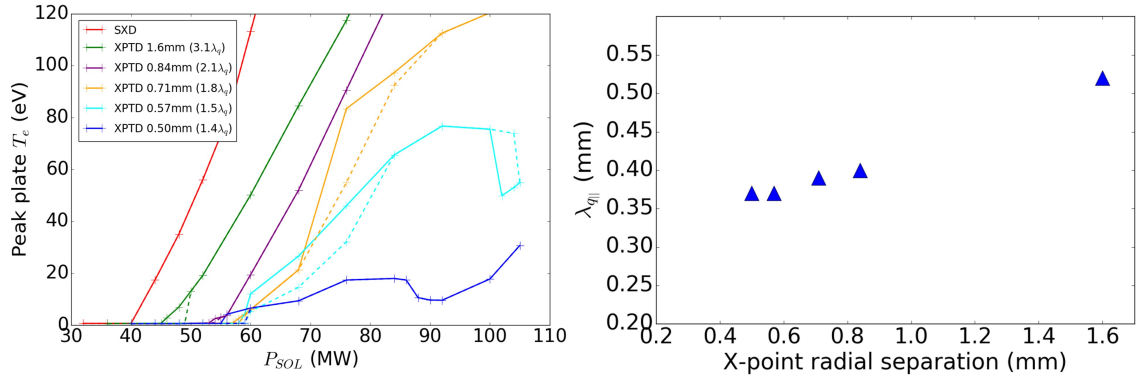

Figure 5.8: (Left) Peak outer target T_e vs exhaust power P_{SOL} for repeated downswing (solid line) and upswing (dashed line) power scans for SXD and XPTD grids with adjusted $\chi_{i,e}$ transport model to maintain $\lambda_{q||}$~0.4mm. (Right) New measured $\lambda_{q||}$ across XPDT grids with adjusted $\chi_{i,e}$ transport model.

MW. The upswing power scans (dashed lines) show similar results, but with detachment threshold 2-4MW greater than for the downswing scans. Analysing $\lambda_{q||}$ over XPTD grids shows that as the X-point radial separation gets smaller and resolution around the LCFS increases, the measured value of $\lambda_{q||}$ is found to be decreasing (Figure 5.8). This confirms that the simulation grids with the SXD and the wider XPTD spacings were under-resolved and resolution-limited for the current transport model. For the grids with the narrowest separations of 0.71, 0.57 and 0.50 mm, $\lambda_{q||}$ drops below the 0.4 mm Eich-scaling width anticipated for ARC, dropping as low as 0.23 mm.

In an attempt to hold $\lambda_{q||}$ fixed at 0.4 mm, the downswing and upswing power scans

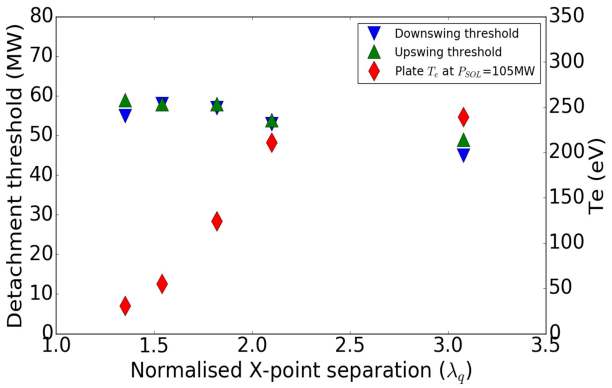

Figure 5.9: Plots of downswing/upsing power scan detachment thresholds (MW) and peak plate T_e (eV) at P_{SOL} = 105 MW against XPTD X-point separation (normalised to $\lambda_{q||}$).

were repeated with the $\chi_{i,e}$ transport barrier depth adjusted for the 0.71, 0.57 and 0.50 mm separation XPTD grids to 0.035 , 0.065 and 0.085 m^2s^{-1} respectively on the LFS (as well as 0.007, 0.007 and 0.008 m^2s^{-1} respectively on the HFS to maintain the 10:90 HFS:LFS power split). This is a less than ideal solution for comparison of simulations - in reality quantities such as $\chi_{i,e}$ defined in real-space should not change with grid resolution - but in absence of solutions to the radial grid resolution issues this was the only available route to proceed. Power scan results are plotted in Figure 5.8 alongside the new measured $\lambda_{q||}$ values. Detachment thresholds and the peak plate temperatures at the P_{SOL} base value of 105 MW are plotted for all grids in Figure 5.9. Now maintaining near-constant $\lambda_{q||}$ across 0.84-0.50mm separation grids, the normalised X-point separation in $\lambda_{q||}$ steadily decreases across XPTD grids, spanning a range of 3.1 - 1.4 $\lambda_{q||}$.

For the two grids with the smallest X-point separations of 0.57 and 0.50 mm, an unexpected behavior is observed: as P_{SOL} is increased, sharp decreases in plate temperature occur at certain P_{SOL} values. These appear to represent transitions across different branches of solutions, akin to the "hot" and "cold" branch solutions observed for the SXD Ne impurity seeded cases shown in Section 5.2, but over much smaller power windows. (It is noteworthy that for these impurity-free solutions, large detachment power threshold hysteresis loops, as seen in Section 5.2, are not present here.) One possible explanation is that as the target X-point is becoming more engaged in attenuating and splitting the power flux (i.e. spacing less than $2\lambda_{q||}$) non-linearities associated with the power loss channels of hydrogenic radiation and plasma-neutral interactions play a more important role. Further study of this behaviour was beyond the scope of the present investigation and should be pursued.

Apart from an initial gain from decreasing X-point spacing from 1.6 to 0.84mm, detachment threshold remains fairly constant in the ranges of 53-58 MW and 54-59 MW for downswing and upswing power scans respectively for all grids with X-point separations smaller than 0.84mm. The gain in threshold over the SXD (detaching at $P_{SOL} = 40$ MW) is significantly less than previously observed in modelling for the geometries in ADX, which found a factor of ∼2 gain in threshold for the XPTD over the SXD [112]. However, the ADX study employed an X-point spacing of 0.7 $\lambda_{q||}$, which we have not yet explored. Indeed, reducing X-point separation does result in a steadily decreasing peak target plate temperature at the base case $P_{SOL} = 105$ MW, decreasing by nearly a factor of 10 by the 0.50 mm XPTD grid from 240 to 31 eV (Figure 5.9). Why this does not result in higher detachment thresholds is not yet understood - the gradient of the plate temperature over a power scan is much shallower for the smaller X-point separations, even accounting for the unusual plate T_e behaviour over these power scans. Additional study is required to identify root causes. Extrapolating the trend in target plate T_e suggests that detachment at the $P_{SOL} = 105$ MW base value may potentially be achieved with X-point spacing of ∼1 $\lambda_{q||}$ or less. It is not currently possible to generate grids with spacing lower than 0.50 mm at this time, and this remains an area for further study.

The radial $q_{||}$ profile is analysed for each SXD and XPTD grid in Figure 5.10, for $q_{||}$ above the target plate for the SXD and above the divertor X-point for the XPTD cases. Relating to $\lambda_{q||}$, all cases have radial X-point separations greater than 1 $\lambda_{q||}$, and so the majority of the exhaust power peak is directed to the lower target in the outer XPTD leg (which is subsequently referred to as the "primary target"). For separations of several $\lambda_{q||}$, very little exhaust power is split from the main heat flux channel towards the upper target in the X-point region, and hence the divertor behaves in a similar manner to the SXD setup. When X-point separations are smaller, a larger fraction of the total exhaust power is split from the main heat flux channel, and the peak $q_{||}$ profile significantly reduces. This is at least consistent with the drop in target plate temperature for narrowing X-point spacing. To reduce the peak $q_{||}$ further, normalised X-point separations of ∼1 $\lambda_{q||}$ or lower may be required to properly engage the divertor X-point for enhanced power handling performance. This provides further motivation to study XPTD grids with 1 $\lambda_{q||}$ separations or lower. The poloidal power flux, q_{pol}, is calculated for each case and shown in Figure 5.11. These data indicate that by reducing the X-point spacing to 1.4 $\lambda_{q||}$ the peak plasma power loading on

the primary target is reduced from a maximum of ∼50 MWm^{-2} to ∼25 MWm^{-2}. This result is encouraging; with target plate tilting (not employed in this design) peak power loading may be reduced to less than ∼10 MWm^{-2}, which is remarkable considering the peak parallel heat flux entering the divertor of ∼10 GW m^{-2} and the lack of impurity radiation in these divertor scenarios.

5.4 Model sensitivity studies for the XPTD

A number of assumptions are made in the modelling, some of which are not experimentally validated yet - in particular assumptions in relation to the upstream separatrix density and the radial transport along the divertor leg. In this section, various model parameters relating to these assumptions are varied, to test the robustness and sensitivity of our ARC model solutions.

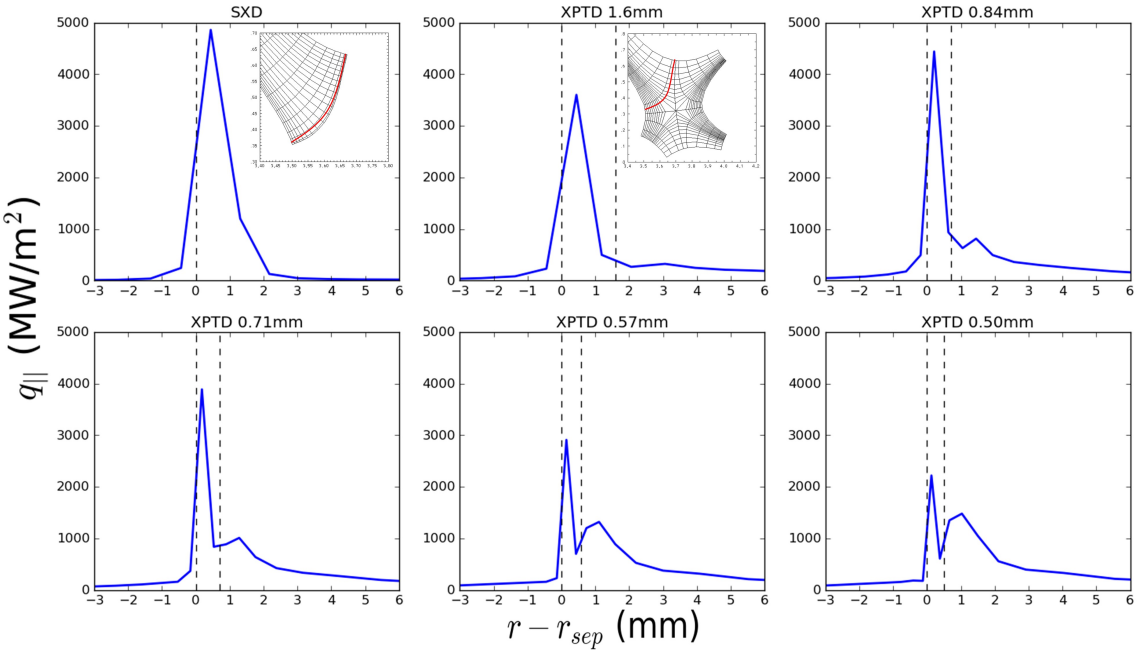

Figure 5.10: Plots of $q_{||}$ measured above the divertor target for the SXD and above the divertor X-point for the XPTD grids, mapped to the midplane. Separatricies locations shown with dashed lines. Inset plots in frames 1 and 2 show location of measured $q_{||}$ for the SXD and XPTD grids respectively.

5.4.1 Upstream density

The ARC design point reference discharge [17] used for this study, with separatrix density of ~1x10^{20} m^{-3}, has Greenwald density fraction of 0.67. Thus it may be possible to operate ARC at a higher plasma density, further increasing the power range over which an impurity-free detached divertor regime may be obtained. In order to examine this, the upstream separatrix density was increased from the reference point value of 1.0x10^{20} m^{-3} to 1.17x10^{20} m^{-3} and 1.50x10^{20} m^{-3}, by adjusting the core density boundary condition. This was performed for the 0.57 mm separation XPTD grid with the $\chi_{i,e}$ transport barrier model described in Section 5.1 (transport barrier depth of $\chi_{i,e}$ = 0.02 m^{2}s^{-1} and 0.005 m^{2}s^{-1} for LFS and HFS respectively), having a normalized X-point spacing of 2 $\lambda_{q||}$. For the 1.5x10^{20} m^{-3} case studies, re-tuning of the v_{conv} profile was required to retain a similar midplane density profile properties as for the lower density cases (i.e. decay length of $\lambda_n \sim$ 5.5 mm, flattened density shoulder in far SOL). The new v_{conv} and midplane n profiles are shown in Figure 5.12.

Downswing and upswing powerscans were repeated for the new cases with the 0.57mm X-point separation grid, and results for these are plotted alongside the ARC base scenario

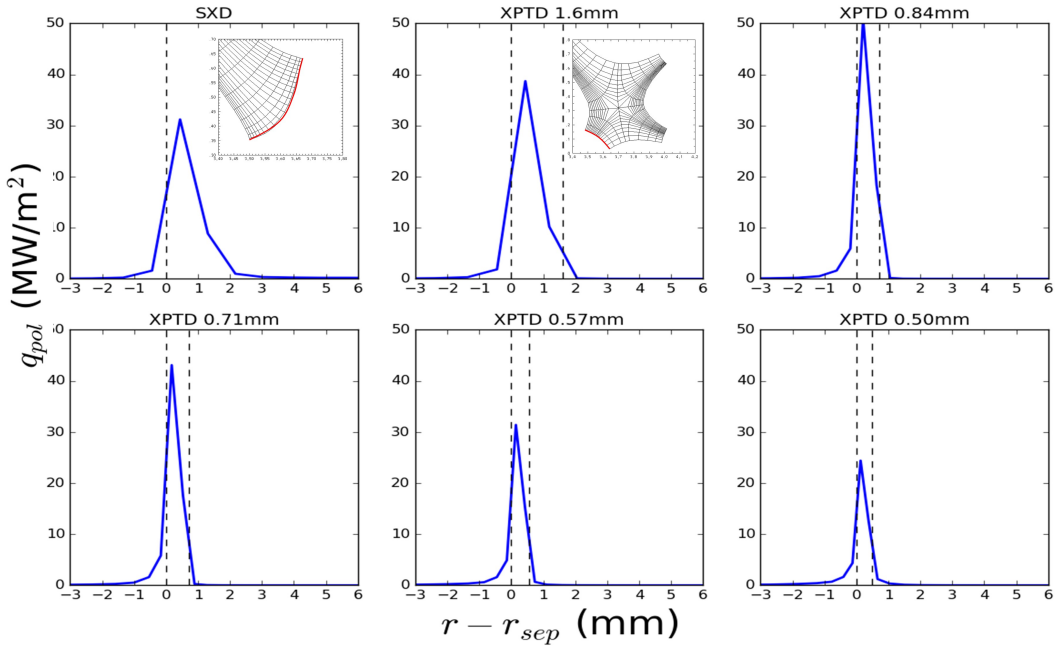

Figure 5.11: Plots of q_{pol} measured above the divertor target plate for the SXD and XPTD grids, mapped to the midplane. Separatricies locations shown with dashed lines. Inset plots in frames 1 and 2 show location of measured q_{pol} for the SXD and XPTD grids respectively.

(1x10^{20} m^{-3}) in Figure 5.13. A significant increase in detachment threshold is observed in both power scan directions, increasing from 53 to 108 MW for the downswing power scan, and from 57 to 128 MW for the upswing power scan. The difference between downswing/upswing detachment thresholds has substantially widened under these higher density conditions. At n_{sep} = 1.50x10^{20} m^{-3}, the solutions obtained fully handles the ARC exhaust power in both power scan directions, without any use of impurity seeding.

Converged solutions below P_{SOL} = 96 MW could not be obtained for this ARC model with raised upstream density. However, in the range of P_{SOL} = 56-96 MW, despite solutions failing to converge the detachment front remains near-stationary within the divertor leg volume for a given P_{SOL} value, with X-point MARFE onset only occuring when P_{SOL} < 56 MW. In these cases there are small scale oscillations in the plasma parameters (though qualitatively the divertor scenario does not change). The dashed line on Figure 5.13 marks these unconverged solutions. This makes the full extent of detachment window in this case poorly defined (whilst detachment threshold remains well defined still), but likely to still contain the 93 MW ARC design point power exhaust within this window. Peak powerfluxes to the boundaries for the detached P_{SOL} = 105 MW solution are calculated and shown in Figure 5.14, showing acceptable power flux densities to all boundaries (with the inner divertor target being on the ∼10 MWm^{-2} limit, but could be reduced by introducing target plate tilting).

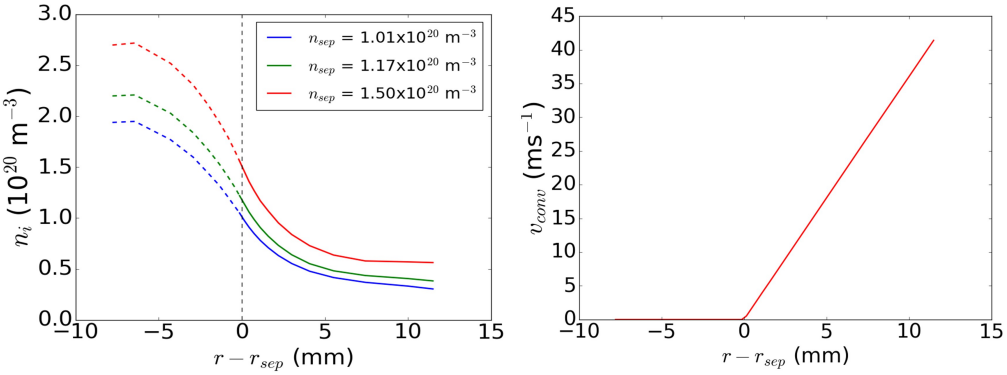

Figure 5.12: Plots of midplane density profiles for the three n_{sep} cases investigated (left) and the new v_{conv} profile for the 1.50x10^{20} m^{-3} case (right).

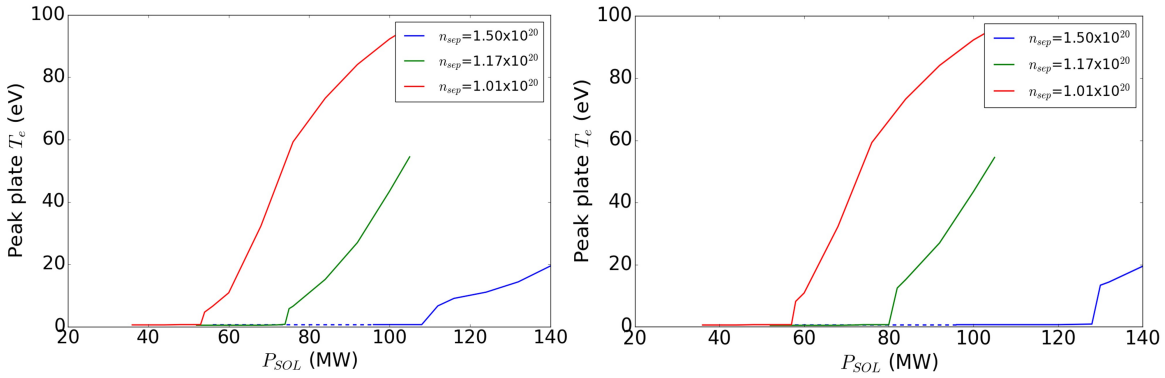

Figure 5.13: Plots of downswing (left) and upswing (right) powerscan results for peak plate temperature (T_e) for the ARC base upstream separatrix density 1.01x10^{20} m^{-3} and the increased 1.17x10^{20} m^{-3} and 1.50x10^{20} m^{-3} cases for the 0.57mm X-point separation grid, corresponding to a normalized X-point separation of 2 $\lambda_{q||}$. The dashed blue line indicates unconverged solutions with the detachment window for the n_{sep} = 1.50x10^{20} m^{-3} case.

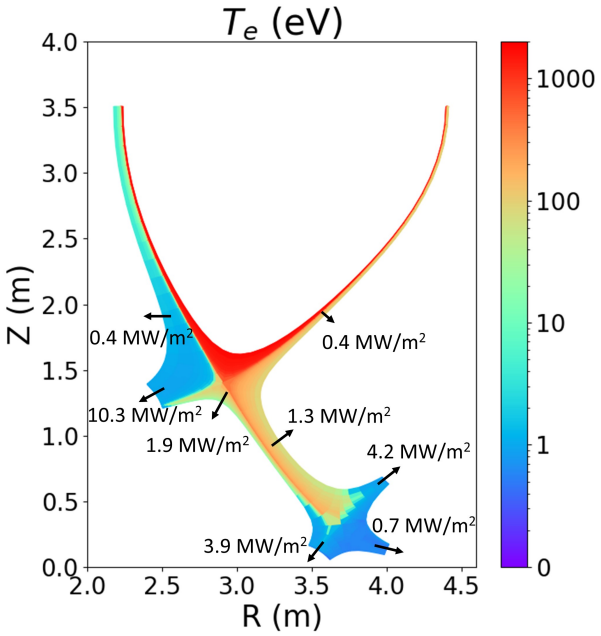

Figure 5.14: Peak power flux densities to domain boundaries for the detached P_{SOL} = 105 MW, n_{sep} = 1.50x10^{20} m^{-3} solution.

5.4.2 Leg radial transport coefficients D and v_{conv}

The magnitude of the radial transport in the long outer divertor leg is one assumption in our model without experimental validation, in particular, lacking experimental data on tightly-baffled, long-legged divertor behaviour. To assess the effect of relaxing this assumption, the magnitude of the transport coefficients D and v_{conv} in the divertor leg volume are varied

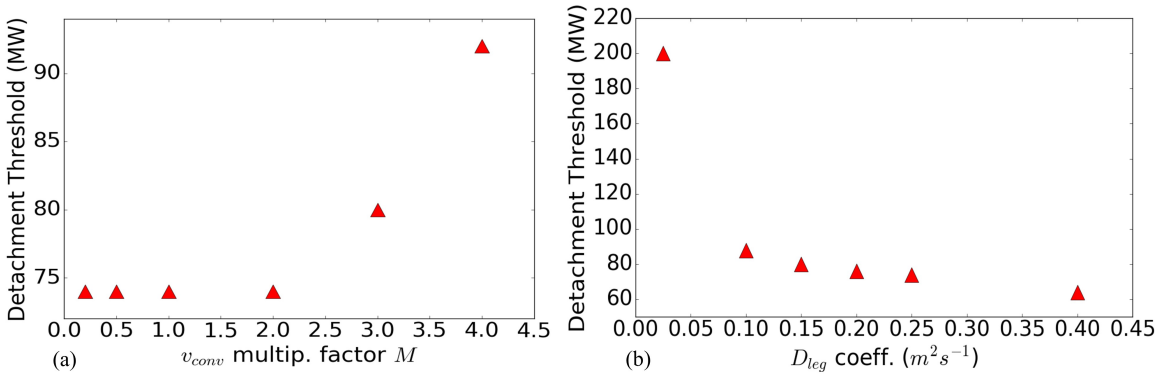

Figure 5.15: Variation in downswing power scan detachment threshold for variation in outer divertor leg values of (a) v_{conv} multiplier factor M and (b) diffusive transport coefficient D.

to assess sensitivity to radial transport for our solutions. As only the transport coefficients in the outer leg were varied and the main chamber transport remained the same, there was no notable change in upstream conditions (midplane profiles, $\lambda_{q||}$) across these sensitivity studies (with the exception of where detachment is enabled at P_{SOL}=150 MW), enabling direct comparisons with the base case results for this XPTD grid.

The magnitude of the convection velocity was changed by multiplying the base-case v_{conv} profile given in Figure 5.2 by a multiplication factor M, such that ${v_{conv}}^{new} = M{v_{conv}}^{orig}$, in the outer divertor leg volume only. A "downswing" powerscan was performed again with the 0.57 mm separation XPTD grid, $n_{sep} = 1.17\text{x}10^{20}$ m^{-3} case from Section 5.4.1 for each value of M studied, with all other factors held constant, to find the new detachment threshold. Results are plotted in Figure 5.15(a). For multiplication factors between 0.2 and 2 the detachment threshold is unchanged from the base-case value of 74 MW, and for $M > 2$ the threshold increases. From this we can conclude that our results are robust to variation in v_{conv} magnitude over a reasonable range, with no deterioration in performance and getting only better performance if significantly larger convective transport than assumed is observed.

To interpret these results, particle and plasma power flows to the boundaries are calculated in the divertor leg for each value of M. Annotated plots of these with the divertor leg mesh are given for $M = 1$, 2 and 4 in Figure 5.16. An estimate of power losses to hydrogenic radiation is shown also. These show that, as M is increased from $M = 1$ to 2, despite an increase in the particle flux to the outer SOL the plasma power to the primary target remains similar. Only for $M = 4$ does the power to the primary target drop significantly, and power flow to the outer SOL boundary dominates. It is notable that this $M = 4$ case is the only

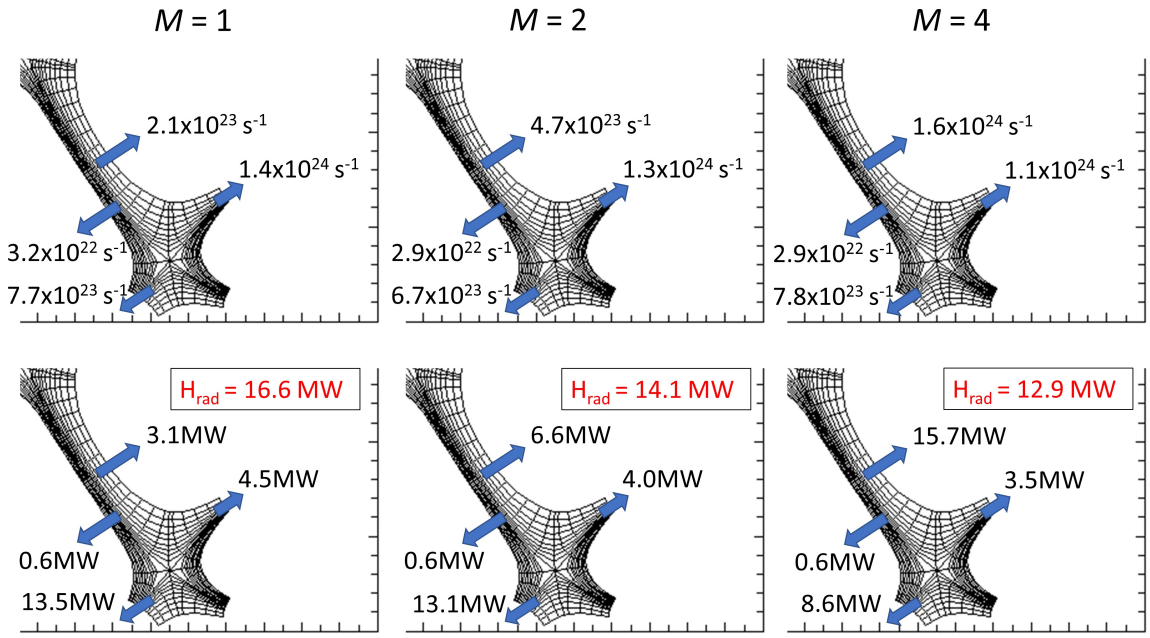

Figure 5.16: Annotated plots of particle (upper) and plasma power flows (lower) to the divertor leg mesh boundaries for v_{conv} multiplier factors of $M = 1$, 2 and 4. An estimate of power losses to hydrogenic radiation in the divertor volume is given.

one of the three where the particle flux to the outer wall is of the same order of magnitude as the parallel flux to the plates, and exceeding the flux to the primary target. In this case we can argue the exhaust power is now directed primarily towards the sidewall, and detachment physics is now more dependent on interaction with the side wall than with the target plate.

To characterise this change, a plot of the calculated ratio of perpendicular/parallel plasma power in the divertor leg is shown in Figure 5.17(a), and Figure 5.17(b) shows instead the ratio of side wall/primary target particle flux. Here perpendicular refers to the sum of fluxes arriving along the outer side wall and PFR boundaries, while parallel refers to fluxes arriving at the two target plates. (Note that the outer side wall particle fluxes are not connected to the primary target particle flux via recycling). In Figure 5.17(b) we see a change in detachment threshold response when the ratio of particle fluxes is greater than 1 (whereas no obvious physically-motivated regime-change value can be identified for the power flux ratio in Figure 5.17(a)). A transition between two regimes can be characterised as such: when particle flux to the primary target plate exceeds that to the side wall, the power exhaust is dominated by interaction with the target plate and detachment threshold is insensitive to variation in the radial convection velocity within a certain magnitude. When the ratio is greater than 1,

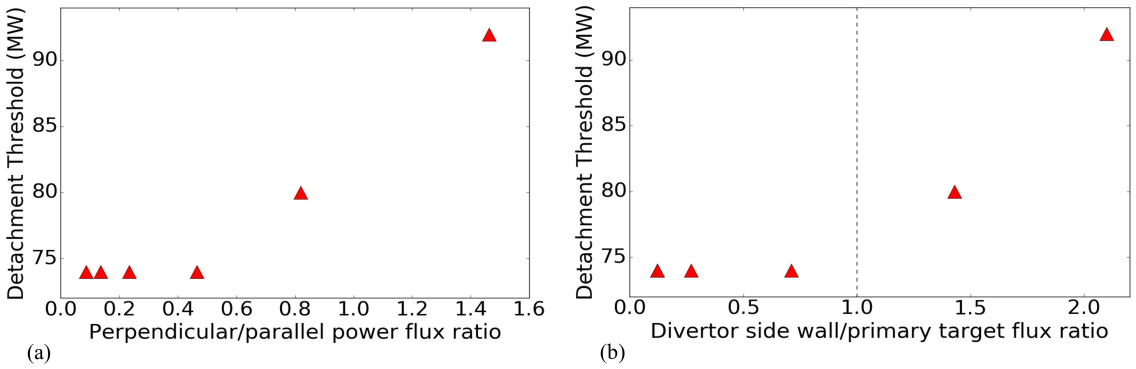

Figure 5.17: Plots of the calculated ratio of (a) perpendicular/parallel plasma power in the divertor leg, and (b) of side wall/primary target particle flux obtained during a scan of v_{conv} multiplier factors, M.

power is primarily transferred to the side wall and detachment physics becomes dependent on the plasma side wall interactions. For the standard base-case ARC operation, ARC is well within the first regime, with a particle flux ratio of ∼0.5.

The magnitude of the D coefficient in the outer leg (D_{leg}) was varied from the base value of 0.25 m^2s^{-1} across a range of 0.025-0.4 m^2s^{-1}, with the impact on the downswing detachment threshold shown in Figure 5.15(b). These show a decrease in detachment threshold as D_{leg} is increased. Except for the data point at $D_{leg} = 0.025$ m^2s^{-1}, the changes are relatively small (∼30%), scanning the a wide range of $D_{leg} = 0.1$-0.4 m^2s^{-1}, so our solutions are seen to be to be fairly robust to variation in D_{leg} as well.

The observation that the detachment threshold decreases with increasing D_{leg} goes against intuitive expectations. One might expect that a smaller D_{leg}, and hence more concentrated plasma flux, would result in a more concentrated power loading on the divertor and deteriorating divertor power handling performance, not improving. To analyse this, plasma particle/power flows to the divertor leg boundaries are examined again (Figure 5.18). Density profiles are narrower and more peaked with smaller D_{leg}, resulting in lower particle flux to the side walls and higher particle flux to the diverter targets. However, the plasma power to the primary target has decreased, a result which is again counter-intuitive.

To explain this, conditions at the target plate bewteen the two cases were examined (Figure 5.19). Decreasing D_{leg} causes an increase in the plasma density at the strike point by factor ∼2, which in part explains the decrease in temperature. With high particle flux to this plate and a recycling coefficient of 1.0, the greater flux to the plate from reducing

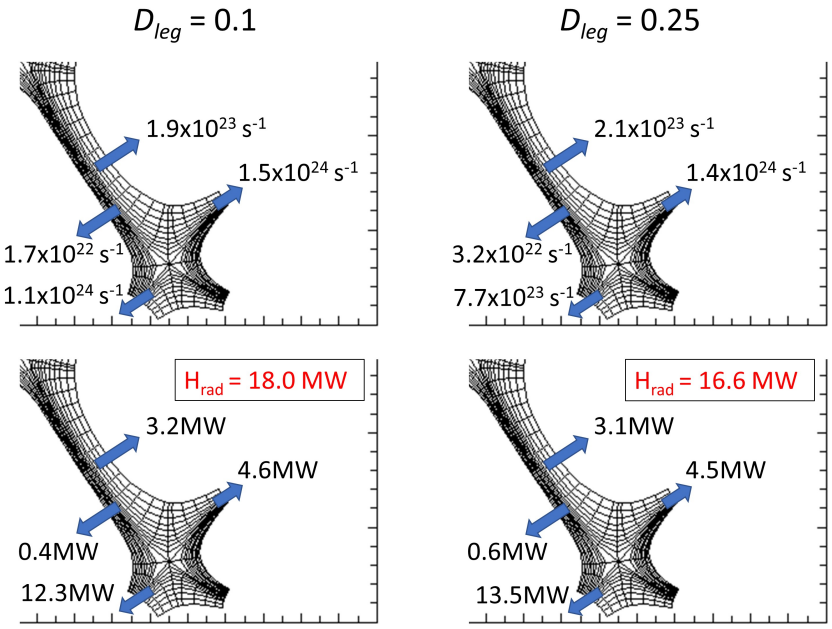

Figure 5.18: Annotated plots of particle (upper) and plasma power flows (lower) to the divertor leg mesh boundaries for D_{leg} values of 0.1 and 0.25 m^2s^{-1}. An estimate of power losses to hydrogenic radiation in the divertor volume is given.

D_{leg} means greater number of recycled neutrals at the target. This is seen in the simulation as higher neutral density at the target plate, resulting in a factor of ∼2.5 increase in peak neutral density as D_{leg} is decreased from 0.25 to 0.1 m^2s^{-1}. The increased neutral density for the 0.1 m^2s^{-1} case is not seen to extend further into the domain, indicating ionisation of these neutrals and enhanced ionisation energy losses. As a result, the peak hydrogenic radiation power flux to the wall increases by factor of ∼1.5. The combination of both the increase in density and increase in hydrogenic radiation causes the peak target temperature to drop by factor of ∼2.8. This result highlights that for regimes in which the heat and particle transport is primarily directed onto the target plate, the detachment threshold is heavily influenced by the plasma density, neutral densities and recycling fluxes at the target plate, which can be enhanced by reducing cross-field particle transport (D_{leg}) in high recycling fraction scenarios.

5.4.3 HFS:LFS power split

In order to access the I-mode confinement regime, a slightly unbalanced double-null equilibrium is found to be required [99, 181], suppressing the formation of H-mode. As a result, the

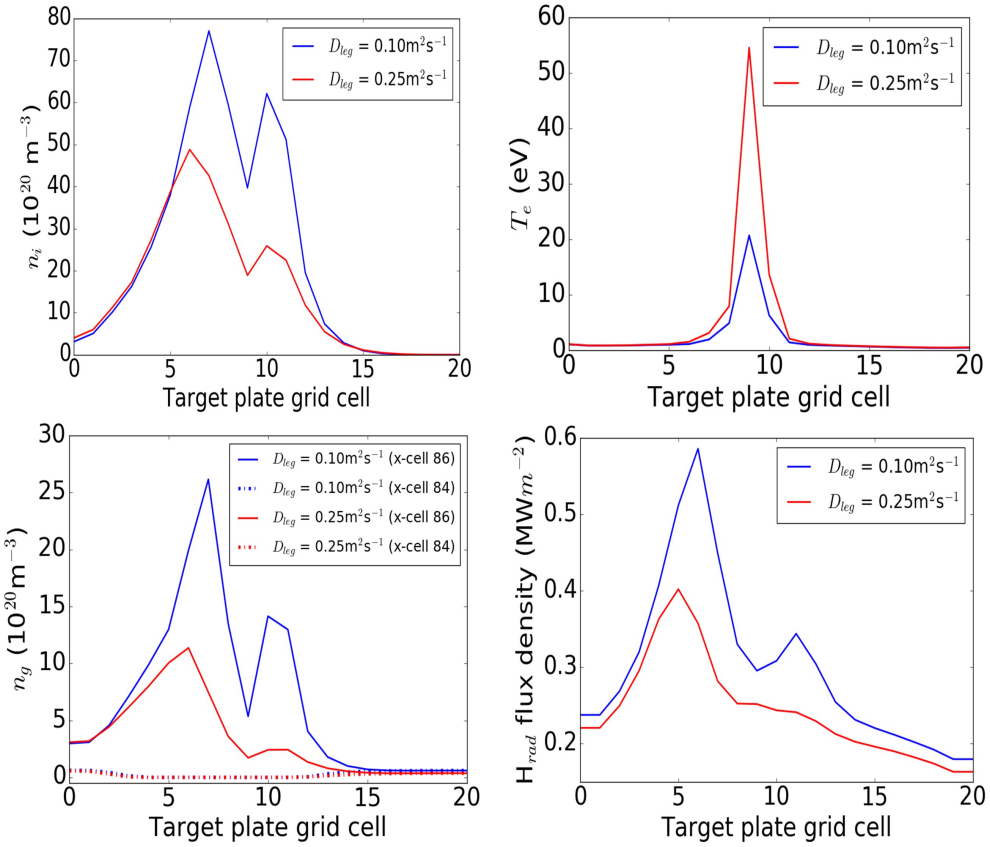

Figure 5.19: Plots of (upper-left) n_i at the target plate (x-cell=86), (upper-right) T_e at the target plate, (lower-left) n_g at the target plate and two cells away from the target (x-cell=84) , and (lower-right) hydrogenic radiation power flux density on the target plate, for D_{leg} values of 0.1 m^{2}s^{-1} (blue) and 0.25 m^{2}s^{-1} (red).

assumed HFS:LFS power split of 10:90 based on a balanced double null configuration may be overly optimistic. Moreover, loss of control of the double-null flux balance could result in an increase in power delivered to the HFS region and the inner divertor target. To test how ARC may perform in such a scenario, power splits of 15:85 and 20:80 are investigated for the 0.57 mm separation XPTD grid, n_{sep} = 1.17x10^{20} m^{-3} case from Section 5.4.1 at the full P_{SOL} = 105 MW base value, by adjusting the depth of the $\chi_{i,e}$ transport barrier on the HFS.

The peak plate temperature on the outer and inner divertor targets for the three HFS:LFS power splits investigated are plotted in Figure 5.20. Across the HFS:LFS ratio scan, the outer target moves from an attached to detached state, whilst the inner target remains detached throughout. However, calculating the peak power fluxes to these boundaries (Figure

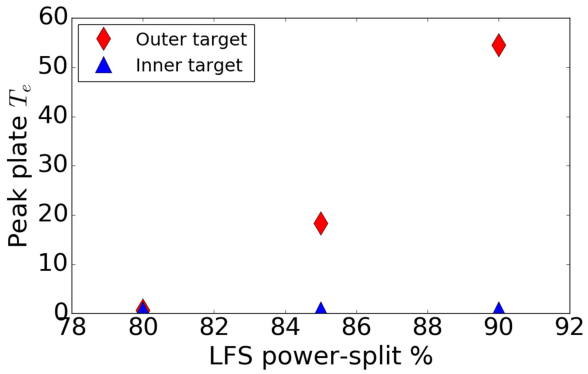

Figure 5.20: Plot of peak plate temperature (eV) at the inner and outer divertor targets for power split ratios of 10:90, 15:85 and 20:80.

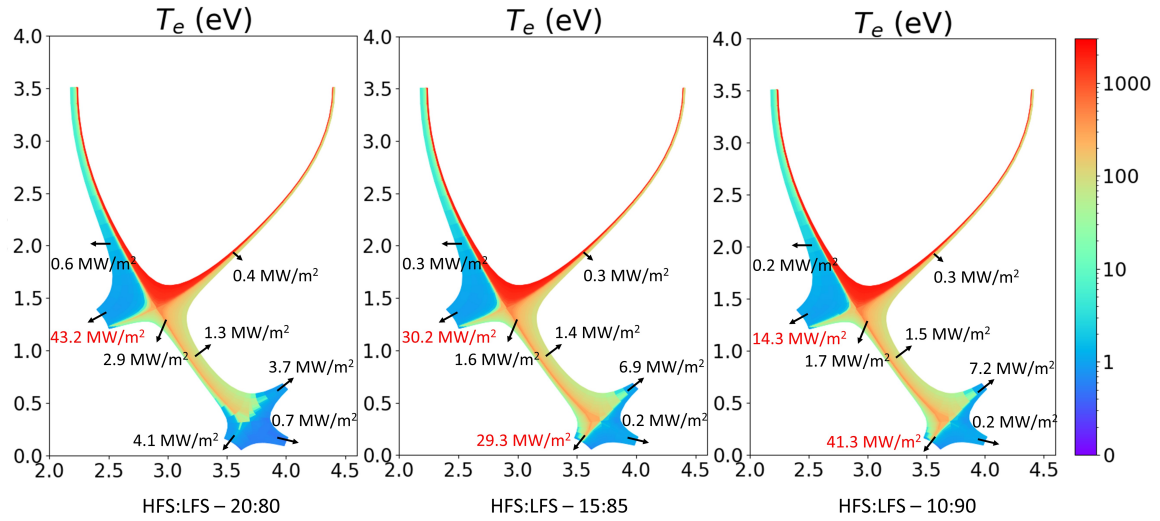

Figure 5.21: Peak power flux densities to domain boundaries for the P_{SOL} = 105 MW, n_{sep} = 1.17x10^{20} m^{-3} solutios with HFS:LFS power exhaust splits of 20:80 (left), 15:85 (middle) and 10:90 (right).

5.21), we see the peak power flux in all cases for the inner divertor target is above the 10 MWm^{-2} limit, despite remaining detached. The peak power flux at the inner target increases by a factor of ∼3 for the 20:80 power split ratio compared to 10:90 split. The low plate temperature, detached state at this plate appears to be maintained by extremely high plasma and neutral density in the cells directly above the plate, radiating much of the exhaust power as hydrogenic radiation. In UEDGE, the photon radiation impacting the plate surface is not included in the target plate temperature calculation, which would lead to some error in these values when radiated power is high, and this in part explains how such low target temperatures are maintained by the code despite high total target power fluxes

(which sum plasma/neutral/radiation loadings). This raises questions about the validity of these solutions at the inner divertor target, and more attention may need to be given to the modelling in this region.

5.5 Discussion

5.5.1 Long-legged divertor performance

This initial performance assessment of SXD and XPTD divertor configurations for the ARC reactor concept is very encouraging – notwithstanding the approximations and simplifications used in the UEDGE simulations. Stable, detached solutions for both the SXD and XPTD grids were obtained at high core exhaust power - in some cases with parallel heat fluxes entering into the divertor of $q_{||} \sim 15$ GW m^{-2} and heat flux widths of $\lambda_{q||} \sim 0.4$ mm, consistent with the anticipated heat flux width for ARC based on empirical scalings.

5.5.2 SXD

With assistance from the divertor radiation associated with a 0.5% Ne fixed impurity fraction, the SXD was able to achieve stable, fully detached divertor conditions with acceptable first wall power flux loading at the target ARC exhaust power value, $P_{SOL} = 105$ MW, and a power flux width of $\lambda_{q||} \sim$0.55 mm measured at the entrance to the divertor. Reducing $\lambda_{q||}$ to 0.4 mm will likely require an increased level of impurity seeding to handle the same power. On the other hand, the leg length of the SXD model mesh did not fully utilize the space available in ARC (see Figure 5.1); extending the leg may provide the necessary performance enhancement. The detached divertor solution identified here relies on the formation of a high-intensity Ne radiation front, which forms directly above the target plate. Peak emissivities on the order of ∼850 MW m^{-3} are observed in the simulation, leading to radiant power loads of ∼6 MW m^{-2} to the target plate, which may be acceptable.

Also associated with Ne seeding is an hysteresis effect observed in the relationship between exhaust power and onset of divertor detachment. While this result is not unexpected, it points to a challenging engineering problem. Detached solutions obtained at the highest power, i.e., the "cold branch solutions" were accessed here by starting from detached solutions at low power and growing them to high power - taking a path through parameter space (e.g. impurity seeding fraction) that maintained plasma detachment. Once the divertor reattached

at the highest powers, the detached state could not be easily regained; it required reducing P_{SOL} to very low power. If this situation is realized in a reactor, power exhaust transients that are able to burn through the detached state would need to be entirely eliminated, and/or a robust mitigation strategy would need to implemented so as to promptly regain divertor detachment and avoid divertor damage.

5.5.3 XPTD

This UEDGE modelling assessment shows that a secondary X-point in the divertor leg has potential to significantly enhance divertor performance relative to the SXD case. The base case for the XPTD was set up to be identical to the impurity-free SXD case, except that, due to enhanced grid resolution around the separatrix in the narrowest X-point separation cases, $\lambda_{q||} \sim 0.4$ mm was obtained in the model. Two effects emerge as the magnetic separation between main X-point and divertor X-point flux surfaces, s_x, is reduced: (1) slight increase in divertor detachment power threshold and (2) significant decrease in divertor target electron temperatures under attached divertor conditions, by almost a factor of 10.

An increase in divertor detachment power threshold with decreasing s_x for the XTPD was expected based on previous work using ADX parameters [60, 112]. However, the ARC cases studied thus far have not obtained the factor of ∼2 enhancement in detachment power threshold seen between the SXD and XPTD in the ADX cases - only a 25-50% enhancement is obtained here (Figure 5.8). This can be attributed to the fact that the X-point separation distance, s_x, normalized to $\lambda_{q||}$ was explored only over the range of $s_x/\lambda_{q||} \sim 3.1$ - 1.4, while the ADX study [112] had $s_x/\lambda_{q||}$ ∼0.7. The lack of a factor of 2 enhancement is therefore consistent with the expectation that the secondary X-point should have maximal impact when it most fully intercepts the parallel heat flow channel.

The trend of a decreasing attached divertor target electron temperature with decreasing $s_x/\lambda_{q||}$ (Figure 5.9) also hints that there may be a large gain in divertor detachment power threshold once $s_x/\lambda_{q||}$ is decreased to ∼1. However, the physics that drives this trend appears to be related to the role that the divertor X-point plays in splitting the power channel in to two and narrowing the primary power channel (Figure 5.10). Further study is needed.

With upstream separatrix density elevated above the reference value (1x10^{20} m^{-3}) to 1.5x10^{20} m^{-3}, the performance of the XPTD is projected to be quite impressive - fully accommodating the ARC exhaust power without any impurity seeding. As far as the author

is aware, this is the first time an impurity-free divertor power handling scenario has been obtained in edge modelling for a tokamak fusion reactor. In view of the potentially dangerous hysteresis effect seen in the detachment power thresholds for the Ne-seeded SXD cases, it may be necessary to operate these divertor configurations with very low or no divertor impurity seeding. In this regard, the identification of a divertor scheme that can successfully operate this way is essential. Needless to say, such a scenario would also be highly beneficial for optimizing the plasma core - reduced core impurity line radiation, reduced Z_{eff} and bremsstrahlung radiation, and reduced fuel dilution. In addition, there are questions surrounding I-mode and its ability to reach detachment via impurity seeding, with recent results from Reinke [139] showing a back-transition to L-mode with the introduction of seeded impurities in the divertor - therefore impurity-seeded-free detachement may in fact be necessary for the I-mode confinement regime.

The insensitivity of the modelling results to the assumed magnitude and mix of convective versus diffusive cross-field particle fluxes in the divertor leg (Section 5.3) is encouraging, accommodating a factor of ∼4 or more variation in the magnitude of each (Figure 5.15). Nevertheless, until experiments can provide definitive data on these parameters - and at the plasma conditions that are projected for the ARC divertor (e.g. plasma density, temperature, neutral densities, heat fluxes) - there will always be uncertainty in these types of model projections.

In summary, this initial performance assessment of the XPTD concept for ARC is very encouraging, and motivates further continued studies for the XPTD configuration and ARC divertor, in particular for the regime $s_x/\lambda_{q||} < 1.4$.

5.5.4 Model improvements and opportunities for further study

5.5.4.1 Increasing the radial grid resolution.

Despite the encouraging results obtained, a significant caveat remains for them regarding the poor radial resolution that could be obtained in these simulations. Due to the challenging nature of the simulations with very narrow SOL widths (∼ 0.4 mm), the resulting radial grid resolution that could be obtained in these simulations was low. For the SXD and the XPTD grids with larger X-point spacings the simulations were radially under-resolved, with the LCFS resolution $\delta y > \lambda_{q||}$, leading to resolution-limited $\lambda_{q||}$ obtainable and requiring the values of the $\chi_{e,i}$ transport barrier to be altered to as the grid resolution changed. Even for

the narrowest XPTD X-point spacings, the resolution only allowed for 2-3 radial grid points to be contained within the first $\lambda_{q||}$ width. This relatively poor radial resolution may have quantitative impact on the modelling results, and it may be the case that a number of our conclusions are subject to change if greater resolution is achieved.

The key issue here was the failure of the UEDGE grid generators to successfully produce higher radial resolution grids for the ARC geometry, preventing any meaningful convergence testing from being performed in the radial dimension. In order to determine that these results are real physics and not just numerical artefacts, resolving this resolution issue should be the highest priority of any future work continuing this study for the ARC SOL. The reason behind the grid generator failures should be identified and fixed to allow progress on this issue. In addition, alternative methods could be explored for the XPTD grid generation, that allow for varying number of grid cells separating the two X-point separatrices whilst maintaining a fixed separation. This would allow for changes of grid resolution in the XPTD cases, without changing the physical situation the simulations are trying to model, enabling sensible resolution tests to be carried out in these geometries.

5.5.4.2 Exploration of reduced X-point separation normalised to $\lambda_{q||}$.

The primary goal of this study was to determine if a viable divertor solution might exist for ARC given its high projected exhaust power (93 MW in [105], assuming 35% core raditation), narrow scrape-off layer heat flux width (0.4 mm) and moderate separatrix density (1x10^{20} m^{-3}). Thus the present study was constrained to explore models in which $\lambda_{q||}$ was held fixed at 0.4 mm and, for the XPTD, to vary the distance between main X-point and divertor X-point flux surfaces, s_x. This made it impractical to explore the interesting regime of $s_x/\lambda_{q||}$ < 1.5 because the present methods used were not able to generate a viable mesh with a secondary X-point for such narrow radial grid spacings. Another approach would be fix s_x and vary $\lambda_{q||}$. This would not reproduce the ARC base-case conditions explored here but it would allow a relative performance assessment of the XTPD that sweeps a wider range $s_x/\lambda_{q||}$. In addition, the power exhaust could be adjusted so as to hold $q_{||}$ entering into the divertor fixed while $\lambda_{q||}$ is varied.

An exploration of the physics responsible for the trend of a decreasing divertor target electron temperatures in the attached state with decreasing $s_x/\lambda_{q||}$ (Figure 5.9) was beyond the scope of the present investigation; it clearly needs further study. Related to this is the

reduction in slope of the T_e versus P_{SOL} trend lines in Figures 5.7/5.8 under attached conditions for decreased values of $s_x/\lambda_{q||}$. It is not clear why the power threshold for detachment is largely insensitive to $s_x/\lambda_{q||}$ while these other parameters vary with $s_x/\lambda_{q||}$ in this regime.

It would also be interesting to examine the case when s_x is exactly zero and to explore negative values of s_x. While the former is not possible with the present version of UEDGE, the latter is. Another possibility is to add yet another X-point to the divertor leg, producing a "snowflake target divertor". But, the magnetic topology of this divertor plus the core plasma configuration is well beyond the capabilities of the present UEDGE code.

5.5.4.3 Feasibility of controlling and holding X-point separation at $s_x/\lambda_{q||}$ ~1.

Although there may be significant benefit in operating an XPTD with $s_x/\lambda_{q||}$ ~1, it remains to be determined whether this would be feasible for a plasma shape control system. For reference, an X-point separation of 1 $\lambda_{q||}$ (~0.4 mm) in poloidal flux at the outer midplane maps to a physical separation of ~10 cm at the vicinity of the X-point target. Thus the location of the divertor X-point may be required to be positioned well within 0.1 m in the ARC tokamak that has a major radius of 3.3 m. In addition, in the ARC divertor design study [105] it was identified that for the ARC XPTD geometry, approximately +/- 2% changes in the total plasma current or ~5 cm vertical/radial displacements to the core plasma would both cause the flux surface passing through the divertor X-point to change by 1 mm (~2.5 $\lambda_{q||}$) mapped to the outer midplane, which would lose the benefits of the XPTD if not adequately controlled for. Clearly the narrow $\lambda_{q||}$ presents a significant plasma control challenge for the XPTD geometry as a power exhaust solution.

5.5.4.4 Sensitivity of results to upstream transport model assumptions.

The sensitivity studies performed in Section 5.4.2 only assessed the sensitivity of the modelling results to changes in the transport model coefficients D and v_{conv} in the outer divertor leg. However, the sensitivity to the upstream transport model assumptions was not investigated in this work. The combination of transport coefficients that could produce the desired ARC upstream profiles is not unique - other potential combinations than employed here may be possible. Such a sensitivity study could seek to find alternative combinations of D, $\chi_{e,i}$ and v_{conv} that could produce the ARC midplane profiles, and repeat power scans to assess the impact of the new transport model on the results and conclusion obtained. Alternatively,

the constraints of ARC could be relaxed, and sensitivity to changing widths of $\lambda_{q||}$ and λ_n could be assessed. Such investigations were beyond the scope of this thesis, and is left for future work in modelling the ARC divertor.

5.5.4.5 Improved impurity model; inclusion of helium impurity.

The magnitude of the detachment power threshold hysteresis effect seen for the Ne seeded case could be due in part to the fixed fraction impurity model that was implemented in UEDGE. Since in this model the local impurity density is strictly proportional to local plasma density, the impurity radiation power is directly coupled to the attached/detached conditions at the target plate, and the associated fall/rise in plasma density near the plate. Implementing a multi-charge state impurity-transport model in UEDGE is the obvious next step for impurity seeded cases, both for improving the impurity radiation power estimates in the divertor and also for examining its impact on divertor detachment power hysteresis. In addition, helium as a radiating impurity species in the divertor has not been considered in the modelling thus far, despite the fact that helium ash will be present in a fusion tokamak exhaust.

5.5.4.6 Exploration of inner divertor response and potential inner divertor solutions.

In all the simulations performed the inner divertor was always detached within a few cells of the target plate, including cases in which the plasma power delivered to the HFS was set to be high, such as the case in which an 20:80 power split between inner/outer divertor targets is considered (left panel in Figure 5.21). This is because the model produced a very high plasma/neutral density near the target plate resulting in an extremely large fraction of the plasma power being radiated. It is not clear that such a situation is plausible because it has not been seen in present experiments (although present experiments do not approach the plasma pressures and parallel heat fluxes modeled here). One cannot rule out that additional physics, such as enhanced plasma turbulence, might intervene to disperse the high density and cause the inner divertor to reattach. If so, the divertor target, which is a simple flat plate design at present, may need to be redesigned to accommodate it. In any case, it is not believed that this inner divertor behavior significantly impacts the results of the outer divertor scoping study presented in this thesis.

5.5.4.7 Improved neutral model.

A simple diffusive neutral transport model was employed for these scoping studies. The use of a fluid model can be justified in this case because the neutral mean-free-path is short compared to the divertor dimensions and gradient scale lengths of plasma parameters in the divertor. The next level of model refinement would be to employ a full Navier-Stokes fluid model that includes inertial terms. Such corrections are important when plasma flows over large regions of the divertor approach sound speed velocities. Indeed such features are observed in these simulations, particularly in the region between detachment fronts and a target plate. It is unknown at this time what impact, if any, such corrections have on the divertor detachment power threshold. The use of a Navier-Stokes neutral model for these studies was considered initially but abandoned because converged solutions were not readily obtained and the numerical burden of carrying this forward would have severely hampered this initial scoping study. Ultimately, kinetic neutral models should be employed, fully resolving atomic and molecular species, and assessing the impact of this physics, if any, on the divertor power handling response.

5.5.4.8 Inclusion of neutral pumping.

Helium ash formed by D-T fusion must be continuously removed from the reactor. This is normally facilitated by pumping some small fraction of the neutral recycling flux that appears in the divertor. Our present model does not account for this; it assumes a plasma recycling coefficient of 1 on all surfaces. The next level of refinement in the model is to drop the recycling coefficient below 1 over some region of the divertor leg and re-introduce neutrals elsewhere, according to the fueling method used (e.g. gas puff, pellets). Based on results from long-legged divertor modelling for the ADX tokamak [112], and from the observed impact of recycled neutrals on the target temperature/detachment threshold in Section 5.4.2, we expect that the divertor power handling performance of both the SXD and XPTD configurations will experience some degradation as plasma recycling is reduced below unity to simulate the pumping required for helium ash removal. This needs to be quantified for ARC parameters.

5.5.4.9 Up-down asymmetries and E×B effects.

For the purposes of simplification in this scoping study, we considered perfect up-down symmetry in the boundary plasma and employed a half-domain geometry. Such a situation is clearly not realistic; there will always be a slight up-down imbalance in the geometry and/or there may be a need to operate with an up-down imbalance, such as to access an I-mode confinement regime with ∇B drift away from the primary main plasma X-point. A result of this will be an enhanced power load to the primary divertor, which can significantly impact the overall level of exhaust power that the divertors can handle. Additionally, our model does not include particle drift effects, most notably ExB drift effects, which are known to affect divertor detachment responses [140]. Hence, inclusion of drifts may have notable impact on the conclusions and quantitative results reported in this study. Further studies are needed to assess the potential impact of both these effects on the power handling limits of both the SXD and XPTD configurations under ARC parameters.

Chapter 6

Nonlocal thermal transport in the SOL

As has been demonstrated in the previous chapters, scrape-off-layer simulation codes are an important tool used for designing and assessing divertor configurations for their ability to handle the high power loads anticipated in a tokamak fusion reactor. Accurate modelling of thermal transport in these codes is therefore of vital importance for effective divertor designs. The majority of SOL codes employ local thermal transport models - where the heat flux depends only on the local temperature and temperature gradient - assuming high particle collisionality and short mean-free-path lengths relative to system scale lengths. However, for the high upstream temperatures predicted for future reactor-level fusion devices and the steep temperature gradients required in the SOL to reach low target temperatures, such assumptions of high-collisionality may well become invalid and thermal transport become 'nonlocal'. Accurately capturing the thermal transport when local conditions do not hold is a major challenge in predictive modelling of the SOL. Chapters 6 and 7 discuss nonlocal thermal transport in the tokamak SOL, and present the results of a study of nonlocality for the ITER SOL that has been performed in this work.

6.1 Kinetic nonlocal thermal transport effects in plasmas

6.1.1 Local thermal transport - Spitzer-Härm

The Spitzer-Härm theory of thermal conductivity [141] in a plasma is commonly employed to describe the thermal heat flux in the parallel direction to the SOL field lines. In the presence of an electric field and a small temperature gradient ∇T, the heat flux density $\mathbf{q}$ and the current density $\mathbf{j}$ in the plasma are given by Spitzer and Härm as:

$$\mathbf{q} = -\beta\mathbf{E} - \kappa\nabla T \tag{6.1}$$

$$\mathbf{j} = \sigma\mathbf{E} + \alpha\nabla T \tag{6.2}$$

where α, β, σ and κ are transport coefficients. In Reference [141], Spitzer and Härm compute these coefficients to determine the heat flux in the free-flowing (parallel) direction as

$$\mathbf{q}_{SH} = -\kappa_{SH}\nabla_{||}T_e - 0.71\frac{T_e}{e}j_{||} \tag{6.3}$$

where κ_{SH} is the Spitzer-Härm thermal conductivity given by

$$\kappa_{SH} = 3.2\frac{n_e T_e \tau_e}{m_e} \propto \kappa_{||0} T_e^{\frac{5}{2}} \tag{6.4}$$

where τ_e is the energy confinement time.

In deriving the thermal conductivity, Spitzer and Härm made important assumptions [141, 142], primarily:

- The electron distribution function remains approximately Maxwellian as it evolves through a temperature gradient scale - corresponding to assuming the Knudsen number $K_n = \lambda_e/L_T$ is small (where L_T is the temperature gradient scale-length and λ_e is the electron mean free path).
- The distribution function $f \approx f_0 + f_1$, with f_0 being an isotropic Maxwellian and f_1 an anisotropic perturbation, such that $f_1 \leqslant f_0$ and $O(f_1^2)$ terms can be dropped.

This first assumption is essentially a statement on locality; plasma transport must be local for Spitzer-Härm thermal conductivity to be valid. The Spitzer-Härm thermal conductivity has been shown to work well at modelling heat flux when $K_n = \lambda_e/L_T \ll 1$. In this case the

collisional mean-free-path of the electrons is small compared to the temperature-gradient length scale, $L_T = T_e/(dT_e/dx)$. The plasma can be considered as highly collisional and transport is local, depending only on the local temperature and temperature gradient at any location in the plasma.

6.1.2 Low collisionality and nonlocal thermal transport

In the presence of high temperatures and/or steep temperature gradients, the relation $\lambda_e/L_T \ll 1$ may not hold. In such a scenario the plasma can no longer be considered as highly collisional. Particles can travel long distances without exchanging energy through collisions, potentially covering distances significant on the length scale L_T.

This is of particular relevance to the plasma electrons and energy transport; the majority of the plasma heat flux is carried by electrons with a velocity ∼3-4v_{te} [143], where v_{te} is the electron thermal velocity. Since $\lambda_e \propto v_{te}^4$, these supra-thermal electrons have much longer mean-free-paths than those at the thermal average, with $\lambda_e(3v_{te}) \sim 100\lambda_e(v_{te})$. This introduces an important criterion for assessing the locality of the thermal transport in a plasma; when $K_n^{-1} = L_T/\lambda_e \gg 100$, the condition for local thermal transport of $\lambda_e(3v_{te})/L_T \ll 1$ holds. But when $L_T/\lambda_e \sim 100$ or less, then $\lambda_e(3v_{te})/L_T \sim 1$, the condition for locality is broken, and Spitzer-Härm conductivity is no longer valid. It has been shown that for $L_T/\lambda_e \sim 100$, Spitzer-Härm predictions of thermal transport no longer agree with experimental data [30].

A 1D visual representation of the underlying physical situation is given in Figure 6.1. When λ_e becomes significant in comparison to the system scale length, the supra-thermal electrons can stream from the hot upstream plasma beyond the temperature gradient ('heat front') to directly heat the cooler plasma downstream. The heat flux at any location x no longer depends on just the local temperature $T_e(x)$ and local temperature gradient $\nabla_{||}T_e(x)$, but also on conditions in distant regions of the plasma. Transport in this regime is described as 'nonlocal'. Under such conditions a fluid description of thermal transport is not valid, and a statistical, kinetic approach is required instead.

An early analysis of the effects of nonlocal transport was perfomed by Bell [29], who numerically solved for the evolution of the kinetic equation (Eq. 3.1) in the presence of a heat front in a rapidly heated plasma. Figure 6.2 shows the results for the predicted heat flux across the domain, analysed for two time-snapshots in the simulation, plotted alongside the

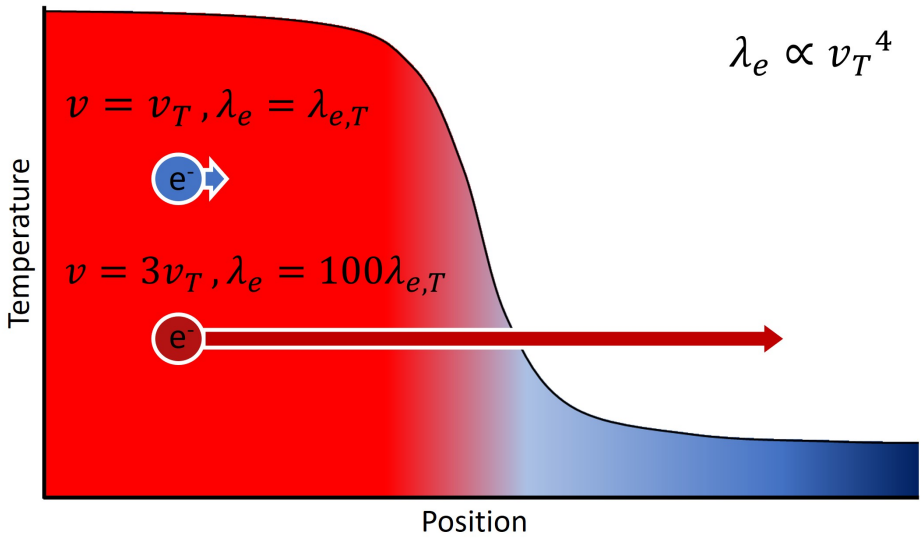

Figure 6.1: 1D illustration of nonlocal thermal transport. The plot shows a 1D temperature profile, with hot (red) and cold (blue) plasma regions. The 'cold' thermal electron (blue) has a short mean-free path, and does not leave its local plasma region before collision. The 'hot' electron (red) with $v \approx 3v_{te}$ has a much longer mean-free path, travels much further before collision, and escapes the local region to heat distant plasma beyond the heat front.

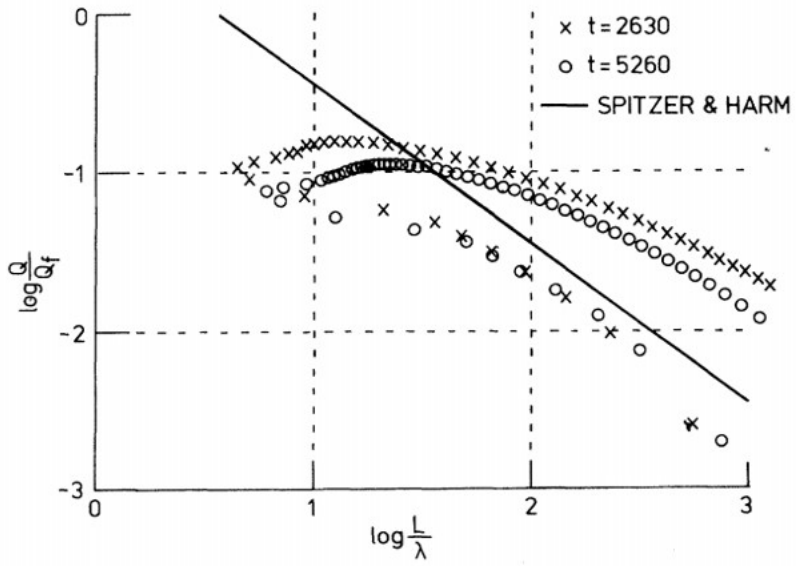

Figure 6.2: Results of kinetic Fokker-Planck modelling of thermal transport across a steep temperature gradient performed by Bell, showing a plot of $\log(Q/Q_f)$ against $\log(L_T/\lambda_e)$, where Q and Q_f are the measured and free-streaming heat fluxes respectively. The thick line shows predictions for Spitzer-Härm local theory, with kinetic simulation results plotted alongside for two simulation time snapshots. Figure reproduced from Reference [29].

predictions from Spitzer-Härm. The data reads from the bottom-right corner, corresponding to the hot plasma region upstream of the heat front, and follows the data clockwise round to the last upper-right data points for the cold region, with a steep temperature gradient between at the left-most data points. Both upstream and in the region of the heat front, the kinetic heat flux is lower than that predicted by Spitzer-Härm, giving the first nonlocal effect of 'flux-limitation'. Ahead of the front, the kinetic heat flux is increased above that predicted by Spitzer-Härm, giving the second nonlocal effect known as 'preheat'. The discrepancy between the kinetic heat flux and the Spitzer-Härm model for both of these effects can be significant in low collisionality regimes, and have a significant impact on temperature/heat flux profiles.

The issue of nonlocal thermal transport has received the most attention in the context of laser-heated plasmas relevant to inertial confinement fusion [29, 30, 147–149], but the necessary conditions can be found in SOL plasmas as well, where upstream temperatures are high and temperature gradients become steep approaching the divertor target plates [32,143]. Nonlocal effects could therefore potentially have significant impact on plasma conditions across the SOL and the divertor target, which have implications on the target plate conditions and the ability to achieve detached divertor operation. The magnitude of the divertor heat flux and target temperatures are already a concern for divertors in future high-power devices such as ITER/DEMO/ARC, and inaccuracies in the thermal transport in simulation codes used for their design could add to these concerns. If nonlocal transport effects are significant for the SOL parameters in these devices, it may prove the difference between success and failure of the power exhaust management systems. Models that seek to capture the kinetic nonlocal parallel transport in SOL simulation codes therefore deserve attention.

6.2 Capturing nonlocal effects in SOL modelling

Many methods have been proposed to capture nonlocality in simulation codes without resorting to full kinetic modelling, which is not yet feasible for realistic simulations required to assess the performance of future devices (although some progress is being made in this area [144–146]). To avoid full kinetic modelling, models that perform kinetic corrections to the local Spitzer-Härm flux, such as 'flux limiters' and 'convolution formulas', as well as 'reduced-kinetic models' that provide simplified analytical solutions to the drift kinetic

equation, are frequently applied in large simulation codes.

6.2.1 Flux limiters

The most rudimentary and commonplace nonlocal transport correction is the use of flux limiters on the electron heat flux in plasma fluid models - arbitrary limitation of the heat flux when the local Spitzer-Härm model predictions become unphysically large. There is an often assumed physical limit to the maximum heat flux that can be observed, known as the 'free-streaming flux', given as $q_{fs} = nT_e v_{te}$. Applying flux limiters to thermal transport models prevents the heat flux from exceeding a fraction α of the free-streaming limit. For transport along a magnetic field line, the parallel heat flux in flux limited models is given by the equation

$$\frac{1}{q_{e||}} = \frac{1}{q_{SH}} + \frac{1}{\alpha q_{fs}}. \tag{6.5}$$

The flux-limiter factor α can be tuned so the model fits experimental data or kinetic simulation results.

The use of flux limiters in parallel transport modelling originated in laser-plasma modelling [29, 150], and is now the most commonly applied method for nonlocality corrections used in large scale SOL modelling, despite being the most basic nonlocal correction, because of its simplicity and ease of implementation. Flux limiters are used in large scale SOL fluid codes like UEDGE [78], SOLPS [151] and EDGE2D [152]. The flux-limiter factor α is typically of the order 0.1, but can range from 0.03 to 3, depending on the plasma conditions [143]. Flux limiter models form the basis of the ITER SOL modelling and predictions, typically taking an α of 0.2, based on benchmarking with a kinetic-fluid model [22, 153].

There are significant limitations to the use of flux limiters to account for nonlocality. Flux limiters are unreliable in terms of predictive modelling; α is an *ad hoc* parameter, and values of α determined from previous experiments cannot be applied to future experimental devices, as the value is plasma conditions/device dependent. For events like Edge-Localised-Modes (ELMs), where plasma conditions change rapidly over the course of a simulation, no flux limiter can be set that is appropriate for the full range of conditions [154], and comparison with PIC simulations of the SOL show flux limiter values would need to vary in both space and time by orders of magnitude in order to model these events [155]. In addition, whilst flux limiters have proved successful in medium-range collision lengths, in long collision length

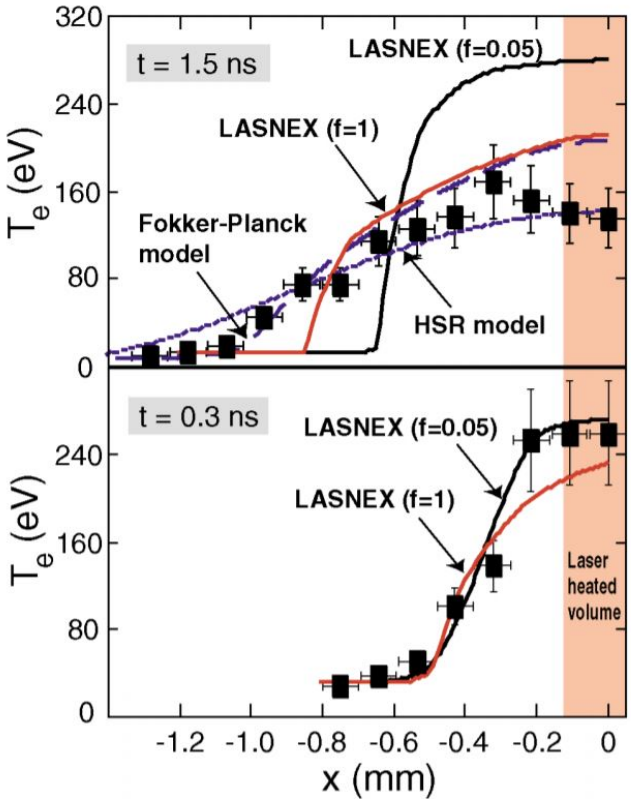

Figure 6.3: Comparison of experimental temperature data against predictions of flux-limited (LASNEX 2D fluid code), Fokker-plank and hot spot relaxation (HSR) nonlocal model predictions, at 0.3 and 1.5 ns times into the laser-heating pulse. At the earlier time, the LASNEX model with a flux-limiter factor f $(=\alpha) = 0.05$ (solid black line) reproduces the experimental data well. At the later time, no flux-limiter model matches the measured temperature profile, with models predicted too steep a temperature gradient. The Fokker-Planck (purple-dashed line) and HSR (purple-dotted line) models were found to perform better in this scenario. Figure is reproduced from Reference [158].

regimes they miss out important kinetic effects such as preheat, where flux enhancers would be needed.

Benchmarking flux limiters against kinetic codes for prediction purposes is also limited in effectiveness. The National Ignition Facility (NIF), and inertial confinement fusion experiment, was designed using electron flux limiter models for the thermal transport, using an α value determined from past experiments and from simulation codes of 0.05 [156]. The experimental results had some major discrepancies with the predictive modelling, with an updated 'High Flux Model' being required, instead implemented with an α of 0.15 [156]. The value of the flux limiter used to model NIF experiments continues to be revised even to this day [157]. It has also been found that in some cases no single flux limiter can accurately re-

produce experimental data in nonlocal conditions. Gregori *et al* [158] compared temperature profiles extracted from laser-heated plasmas experiments against flux-limited, Fokker-Planck and analytical nonlocal model predictions (Fig. 6.3). No flux-limiter model could reproduce the data taken at the later time of the pulse, producing too steep temperature gradients than experimentally observed. In this case, the Fokker-Planck and nonlocal 'hot spot relaxation' (HSR) [159] models performed much better in comparison to the data.

6.2.2 Convolution Models

Convolution formulae exist as a more sophisticated nonlocal modelling technique than flux limiters, that are simpler, more computationally efficient alternatives to solving the full kinetic equation for the distribution function, whilst still retaining the ability to model kinetic effects such as flux-limitation preheat. These models again perform as a correction to the Spitzer-Härm predictions. The general equation for convolution models is given as

$$q_{||}(x) = \beta^{-1} \int_{-\infty}^{\infty} q_{SH}(x, x') G(x, x') dx' \tag{6.6}$$

where q_{SH} is the Spitzer-Härm heat flux, $G(x, x')$ is a 'delocalisation kernel' and $\beta = \int G dx'$ is a normalisation factor [148]. The delocalisation kernel contains the information for the nonlocal transport effects, applying kinetic corrections to the local flux q_{SH} when collision lengths are long. In short collision length regimes, the models must reduce back to the uncorrected local flux q_{SH}.

The convolution method was pioneered by Luciani, Mora and Virmont [148] in their LMV model, for application to laser-plasma physics. The heat flux in the LMV model is given as

$$q_{LMV}(x) = \int_{-\infty}^{\infty} dx' \frac{q_{SH}(x, x')}{2a\lambda_e(x')} exp[-\theta(x, x')] \tag{6.7}$$

where

$$\theta(x, x') = \left| \frac{1}{a\lambda_e(x')n(x')} \int_{x'}^{x} dx'' n(x'') \right| \tag{6.8}$$

and a is a constant to be tuned. The LMV model proved to have desirable properties; it exhibited flux inhibition in the presence of large temperature gradients, it could predict preheat ahead of the heat front, and reduced to the classical Spitzer-Härm flux in the collisional limit.

Subsequent convolution models have been derived since the development of the LMV model [149, 159], showing varying degrees of success in comparison of prediction to kinetic simulations and experimental data [160]. However, these models have mostly been applied to laser-plasmas, with limited use in SOL plasmas [161]. The models become numerically very challenging to implement when the density cannot be assumed to be constant, and special care and consideration is needed when applying the model to simulations with spatial boundary conditions, both of which are true for the tokamak SOL.

6.2.3 Reduced-kinetic models

Rather than perform full kinetic modelling or exact numerical solutions to the kinetic equation in 3.1, both of which are computationally demanding, reduced-kinetic models seek to apply analytical methods to solve modified/simplified forms of the kinetic equation in order to retain nonlocal transport effects. Deriving models directly from the kinetic equation seeks more accurate reproduction of nonlocal kinetic effects in the resultant heat flux models. Reduced-kinetic models originate again in laser-plasma physics with the AWBS model [147], and a wide variety of models have been developed since then [153, 162, 163, 165, 175] that advance in sophistication and practicality. A common simplification applied is approximating the electron distribution function $f_e = f_e^{(0)} + \delta f_e$, treating it as a sum of a Maxwellian and non-Maxwellian component [147, 162, 163]. Others simplify the collision operator in the Fokker-Planck kinetic equation to Krook/BGK operators [153, 163, 175] that make the equation easier to solve. Another method has been to take a Landau-fluid approach, and treat the nonlocal heat flux as a sum of Lorentzians [166, 167]. These models have had varying success at reproducing results from experimental data and kinetic simulations [169–171].

One such reduced-kinetic nonlocal model of interest in this thesis is that first developed by Ji, Held and Sovinec [162] and then further developed by Omotani [154]. This approach solves the electron drift kinetic equation using a moment expansion of the kinetic equation in a polynomial basis, truncated to a high order of moments, and the resulting set of equations are solved as an eigenvector problem, from which the nonlocal heat flux component can be extracted. This model (which will be referred to as the 'Ji-Held' model) has been tested and compared with both kinetic codes and local flux-limited thermal transport models [169], and whilst the model has some limitations - for example being unable to predict preheat effects - it has been shown to have the advantage of reproducing flux-limited cases of varying

magnitude flux-limiter in time-dependent simulations over a range of plasma conditions [169].

Whilst the focus of reduced-kinetic models has largely been in application to laser-plasma physics problems, a number have been applied to tokamak SOL scenarios [153,154,165,175]. However, these have always been in the context of simple 1D SOL models, and so far reduced-kinetic nonlocal models have never been implemented into large scale complex SOL codes that account for the large variety of physics processes present. In addition, the studies that have been performed have focused on current devices like JET [154] and ASDEX [168], but have not yet been applied to future high-power devices such as ITER and DEMO, for which nonlocal effects will be significantly more pronounced due to the high exhaust powers and SOL temperatures anticipated. Therefore, in this thesis an assessment of the relevance of nonlocality for the ITER SOL is perfomed, by implementing the Ji-Held nonlocal model into the complex SOL code SD1D, and using the code to study the impact of incorporating nonlocal thermal transport on predictions for the ITER SOL and divertor, compared to predictions from local transport models. The Ji-Held model is further discussed in the next section, followed by details of the implementation of the model into SD1D. The results of the ITER nonlocal SOL study are then presented in Chapter 7.

6.3 The Ji-Held nonlocal model

An outline of the derivation for the Ji-Held nonlocal thermal transport model is given here; the full derivation can be found in References [154,162], and this section closely follows these references. The electron distribution function f_e is expressed as the sum of a Maxwellian part $f_e^{(0)}$ and non-Maxwellian part δf_e, such that $f_e = f_e^{(0)} + \delta f_e$. δf_e can be thought of as the nonlocal contribution - the distortion of the distribution away from Maxwellian caused by nonlocal electron transport, which is neglected in a diffusive local treatment. The stationary drift kinetic equation for a collisional plasma can then be written as:

$$v_{||}\frac{\partial\langle\delta f_e\rangle}{\partial x} = \sum_{a=e,i} C(\langle f_e^{(0)} + \delta f_e\rangle, \langle f_a^{(0)} + \delta f_a\rangle) - v_{||}\frac{\partial\langle f_e^{(0)}\rangle}{\partial x} \tag{6.9}$$

where $\langle\cdot\rangle$ denotes the gyroaverage, $v_{||}$ is the component of the velocity parallel to the magnetic field, x is the distance along the field line and $C(\cdot,\cdot)$ is the linearized Fokker–Planck collision operator.

This equation is expanded in fluid moments on the basis $P^{lk}(\frac{\mathbf{v}}{v_{te}}) = P^l(\frac{\mathbf{v}}{v_{te}})L_k^{(l+\frac{1}{2})}(\frac{v^2}{v_{te}^2})$, where $P^l(\frac{\mathbf{v}}{v_{te}})$ are tensor harmonic polynomials and $L_k^{(l+\frac{1}{2})}(\frac{v^2}{v_{te}^2})$ are associated Laguerre polynomials. The polynomial basis is typically truncated to a high order for L angular harmonics and K Laguerre orders (e.g. 20x20) such that $0 \leq l < L$ and $0 \leq k < K$, reducing the kinetic equation to a set of first-order ODEs for non-Maxwellian fluid moments:

$$\sum_B \Psi_B^A \frac{\partial n^B}{\partial z} = \sum_B C_B^A n^B + g^A \tag{6.10}$$

where the (l,k) index pairs are represented by A/B for convenience; z is a dimensionless length defined by $\frac{\partial z}{\partial x} = {\lambda_{ee}}^{-1}$ (where λ_{ee} is the electron–electron collision length); $n^{(l,k)}$ are the parallel fluid moments of δf_e,

$$\langle \delta f_e \rangle = \sum_{lk} \frac{e^{-v^2/v_{te}^2}}{\pi^{\frac{3}{2}} v_{te}^3} P_l\left(\frac{\mathbf{v}}{v_{te}}\right) L_k^{(l+\frac{1}{2})}\left(\frac{v^2}{v_{te}^2}\right) n^{(l,k)}; \tag{6.11}$$

Ψ_B^A is the matrix defined by

$$\Psi_{(l',k')}^{(l,k)} = \psi_{kk'}^l \delta_{l+1,l'} + \psi_{k'k}^{l-1} \delta_{l-1,l'}, \tag{6.12}$$

$$\psi_{kk'}^l \delta_{l+1,l'} = \frac{(l+1)}{(2l+1)(2l+3)} \lambda_{k'}^{l+1} (\delta_{k,k'} - \delta_{k-1,k'}), \tag{6.13}$$

where $\lambda_k^l = \frac{2}{\sqrt{\pi}}(l+k+\frac{1}{2})!/k!$ and δ is the Dirac-delta function; the collision matrix C_B^A is given by

$$C_{(l',k')}^{(l,k)} = \frac{\lambda_{ee}}{n_e v_{te}} \frac{1}{\lambda_{k'}^l} \left(A_{ee}^{lkk'} + B_{ee}^{lkk'} + A_{ei}^{lkk'} \right) \delta_{l,l'}, \tag{6.14}$$

where $A_{ee}^{lkk'}$, $B_{ee}^{lkk'}$ and $A_{ei}^{lkk'}$ are the moments of the electron-electron and electron-ion collision operators; and g^A is the drive term from the $\frac{\partial \langle f_e^{(0)} \rangle}{\partial l}$ component,

$$g^A = \frac{5}{4} \frac{n_e}{T_e} \frac{\partial T_e}{\partial z} \delta_{A,(1,1)}. \tag{6.15}$$

Multiplying by Ψ^{-1} $(= (\Psi_B^A)^{-1})$, Equation 6.10 becomes

$$\sum_B \frac{\partial n^B}{\partial z} = \sum_B \Psi^{-1} C_B^A n^B + \Psi^{-1} g^A. \tag{6.16}$$

The eigensystem of the matrix $\Psi^{-1} C_B^A$ can be found with eigenvectors W_A and corresponding

eigenvalues ζ_A,

$$\Psi^{-1} C_B^A W_A = \zeta_A W_A \tag{6.17}$$

Transforming Equation 6.16 to the eigenvector basis leads now to the set of decoupled ODEs

$$\frac{\partial \hat{n}^A}{\partial z} = \zeta_A \hat{n}^A + \hat{g}^A, \tag{6.18}$$

where $\hat{n}^A$ and $\hat{g}^A$ are the components of n^A and g^A on the eigenvector basis. The equations are solved in this basis as an eigenvalue problem, where the solutions can be expressed as

$$\hat{n}^A(z) = \begin{cases} -\hat{g}^A & \zeta_A = 0 \\ \hat{n}^A(z_0)\exp\left(\frac{z-z_0}{\zeta_A}\right) + \int_{z_0}^{z} dz' \exp\left(\frac{z-z'}{\zeta_A}\right) \frac{\hat{g}^A(z')}{\zeta_A} & \zeta_A \neq 0 \end{cases} \tag{6.19}$$

where $\hat{n}^A(z_0)$ are the values at the boundary z_0.

Transforming back to the original basis and selecting the (1,1) moment (giving the heat flux) gives the Ji-Held nonlocal thermal transport model:

$$q_{e||} = -\frac{5}{4} v_{T_e} T_e n^{(1,1)} = -\frac{5}{4} v_{T_e} T_e \sum_B W_B^{(1,1)} \hat{n}^B. \tag{6.20}$$

Once the boundary moments are specified (which itself is non-trivial), Equation 6.20 can then be used to calculate the nonlocal electron heat flux. In the short mean-free-path limit, Ji *et al* showed the model reduces to the Spitzer-Härm flux, and diverges for longer collision length conditions (Fig. 6.4) [162].

This model has been previously studied in a 1D SOL model, for a test case representative of a Edge-Localised Mode (ELM) crash in the JET tokamak SOL [154]. The model was shown to be able to self-consistently calculate the heat flux reduction based on plasma parameters, and respond to changes in the plasma conditions over time. It was observed that over the course of an ELM-crash the degree of flux limitation varied by up to two orders of magnitude. The flux limitation calculated by the model has also been shown to be in reasonable agreement with results from a kinetic code across a range of collisionality regimes [169].

However, these studies did not capture any of the important atomic and neutral physics that would have a significant impact on the realised heat flux, which become increasingly

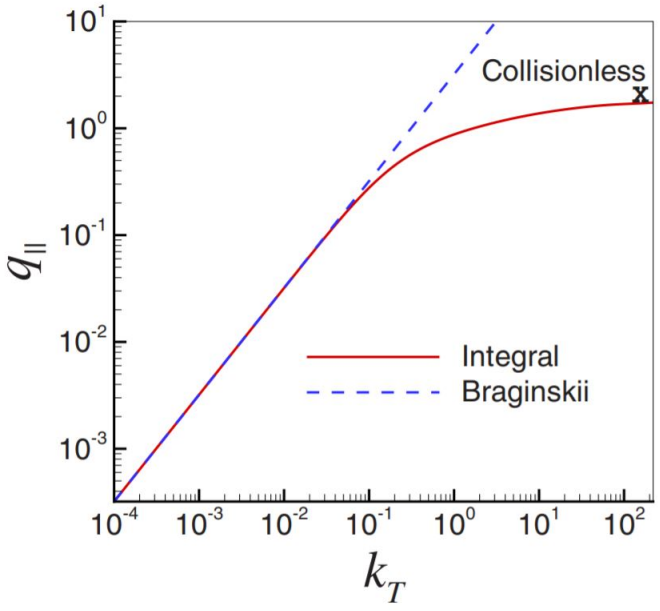

Figure 6.4: Comparison of the Ji-Held model with Braginskii closure (Spitzer), ploting heat flux prediction against collision length $k_T = 2\pi\lambda_{ee}/L_T$. For short k_T, the Ji-Held model (labelled "integral") and Spitzer models converge, but diverge for longer k_T in collisionless conditions. Figure reproduced from Reference [162].

important when modelling high-power tokamaks such as ITER. To perform the nonlocality study of the ITER SOL in this work, the Ji-Held model was implemented into the 1D SOL modelling code SD1D, that is capable of capturing these effects. The inclusion of transfer channels that capture energy/particle transfer between the plasma, neutrals, impurities, and encompassing processes such as recombination, ionisation, charge exchange, recycling etc, make SD1D a complex SOL model that goes beyond that in which the Ji-Held nonlocal transport model has previously been studied in [154].

6.4 Implementation of 'SD1D-nonlocal' code

The SD1D model (described in Chapter 3.2) calculates the heat flux component of the plasma fluid equations as

$$\mathbf{q} = \frac{5}{2} p \hat{\mathbf{b}} V_{||} - \kappa_{||e} \partial_{||} T_e \tag{6.21}$$

where the former and latter terms give the convective and conductive heat flux contributions respectively. In this study, to create the 'SD1D-nonlocal' code the conduction component in Equation 6.21 is modified to be able to perform simulations using three thermal transport

models: Spitzer-Härm, flux-limited Spitzer-Härm, and the Ji-Held nonlocal model.

- *Spitzer-Härm*: The heat flux calculation in the standard SD1D model is calculated using Equation 6.21, where the parallel conduction coefficient $\kappa_{||e}$ is given by the diffusive Spitzer-Härm model,

$$\kappa_{||e} = \kappa_{SH} = \kappa_{oe} T_e^{5/2}. \tag{6.22}$$

  where κ_{oe} is a constant given by $\kappa_{oe} = \frac{3.1\times10^4}{\ln(\Lambda)}$ (numerically determined by Spitzer and Härm [141]) and $\ln(\Lambda)$ is the Coulomb logarithm.

- *Flux-limited Spitzer-Härm*: The flux-limited (FL) model is implemented into the SD1D code by adjusting the thermal conductivity in the heat flux calculation to an 'effective thermal conductivity' term,

$$\kappa_{eff} = \kappa_{SH} \frac{1}{1 + \frac{q_{SH}}{\alpha q_{fs}}}, \tag{6.23}$$

  which is mathematically equivalent to Equation 6.5.

- *Ji-Held nonlocal model*: To incorporate nonlocal thermal transport, the latter term in Equation 6.21 was replaced to calculate the conduction component of the heat flux using Equation 6.20 for the Ji-Held model. Scripts to compute Equation 6.20 from the plasma density, temperature and velocity profiles had already been written in BOUT++ by Dr John Omotani for his JET ELM-crash study [154], and these scripts were integrated into SD1D primarily by Dr Ben Dudson. Boundary conditions in the nonlocal model are adapted to match the no-flow and sheath boundary conditions of SD1D (given in Equations 3.40 and 3.42 in Chapter 3), which impose these condition on the boundary moments. A notable difference in implementation of the sheath boundary is that the Spitzer and FL models employ zero-gradient Neumann conditions for T_e at the boundary, whereas the SD1D-nonlocal code employs a constant-gradient Neumann condition which is instead applied to $\log(T_e)$, preventing negative guard cell T_e in the case of low target temperatures.

Convergence testing and comparison with kinetic code results for the Ji-Held model and Omotani's implementation of it has been performed in previous studies with the model

[154, 162, 169]. As a check on the successful integration of Omotani's Ji-Held model implementation into SD1D, benchmarking simulations were performed for a highly collisional SOL scenario. SD1D-nonlocal simulations were run on a 1D grid with 320 evenly-spaced grid-cells for a domain with connection length $L = 100$ m from stagnation point ($s_{||} = 0$) to divertor target, with X-point location at $s_{||} = 80$ m. The simulations were performed using 20x20 moments in the Ji-Held model using a Legendre-Laguerre basis, which has been shown to be sufficient for convergence of the nonlocal model output [154, 169]. Simulation parameters were set such that the particle source produced an upstream density of ~3.7x10^{19} m^{-3}, and power source such that the parallel power flux density at the X-point was 0.24 GW m^{-2}. High recycling fraction of 0.95 is applied at the target boundary, and the sheath transmission factor is set to 7.8. Such conditions are similar to those of 2D simulations of the ITER SOL for the 3rd/4th grid cell ring outside the separatrix for 80-100MW exhaust power, albeit at a higher upstream density and longer connection length to enforce high collisionality.

Simulations were run to steady-state, and the resulting temperature/heat flux profiles produced by running the SD1D-nonlocal code with both the Spitzer-Härm and Ji-Held heat flux models are shown in Figure 6.5. These simulation parameters produced a SOL collisionality $\nu^*_{SOL} = L/\lambda_e$ of ~170, indicating a SOL that is highly collisional. Under such conditions the results from the Ji-Held model should reduce to be the same as for Spitzer-Härm. This is indeed observed in these test simulations, with the simulation outputs converging on the same result for both models.

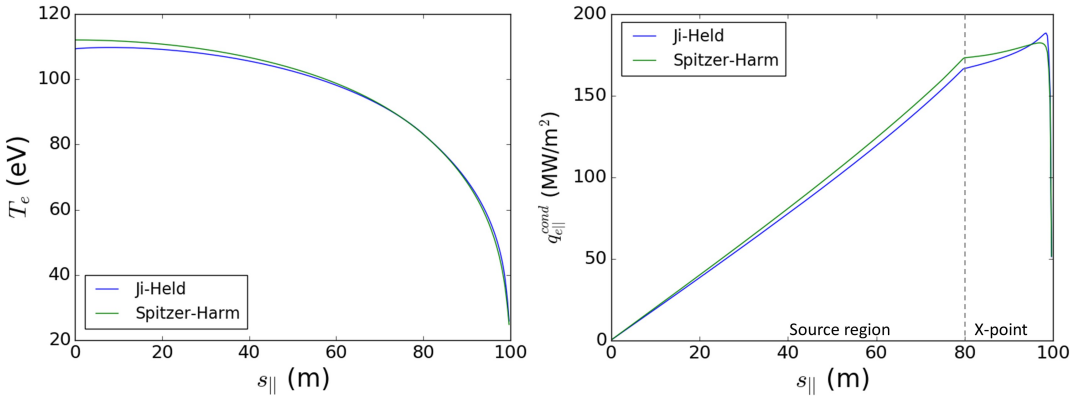

Figure 6.5: Comparison of T_e profiles (left) and $q^{cond}_{e||}$ profiles (right) across the domain using Spitzer-Härm and Ji-Held heat flux models for the benchmarking simulation conditions with upstream separatrix denstiy of $n_{sep} = 3.7$x10^{19} m^{-3}. Both models converge on the same simulation outputs for this highly collisional case.

Decreasing the input particle source so that the upstream density decreased to ~2.1x10^{19} m^{-3}, the Ji-Held and Spitzer model outputs start to significantly diverge (Fig. 6.6). The conductive heat flux remains approximately the same in both simulations, since the total power being transported through the 1D domain is fixed by the specified input power. However the calculated temperature profiles required to carry this heat flux are dramatically different between the Spitzer-Härm and Ji-Held simulation results, with an elevated temperature profile for the results using the Ji-Held model. The change in conditions reduced the collisionality of the simulations to $\nu^*_{SOL} \sim$ 55-70. For a lower collisionality, nonlocal effects would become more relevant, and so diverging outputs is in agreement with our expectations.

Behaviour showing the Ji-Held model reducing to the Spitzer-Härm output for conditions of high-collisionality, and diverging from the Spitzer-Harm results as collisionality is reduced, gives strong evidence that the Ji-Held model had been successfully integrated into the SD1D code. The SD1D-nonlocal model can now be applied to assess nonlocality in the SOL of various devices. In the next chapter, the code is applied to study high-power ITER scenarios, to assess the relevance and impact of including nonlocal thermal transport on the ITER SOL and simulation outputs.

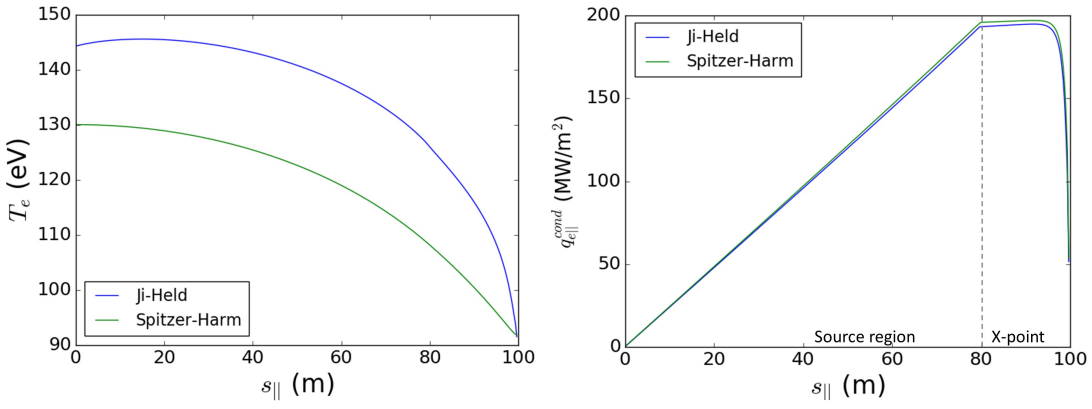

Figure 6.6: Comparison of T_e profiles (left) and $q^{cond}_{e||}$ profiles (right) across the domain using Spitzer-Härm and Ji-Held heat flux models for the benchmarking simulation conditions with upstream separatrix denstiy of $n_{sep} = 2.1\text{x}10^{19}$ m^{-3}. Whilst the conductive heat flux remains approximately the same in both simulations (due to the fixed input power through the domain), the temperature profiles required to carry this heat flux are dramatically different between the Spitzer-Härm and Ji-Held model results.

Chapter 7

SD1D-nonlocal ITER simulations

7.1 1D ITER-like tokamak

Simulations for this study were run on a 1D grid with 320 evenly-spaced grid-cells. The SD1D-nonlocal simulations were performed using 20x20 moments in the Legendre-Laguerre basis, which has been shown to be sufficient for convergence of the nonlocal model output [154, 169]. The SD1D-nonlocal code does take significantly longer to run than the standard local SD1D - running on 16 cores the SD1D model took 8-10 hours to run a real-time simulation of 40 ms for the ITER conditions used in this study, whereas SD1D-nonlocal needed 5-7 days to complete the same. This in part motivated the choice to limit the simulations to 20x20 moments and 320 grid cells, as the simulation time scales significantly for both these quantities.

Simulations were run with relevant parameters for 1D ITER steady-state conditions: upstream density set to 4.0x10^{19} m^{-3} using the density feedback controller feature in SD1D; parallel power flux density at the X-point set to 0.8 GW m^{-2}; connection length $L = 70$ m from stagnation point to divertor target (giving a spatial resolution for 320 cells of $\sim$0.22 m), with X-point location at $s_{||} = 42$ m. These parameters are consistent with 2D modelling studies of ITER with a SOL exhaust power of 100 MW and SOL e-folding length $\lambda_q = 3.5$ mm, for the first radial grid cell ring outside the separatrix [126,173]. High recycling fraction anticipated for ITER inter-ELM operation [174] of 0.95 is applied at the target boundary, with a neutral diffusion factor set to account for a $\sim 2^\circ$ field line angle with the divertor target, and the sheath transmission factor at the target is set to 7.8. No gas puffing is used for these simulations, nor is impurity seeding applied to the simulations at this point.

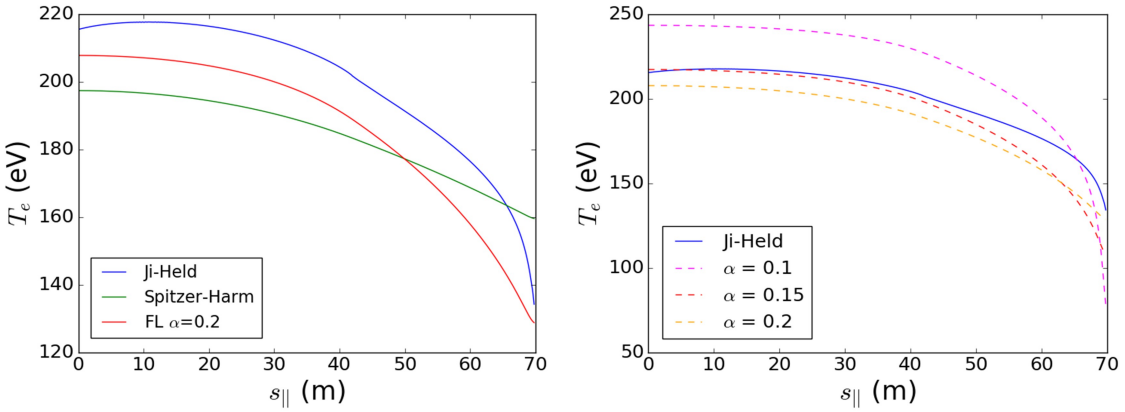

Figure 7.1: Left: SOL temperature vs SOL parallel distance for ITER-like 1D simulations using the Spitzer-Härm (green), flux-limited with α=0.2 (red) and Ji-Held nonlocal (blue) heat flux models. Right: T_e profiles for ITER-like simulations in SD1D with flux-limiters of various α values.

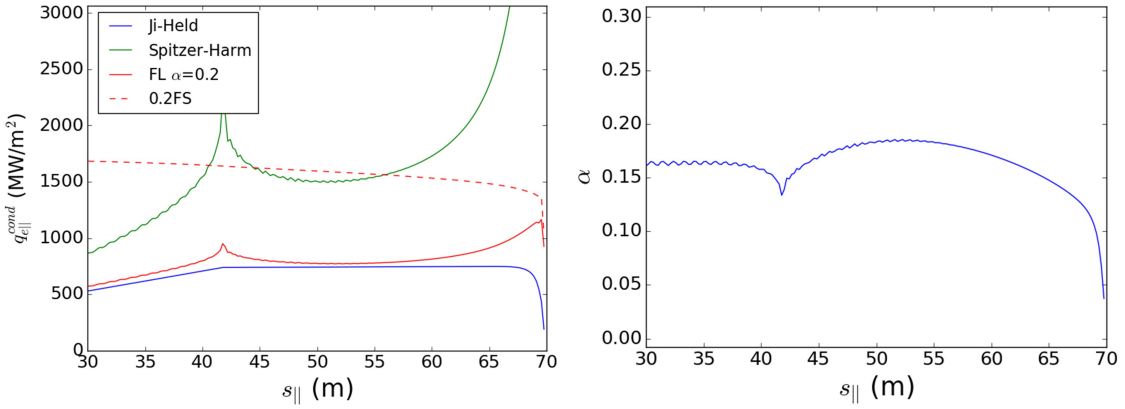

Figure 7.2: Left: $q_{e||}^{cond}$ profiles across the domain for Spitzer-Härm, flux-limited and Ji-Held heat flux models, calculated from the nonlocal model solution and T_e profile in Figure 7.1. The αq_{fs} value (labelled "0.2FS") for the plasma is plotted alongside for comparison. Right: Equivalent α value for the flux-limitation provided by the Ji-Held nonlocal model under the base ITER conditions. Noise and non-smooth features are observed in the Spitzer and flux-limited $q_{e||}^{cond}$ and α profiles, as these quantities all require calculating the value of the local Spitzer heat flux on the Ji-Held T_e profile, which the Spitzer model is not in steady-state for.

Spitzer-Härm, flux-limited Spitzer-Härm (FL) and nonlocal SD1D heat flux models were run to stationary steady-state solutions, with the FL runs performed with a flux-limit factor α of 0.2 (typical value based on kinetic simulation results [174, 175]). Particular focus in these studies will be given to comparison of the nonlocal model with the FL α=0.2 case, as this is the typical model applied for simulations of the ITER SOL in large scale fluid codes.

Resulting SOL temperature profiles for our ITER 'base-case' steady-state conditions are

shown in Figure 7.1 for each heat flux model. The electron temperature (T_e) profile from the Ji-Held nonlocal model is notably hotter across the entire domain than the FL α=0.2 model output. This difference is at a minimum at the domain boundaries, with a 5% discrepency ($\sim$10 eV) for upstream temperatures, and target boundary temperatures within 5 eV for the two models. For the region immediately in front of the divertor target ($s_{||}$= 60-68 m), the difference increases to $>$ 20 eV ($>$ 10%). This is an important region in the SOL for neutral-interactions/radiative energy losses necessary for achieving detachment, and therefore that the predicted T_e profile is notably hotter here using the nonlocal model could be a concern for the use of FL models in SOL models used for divertor designs.

Simulations for multiple flux limiter α values were performed under these ITER conditions, to determine if an equivalent global flux limiter could be used to reproduce the nonlocal model results. Profiles with some similarities could be obtained with flux-limiters (Fig. 7.1(right)), but no single flux limiter value could reproduce the nonlocal model results exactly - an α value of 0.15 closely matched the upstream temperature profile, whereas the target plate temperature was best reproduced with an α of 0.2. The region between the X-point and target boundary was not reproduced accurately by any of the flux-limiter simulations. This highlights the inadequacy of flux-limiters in accurately modelling systems with spatially-varying collisionality even in steady-state conditions, and that ITER parameters provide such a case.

For direct comparison between the three models, profiles for the conduction component of $q_{e||}$ are calculated for the Spitzer-Härm, α=0.2 flux-limited and Ji-Held heat flux models (Fig. 7.2) from the Ji-Held model solution and T_e profile in Fig. 7.1, alongside the value of αq_{fs}. An equivalent flux-limiter α value for the Ji-Held model is calculated across the domain. The Ji-Held model predicts flux-limitation for the base ITER conditions of a similar magnitude to the FL model for much of the domain, with a similar $q_{e||}^{cond}$ profile between the models and the equivalent Ji-Held α-value in the range of 0.15-0.2. However towards the target the flux-limitation increases significantly, with the $q_{e||}^{cond}$ profiles diverging and the equivalent α dropping to $<$ 0.1, as can be seen with the much steeper T_e gradient near the target, demonstrating the spatially-dependent nature of the flux-limitation with the nonlocal model.

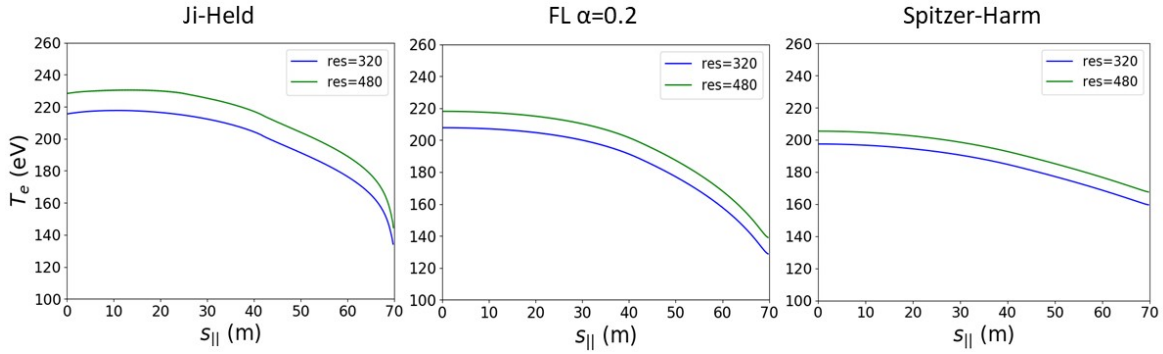

Figure 7.3: Resolution convergence testing for the ITER base-case SD1D-nonlocal simulations, using grids with 320 and 480 cells, for each of the Ji-Held, FL α=0.2 and Spitzer-Härm heat flux models.

7.1.1 Convergence testing

Convergence testing was performed with regards to the spatial grid resolution for the ITER base case simulations in Section 7.1. The number of grid cells was increased by 50% to 480 (giving a new spatial resolution of ∼0.15 m), and simulations were once again run to steady-state using the Spitzer-Härm, flux-limited and Ji-Held heat flux models. The results using each model are shown in Figure 7.3. In all case, temperatures increased consistently across the domain for the 480 cell simulations by ∼10-13 eV upstream and by ∼5-8 eV at the target, constituting a ∼5% increase in T_e across the domain. The qualitative behaviour of the results is retained despite this upwards shift in T_e. A ∼5% difference was deemed satisfactory for proceeding with the 320 cell grids in this study,when balanced with the need to complete simulation runs in the time frame of this study. However, even though the qualitative behaviour of the models appears to be captured, this observed difference in T_e over the domain indicates some level of quantitative uncertainty for the results obtained.

Convergence testing with regards to the number of moments used for the Ji-Held model was not performed - instead the work performed by Omotani [154] in testing his implementation of the Ji-Held model is relied upon in this regard. Increasing the order of truncation increases the accuracy of the Ji-Held model with respect to the with respect to the fully-kinetically calculated heat flux, and in effect extends the validity of the model to longer collision lengths [154, 162]. Omotani showed that over the range of conditions in a JET ELM simulation, results from the 20x20 and 40x40 moments Legendre-Laguerre (LL) models agreed within 2-3% of each other [154], for conditions with electron collision lengths in excess of 100 m (orders of magnitude greater than in the simulations in this study). This

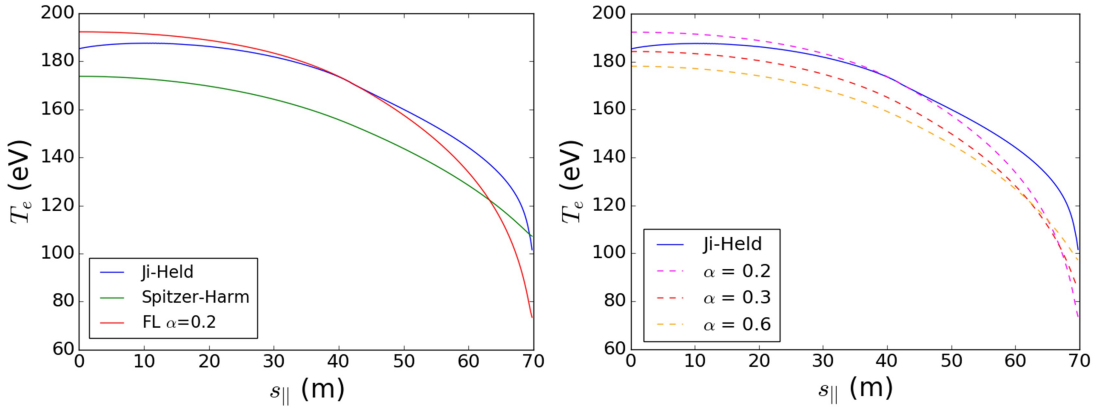

Figure 7.4: Left: Comparison of T_e profiles for SD1D and SD1D-nonlocal for ITER-like conditions for higher collisionality regime with raised upstream separatrix denstiy of $n_{sep} = 5\text{x}10^{19}$ m^{-3}. Right: T_e profiles for high collisionality ITER-like simulations in SD1D with flux limiters of various α values.

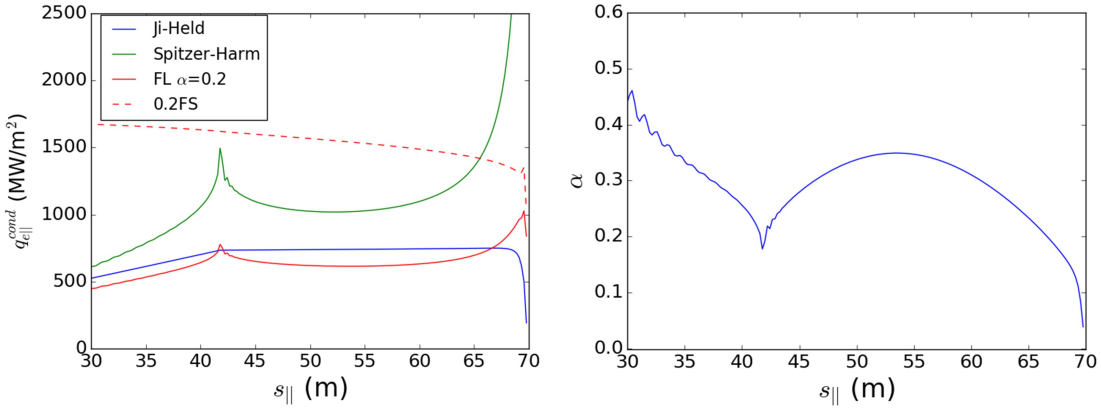

Figure 7.5: Left: $q_{e||}^{cond}$ profiles across the domain for Spitzer-Härm, flux-limited and Ji-Held heat flux models, calculated from the nonlocal model solution and T_e profile in Figure 7.4. The αq_{fs} value for the plasma is plotted alongside for comparison. Right: Equivalent α value for the flux-limitation provided by the Ji-Held nonlocal model under the lower upstream density conditions.

gives confidence in using just the 20x20 LL moments form of the Ji-Held model in this study, that significantly saves on the computational time required.

7.2 Varied ITER SOL collisionality

The upstream density conditions were varied to investigate different collisionality regimes with the nonlocal model, by increasing and decreasing the upstream density controller to values of $3\text{x}10^{19}$ m^{-3} and $5\text{x}10^{19}$ m^{-3}. These values are consistent with the range of upstream

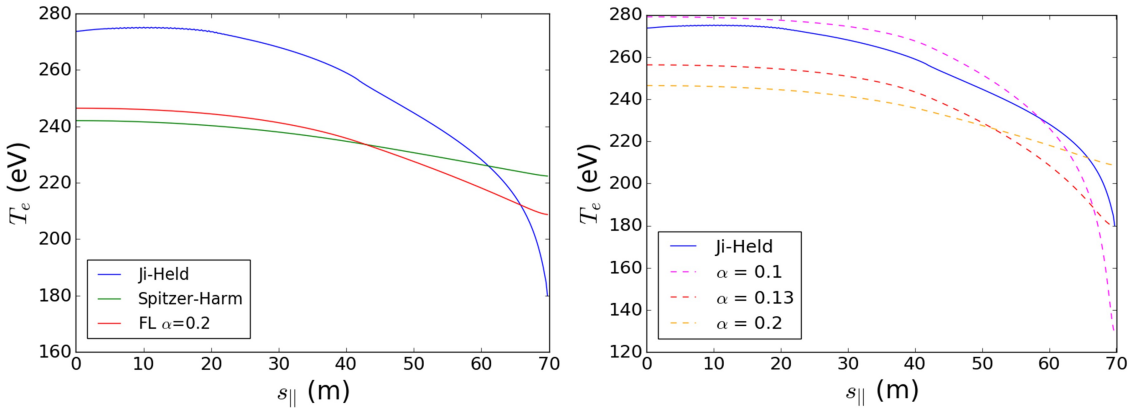

Figure 7.6: Left: Comparison of T_e profiles for SD1D and SD1D-nonlocal for ITER-like conditions for higher collisionality regime with reduced upstream separatrix denstiy of n_{sep} = 3x10^{19} m^{-3}. Right: T_e profiles for low collisionality ITER-like simulations in SD1D with flux limiters of various α values.

densities that are typically investigated for 2D ITER simulations [173]. Increasing n_{sep} to 5x10^{19} m^{-3}, a 25% increase on our ITER base scenario, the simulation output becomes less nonlocal (Fig. 7.4) as a result. There is greater agreement between the Ji-Held and FL $\alpha = 0.2$ models observed upstream, but again diverging towards the divertor target, with significantly higher target plate temperatures that have better agreement with the Spitzer-Härm output. Flux limiter simulations for various α values are performed again to identify if an equivalent global flux limiter can reproduce the nonlocal model results under these conditions. Upstream temperatures were best reproduced using flux-limiters with α in the range of 0.2-0.3, with no flux-limiter model proving able to reproduce temperatures in the divertor region. This matches well with the equivalent α value calculated for the Ji-Held model, with lower flux-limitation being predicted than for the FL $\alpha = 0.2$ model under these conditions, with the equivalent α being calculated within the range of 0.2-0.4 over the vast majority of the domain (Fig. 7.5), dropping again to < 0.1 near the divertor target.

Reducing the upstream density to n_{sep} = 3x10^{19} m^{-3} (a 25% decrease on the ITER base scenario), however, resulted in a drastically different temperature profile using the nonlocal model than for both the Spitzer and FL models. Upstream, the Ji-Held model produced a hotter T_e profile (> 30 eV) across most of domain (Fig. 7.6), before signigicantly dropping to lower T_e at the target boundary (~ 30 eV), with much steeper dT_e/ds gradients. This behaviour is in contrast to Ji-Held model outputs for the base ITER conditions and raised upstream density cases. Given ITER will not operate at a single set of plasma parameters,

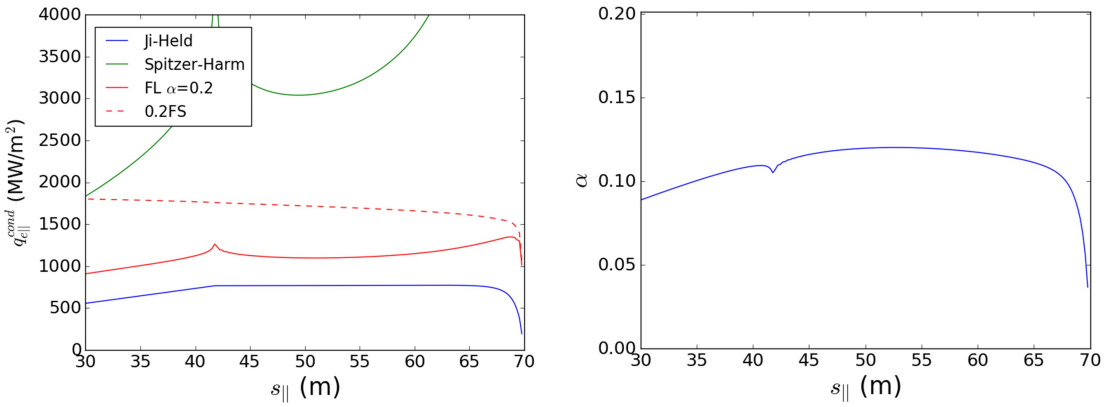

Figure 7.7: Left: $q_{e||}$ profiles across the domain for Spitzer-Härm, flux-limited and Ji-Held heat flux models, calculated from the nonlocal model solution and T_e profile in Figure 7.6. The αq_{fs} value for the plasma is plotted alongside for comparison. Right: Equivalent α value for the flux-limitation provided by the Ji-Held nonlocal model under the lower upstream density conditions.

but rather these will vary both in time and across flux surfaces, this result suggests that nonlocality could have importance in regions/regimes for the ITER SOL where the upstream density and/or SOL collisionality are low. Flux limiter simulations with various α values are performed (Fig. 7.6), with the familiar result that no single global α value can reproduce the nonlocal model, for which a spatially-varying α would be required. Plotting the $q_{e||}$ profiles for the different models and the equivalent α (Fig. 7.7) shows the Ji-Held predicts greater flux-limitation over the whole domain, with the Ji-Held model equivalent α at $\sim$0.1 until decreasing immediately before the target boundary to $\alpha \sim 0.05$.

7.3 Predicting SOL nonlocality

It would be desirable to be able to determine if a tokamak SOL will exhibit nonlocal effects without having to run a full nonlocal SOL code first, since these simulations are computationally demanding and time-consuming. In this section, we explore the potential of typical metrics for their ability to predict/assess the nonlocality of a tokamak SOL.

7.3.1 Assessing nonlocality using local temperature scalelength

One obvious candidate is the L_T/λ_e metric (the 'inverse Knudsen number' K_n^{-1}), which gives the ratio of the temperature gradient scalelength L_T and the electron mean free path λ_e. This is the typical metric used in nonlocality studies, for which $L_T/\lambda_e < 100$ is usually taken

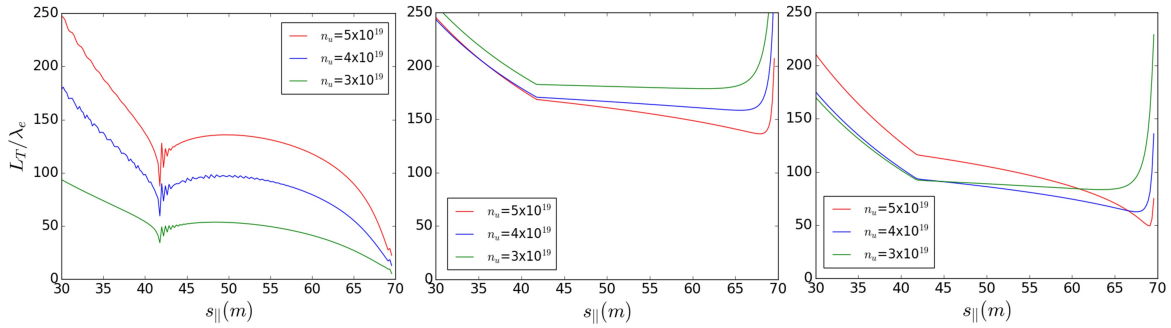

Figure 7.8: L_T/λ_e against SOL parallel distance, calculated from (left) Ji-Held, (middle) Spitzer-Härm and (right) α=0.2 flux-limited steady-state ITER solutions for the three upstream density scenarios investigated in Sections 7.1 and 7.2.

as indication that nonlocal kinetic effects would become present, as outlined in Chapter 6. In the context of the tokamak SOL, this metric will typically take its minimum value close to the divertor target, where temperature gradients are steepest. For our study, we take $\lambda_e \approx \frac{\lambda_{ee}}{\sqrt{2}}$, assuming $\lambda_{ee} \approx \lambda_{ei}$ for $T_e \approx T_i$ (where λ_{ee} and λ_{ei} are the electron-electron and electron-ion collisionlengths). Calculating the value of L_T/λ_e across the domain for the Ji-Held model solutions over the density scan (shown in Figure 7.8(left)), the minimum value of this metric notably decreases as the upstream density decreases, with minimum values of ∼30, ∼20 and ∼10 obtained for the higher density, base-case and lower density ITER scenarios respectively. This trend reflects the level of importance of nonlocality that was observed in the results in Sections 7.1 and 7.2, with increasing significance of nonlocal effects on the temperature/heat flux profiles as the SOL upstream density (and therefore overall collisionality) was decreased. In all cases, the L_T/λ_e minimum is low enough to suggest that significant nonlocal effects should be present, as was observed in the simulation results in the discrepencies of the nonlocal Ji-Held model with the local Spitzer-Härm and FL models.

As mentioned, the aim is to be able to predict SOL nonlocality without having to run the full nonlocal code, so applying the L_T/λ_e metric to the Ji-Held model outputs is not satisfactory to this end. Instead, it would be ideal if applying the metric to the outputs from codes using local thermal transport models could be used for this predictive capability. However, we find that for SOL codes with local Spitzer-Härm or FL thermal transport models and typical sheath boundary conditions, the L_T/λ_e metric is unable to predict the level of nonlocality of the SOL that would be observed in a nonlocal simulation. Calculating L_T/λ_e

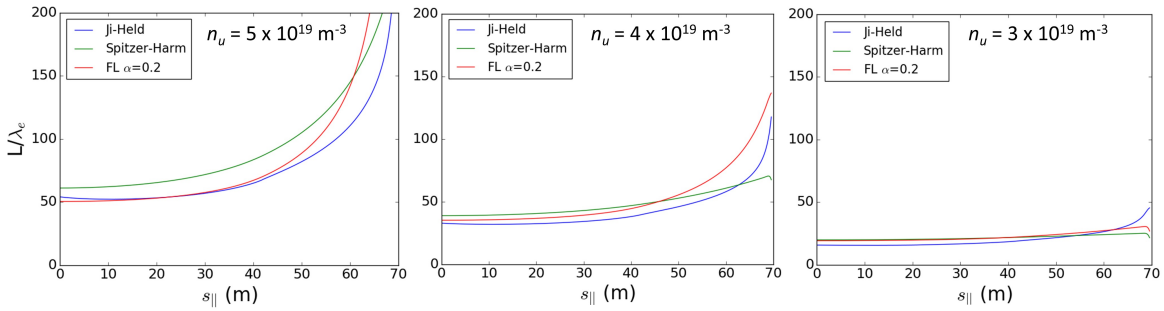

Figure 7.9: L/λ_e against SOL parallel distance, from Spitzer-Härm, flux-limited α=0.2 simulation and nonlocal model solutions, for varying upstream densities.

for the Spitzer-Härm (Fig. 7.8(middle)) and α=0.2 FL (Fig. 7.8(right)) steady state ITER solutions, the minimum value does not show the same trend of decreasing in magnitude with decreasing collisionality, and shows no obvious structure across the density cases. The lowest density case of 3x10^{19} m^{-3} appears to have the highest minimum L_T/λ_e value, and does not drop below 100 significantly at all, in contrast to the trend and high impact of nonlocality observed in the simulations. It is believed that the explanation to this lies in the interaction between the sheath boundary conditions and the thermal conduction models, and its influence on the value of L_T/λ_e in the simulation domain (an example and discussion of this is given in Appendix A). This questions the usefulness of K_n^{-1} for evaluating the potential nonlocality of a system from standard local heat flux model simulations with typical sheath boundary conditions.

7.3.2 Assessing nonlocality using connection length

An analysis is instead attempted for the SOL collisionality parameter $\nu^*_{SOL} = L/\lambda_e$. Figure 7.9 shows this value calculated across the domain under the ITER base and raised/lowered density conditions. We are only interested in the upstream value of L/λ_e for our assessment of nonlocality, both because it takes its minimum value here and because the nonlocality assessment can be grounded to the value of 100 again - if $L/\lambda_e < 100$ then the mean-free-path of the thermal-energy-carrying electrons covers the full SOL connection length. The results show a clear trend across all three thermal transport models; the raised density scenario has a minimum L/λ_e value of ~50, the ITER base scenario has a minimum of ~35, and the lowered density case has a minimum of ~20. This reflects the trend observed in the simulation results in Sections 7.1 and 7.2, with the nonlocality becoming more important as

the density decreases.

Since these results have proven to be relatively consistent across all three models, it suggests that local and flux-limited simulations can potentially be used for assessing the nonlocality of tokamak SOL conditions. Rather than running the full nonlocal model (which takes significantly longer to run than the local codes), running SOL simulations with the Spitzer-Härm or flux-limited models and then calculating the minimum L/λ_e value can be used as a rough initial assessment for whether the SOL conditions for a particular tokamak would be relevant for nonlocal transport.

A simple formula can be applied for this purpose also, if theoretical, experimental or simulation estimates of upstream temperature/density conditions and connection length are known. Inserting the definition of $\lambda_e = \beta \frac{{T_e}^2}{n_e}$ (where the constant $\beta = \frac{1.5\times10^{54}}{\sqrt{2}\ln(\Lambda)}$ and taking $\ln(\Lambda) = 15$) and adjusting the units in the terms, a formula for ν^*_{SOL} can be written as

Device	Shot no	L (m)	T_u (eV)	n_u (m^{-3})	L/λ_e
DIII-D		25	30	1.0x10^{19}	153
JET	35703	40	59.8	1.89x10^{19}	116
	35667	40	43.6	1.49x10^{19}	172
	38880	40	76.1	1.89x10^{19}	71.8
	40262	40	80.7	3.28x10^{19}	111
	40000	40	100.5	4.84x10^{19}	105
	38012	40	80.2	2.81x10^{19}	96.1
	39879	40	86.0	3.75x10^{19}	112
	38013	40	42.3	4.16x10^{19}	511
	37142	40	61.4	2.18x10^{19}	127
	37134	40	72.5	3.03x10^{19}	127
	37135	40	78.5	6.25x10^{19}	223
	37136	40	77.7	7.99x10^{19}	291
	37145	40	62.9	3.48x10^{19}	193
ITER		70	190	5x10^{19}	53.3
		70	210	4x10^{19}	34.9
		70	245	3x10^{19}	19.2
DEMO		100	300	3.0x10^{19}	18.3
ARC SXD		150	600	1.0x10^{20}	22.9

Table 7.1: SOL parameter values and calculated $\nu^*_{SOL} = L/\lambda_e$ from: DIII-D [176] and JET [177] H-mode inter-ELM data; the ITER scenarios investigated in Sections 7.1 and 7.2; predicted SOL conditions for a future DEMO [178]; and parameters extracted from the ARC SXD modelling results in Chapter 5.

$$\nu^*_{SOL} = \frac{L}{\lambda_e} = \frac{L}{\beta}\frac{n_u}{T_u^2} \approx 5.5L(\mathrm{m})\left(\frac{n_u}{10^{20}\mathrm{m}^{-3}}\right)\left(\frac{100\mathrm{eV}}{T_u}\right)^2 \tag{7.1}$$

where T_u and n_u are the upstream electron temperature/density respecitvely. Using parameters representative of the FL α=0.2 model ITER cases studied in Sections 7.1 and 7.2, the L/λ_e values estimated from this formula are 53.3, 34.9, and 19.2 for the raised density, ITER-base and lowered density scenarios respectively. These are consistent with Figure 7.9 and the relevance of nonlocality to the three cases observed in this study previously.

Equation 7.1 is applied to a typical DIII-D case [176] and JET shot data [177] for SOL parameters in H-mode (between ELMs), as well as to approximate SOL conditions predicted for DEMO [178]. Results are shown in Table 7.1 and Figure 7.10. Only one of the JET shots shown here has L/λ_e that drops notably below 100 (to 71.8), but even this case does not reach a collisionality that is comparable to any of the ITER cases investigated here (though it is stated in Ref [177] that some of the lowest collisionality cases were excluded from their analysis). This indicates why local thermal transport models have reasonable success with the modelling of these experiments. However, experiments to study nonlocal thermal transport on existing devices may be possible for lower collisionality conditions than in the JET data shown here. Nonlocality has been observed in kinetic modelling using the KIPP code for some JET H-mode discharges [179].

The predicted DEMO conditions result in a low L/λ_e of 18.3, a similar value to the ITER low density case that was studied. This similarity occurs despite DEMO having a higher upstream temperature, due to a longer connection length of a larger device which compensates. This result suggests that if nonlocal effects will have some importance for ITER conditions, as our results suggest, they will pose at least a similar level of concern for future pilot-plant reactor relevant devices like DEMO, if not greater. Nonlocal transport will almost certainly have a huge impact for modelling of ELMs/disruption events, but the results here suggest that in DEMO and lower-collisionality cases in ITER it is unlikely that nonlocal effects could be ignored even in steady-state. However, all results here were obtained under attached conditions, and whether this conclusion extends to detached divertor conditions - that future reactors will have to operate in to be feasible - is questionable.

With the modelling work that has been performed for the ARC divertor in Chapter

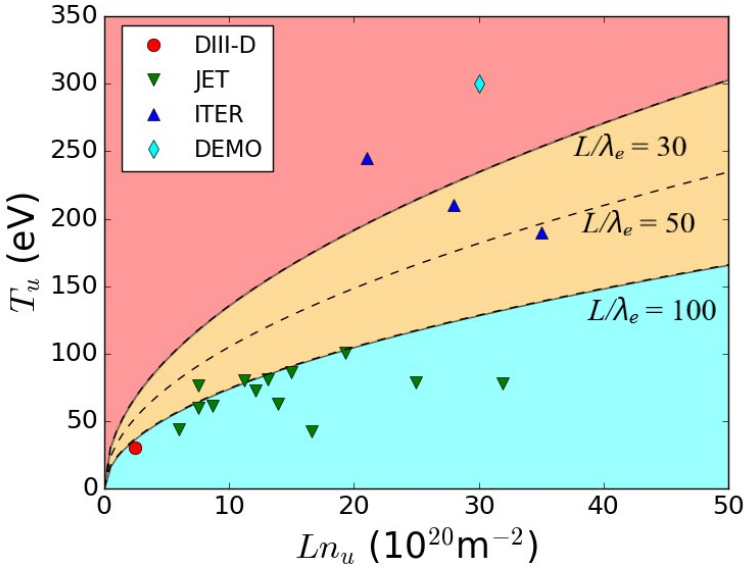

Figure 7.10: Plot of Ln_u against T_u for DIII-D [176] and JET [177] H-mode inter-ELM data, the FL α=0.2 ITER scenarios investigated in Sections 7.1 and 7.2, and predicted SOL conditions for a future DEMO [178]. Contours of $\nu^*_{SOL} = L/\lambda_e = 100$, 50 and 30 are shown.

5, these results can be used with this formula to estimate the relevance of nonlocality for the ARC SOL as well. UEDGE also applies flux-limited Spitzer conduction as the parallel thermal transport model, and in the ARC modelling studies a flux-limiter value for α of 0.2 was used. Upstream SOL temperature and density values were extracted from the Super-X Divertor (SXD) results in Section 5.2, for the 105 MW base-case scenario with zero impurity seeding. Parameters were taken from the first grid cell ring outside the separatrix, which carried the extreme power flux density of ∼10 MW m^{-2}. An estimate of the connection length from midplane to target was calculated from the divertor magnetic geometry. The resulting SOL parameters, also listed in Table 7.1, were found to be $T_u \sim 600$ eV, $n_u = 1\text{x}10^{20}$ and $L \sim 150$ m, giving a resulting ν^*_{SOL} of 22.9. This suggests a high level of nonlocality, but it is notable that it is of comparable magnitude to the values found for DEMO and the lower density ITER scenario, despite having a much higher T_u, because of the extended connection length provided by the SXD configuration. The X-Point Target Divertor (XPTD) grids in Section 5.3 further extend the connection length up to to L ∼220, a 50% increase over the SXD, which would increase ν^*_{SOL} up to 33.7 for similar upstream conditions. However, this is still a very low value, so strong nonlocal effects would still be expected to be present. The connection length would need to increase up to L∼650 in order for $\nu^*_{SOL} > 100$. These

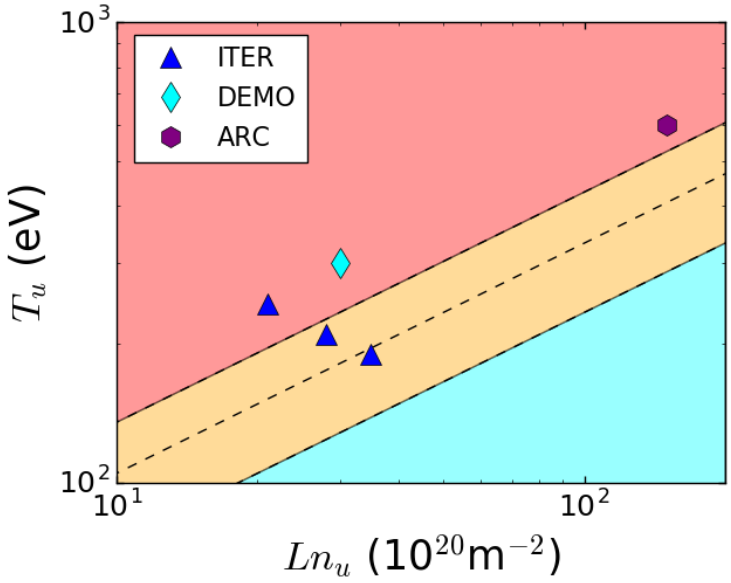

Figure 7.11: Plot of Ln_u against T_u for the FL α=0.2 ITER scenarios investigated in Sections 7.1 and 7.2, predicted SOL conditions for a future DEMO [178], and SOL parameters extracted from the ARC SXD modelling results from Chapter 5. Contours of $\nu^*_{SOL} = L/\lambda_e$ = 100, 50 and 30 are shown.

results therefore suggest that the issue of nonlocal thermal transport will be highly relevant to the ARC divertor in steady-state also, but not necessarily any greater a problem than for ITER or DEMO, despite the much smaller λ_q and higher T_u predicted for ARC.

7.4 Impurity seeding

To mitigate the high anticipated heat loads on the divertor target plate, ITER will employ impurity seeding in the SOL to induce radiation energy losses in the plasma, to lower the target plate temperature and enable detached divertor operation. To investigate the impact of nonlocal transport on code predictions with impurity seeding, simulations are repeated with a 'fixed-fraction' carbon impurity model - where impurity concentration is set at a percentage of the plasma electron density throughout the domain - aiming to reach detached conditions. Carbon impurity is used here as it was the only impurity species implemented within SD1D at the beginning of this study. It is worth noting that there will not be carbon in ITER (which has metallic plasma-facing components), so the quantitative effect of the impurity will be different than for actual ITER operation. However using carbon in this study still has value in this study to make a qualitative assessment of how radiative impurity

species impact the local/nonlocal heat flux model predictions.

Unfortunately, whilst the SD1D code could successfully model detached conditions (for which target plate $T_e < 2$ eV typically in SD1D), the SD1D-nonlocal code using the Ji-Held model was unable to do so. Many methods were attempted in order to get the Ji-Held model to model the SOL in detachment, taking different paths through parameter space, including:

- Reducing input power flux density for Ji-Held simulations to reach detachment with no impurity seeding.
- Reducing input power flux density for both Spitzer and flux-limiter simulations until converged detached solutions are obtained with no impurity seeding, and restarting the simulations using the Ji-Held model.
- Achieving detached conditions at full ITER power flux density with the FL model at 30% impurity fraction (non-stationary solution), and restarting with the Ji-Held model.
- Achieving steady-state detached solution at low power with the FL model (no impurities), then gradually increasing input power/impurity fraction in tandem to maintain the detachment, until a stationary steady-state detached solution was obtained at the full ITER power flux density with 2% impurity fraction, and restarting with the Ji-Held model.

In all cases when running SD1D-nonlocal with the Ji-Held model the code fails to reach convergence, with the CVODE solver producing a "-4" error flag - meaning the solver takes the minimum timestep size allowed and fails to converge - that aborts the code execution. From the second of these listed methods, the simulation output before the code aborts is analysed (Figure 7.12); this simulation is detached for cells 310-320, and over this region erratic behaviour for the Ji-Held heat flux calculation is observed, and a corresponding discontinuity in the T_e profile. There is clearly a numerical issue with the model calculations under these low target temperature conditions. Omotani's previous work with his Ji-Held model implementation never performed simulations in detached conditions or with low target temperatures, and it is speculated that the routines used in some of the integration calculations performed for the Ji-Held heat flux are not robust enough to handle the sharp inflection of the temperature gradient at the detachment front (around cells ∼313-315). However, no solid

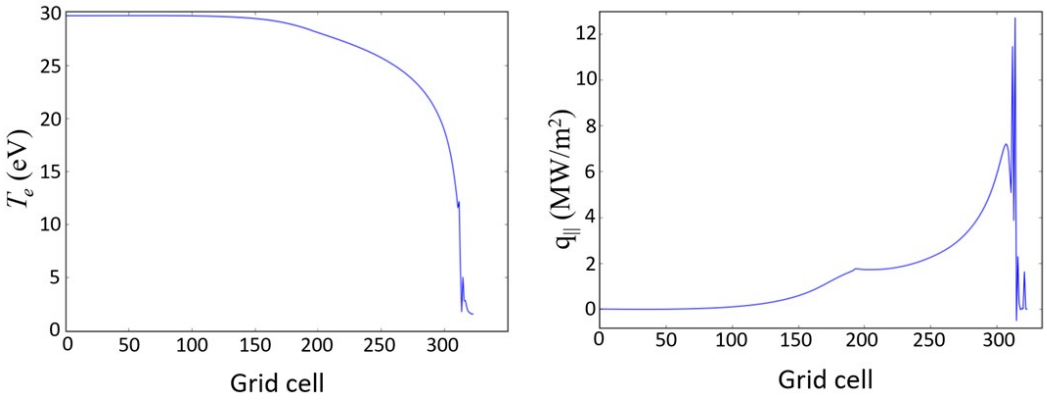

Figure 7.12: Temperature and heat flux profiles produced by SD1D-nonlocal when attempting to model detached target conditions using the Ji-Held nonlocal heat flux calculation.

conclusions on the exact nature of this problem could be determined within the timeframe of this study.

Due to these issues encountered, it was therefore not possible to do a comparison under fully detached conditions of the Ji-Held model with the local transport models, and we are forced instead to investigate differences in model outputs as detached conditions are approached, and for changes in the detachment threshold. The impurity fraction f_{imp} was steadily increased for the ITER base case scenario in Sections 7.1 to increase radiative energy losses in the SOL, once again for simulations using all three thermal transport models. Using the α=0.2 FL model, the onset of detachment occured at an impurity fraction of $\sim$28%. This is an excessively high impurity fraction - it has been estimated that a impurity fraction of 10% in the divertor volume will be required in ITER to achieve divertor detachment [180] - but this is due to: 1) using a carbon impurity in SD1D-nonlocal, whereas the 10% estimate is for nitrogen; 2) no use of target gas-puffing in our simulations to reduce target temperatures; and 3) a large hysteresis effect using the impurity model - that once lower target temperatures are obtained (for which the impurities radiate more strongly), detachment is achieved and maintained when the impurity fraction is then decreased to <5%, more in-line with the 10% estimate. Given that SD1D-nonlocal could not be run with detached conditions without crashing, this hysteresis effect could not be taken advantage of for our study, so comparisons at the higher impurity fractions ($f_{imp} > 25\%$) under attached conditions had to be used instead. For these reasons, in this study we are not concerning ourselves with the absolute value of impurity fraction required to reach detachment, but instead simply using the impurity model as a tool to disproportionately remove energy from the divertor target region, as

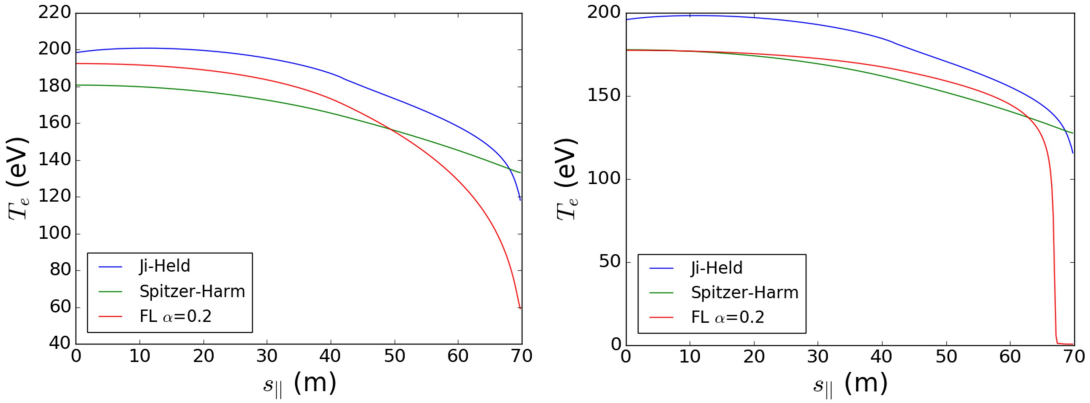

Figure 7.13: Comparison of T_e profiles for SD1D and SD1D-nonlocal for the ITER-base conditions with fixed fraction carbon impurity f_{imp} of (left) 27% and (right) 30%. All solutions shown are in steady-state besides the FL model solution for 30% impurity, for which the detachment front is moving upstream towards the X-point and at this impurity fraction eventually MARFEs.

a method to approach detached conditions and to study what happens when nonlocal heat flux and temperature-dependent impurity radiation effects are combined.

Figure 7.13(left) shows temperature profiles for the three thermal conduction models for the ITER-base scenario with an impurity fraction f_{imp}=27%. This is immediately before the FL model detaches - further increasing f_{imp} to 28% causes the target temperature to decrease below 50 eV in the FL model, where the impurities radiate much more effectively, and from there the target temperature cascade down to ∼1 eV where the plasma detaches. Significant differences between the simulation outputs at f_{imp}=27% are apparent, in particular that the target plate T_e in the FL model has decreased significantly from 130 to 60 eV between the zero impurity and f_{imp}=27% cases, but for the nonlocal model the target T_e is still high at ∼120 eV, only a 15 eV decrease from conditions without impurities (Fig. 7.1). This is despite the fact that the two models produced target temperatures within 5 eV of each other without any impurity seeding. Increasing the impurity fraction to 30% (Fig. 7.13(right)), the FL model becomes detached but both the Ji-Held model and Spitzer-Härm remain attached with very high target temperatures over 100 eV. This demonstrates a change in the detachment threshold between using nonlocal and FL models for ITER conditions - at least under the model and impurity assumptions used - which presents a potential concern for designs of divertor detachment systems on ITER.

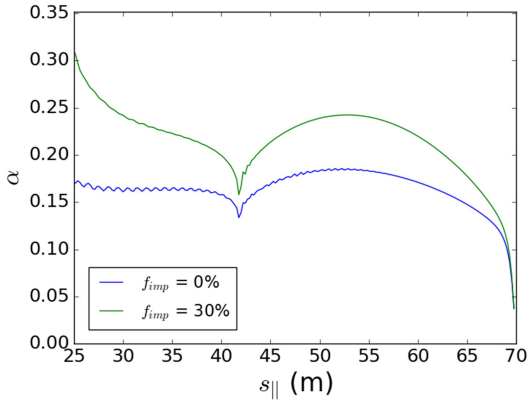

Figure 7.14: Equivalent α value for the flux-limitation given by the Ji-Held nonlocal model for the ITER base-scenario conditions for both f_{imp} = 0% and 30%. The level of flux-limitation predicted by the Ji-Held model decreases with increasing f_{imp}, with the equivalent α increasing from being predominantly in the range ~0.15-0.2 for f_{imp}=0 to >0.2 over the majority of the domain with f_{imp}=30%.

7.5 Discussion

The results in this study highlight that nonlocal thermal transport may well be important for the ITER SOL and for ITER divertor designs, with the nonlocal model implemented showing notable differences in simulation outputs compared with local thermal transport models, and showing strong sensitivity to even small changes in parameters away from the ITER base scenario. The results also highlight the inadequacy of flux-limiters in being able to accurately capture the thermal transport in conditions where collisionality varies significantly across the simulation domain, which our results suggest is relevant to ITER in steady-state. Capturing changing collisionality regimes over time is also beyond the scope of flux-limiters, for events such as ELMs or transients, which are most certainly relevant for ITER.

Particularly concerning features are the hotter temperature profiles observed for the nonlocal model in the region between the X-point and divertor target in some scenarios (Figs. 7.1 and 7.4), in particular for the base ITER scenario where the change in detachment threshold with impurity seeding is observed between transport models. These factors are likely related - with the carbon impurity radiating less effectively at higher temperatures, therefore removing less energy from the divertor region at the elevated temperatures for the Ji-Held model. In this case it could be expected that the Ji-Held model for the lower ITER density scenario (n_{sep} = 3x10^{-19} m^{-3}), which reaches lower divertor temperatures than the other models (Fig. 7.6), may instead reach detachment earlier than the FL model. However, other expla-

nations are also possible; reducing temperatures via impurity seeding and therefore making SOL conditions more collisional may result in the Ji-Held model predicting a lower level of flux limitation, with a resulting flatter temperature profile more similar to that predicted by Spitzer-Härm, which also did not detach at the 28% threshold of the FL α=0.2 model. This is indeed observed in the impurity simulations, with the equivalent α increasing as f_{imp} was increased (Fig. 7.14). In-depth analysis of the Ji-Held model dependencies would be required to identify the predominant effect here. Regardless of the underlying cause, such a discrepency as seen in Figure 7.13(right) could not be tolerated for ITER, and would cause significant damage to the divertor target if realised in practice.

It is also worth noting that the SOL conditions used in this study are representative of 2D ITER simulations with a SOL power width λ_q of $\sim$3.5 mm. The expected value of λ_q for ITER is not currently agreed amongst reseachers, and there is evidence from multi-machine scalings that λ_q could be much smaller, $\sim$1 mm or even less [21, 181]. For narrower λ_q the parallel power flux density in the SOL would significantly increase, potentially as high as $\sim$5 GW m^{-2}. Nonlocal transport effects would become even more important for the ITER SOL in such a scenario.

Modelling these scenarios in 1D is very simplified compared to 2D models, and so it is important to highlight the need for full 2D modelling with nonlocal transport in order to properly assess the impact of these effects for ITER. The results obtained in this chapter therefore motivate the study of a nonlocal transport model in 2D codes in future work: to determine if the discrepancies with Spitzer-Härm/FL models persists, or if the impact of cross field transport between flux tubes of varying collisionality reduces or removes these differences. If such discrepancies as observed in this work are also present in 2D simulations with nonlocal parallel transport, this would have impact on not only the separatrix temperature and target detachment physics, but also on cross field T_e gradients and related ∇T_e-driven turbulence and transport. In theory, the Ji-Held model could be incorporated into any 2D (e.g. SOLPS, UEDGE, EDGE2D) or 3D (e.g. GBS, HERMES, STORM, TOKAM3X) by replacing the relevant term for the parallel electron thermal conduction in the pressure/energy equation with the Ji-Held model (or other nonlocal thermal transport models). However, the factor >10 increase in simulation time to run the Ji-Held model over the Spitzer/flux-limiters found in this study limit the model's application to 2D/3D codes, which have already long computational time demands, and may cause problems in keeping

simulations running in a reasonable timeframe.

These results should be viewed in light of the nonlocal model's limitations as well. The model has previously been compared to the kinetic code KIPP in a simplified problem of large temperature gradients, and was found to underestimate the level of flux limitation in comparison to kinetic code results from KIPP [169] (Figure 7.15). That said, the fact that the Ji-Held model underestimates the flux limitation suggests that it is underestimating the importance of nonlocality in this work. This would potentially mean the discrepancies observed in the T_e profiles and detachment threshold may be further increased and be an even greater concern for ITER modelling than suggested here. This motivates further study of nonlocal models for the ITER SOL in low collisionality regimes and in the context of ELMs/disruptions. The nonlocal model also fails to reproduce any kinetic preheat effects, so only in part addresses issues for nonlocality in the SOL. The exact nature of the discrepancies observed in the simulation outputs from nonlocality may vary depending on the nonlocal thermal transport model employed, so other models that more accurately capture nonlocal flux-limitation and preheat effects should also be investigated for further SOL simulation research. The SNB model [149] is a promising candidate, which has been shown to possess these properties in Reference [169] and Figure 7.15.

In addition, appropriate boundary conditions for nonlocal thermal transport models remains a concern that needs addressing. The nonlocal model was employed with a standard sheath boundary condition given by Equation 2.20. This itself is a dubious assumption, since this condition employs assumptions of local thermal transport. In collisionless plasma conditions, streaming thermal-energy-carrying electrons from regions further away in the plasma would impact the boundary. Under such conditions the sheath electrons would be highly non-Maxwellian, making this sheath condition invalid. One potential approach to account for this is to incorporate a kinetic calculation of the sheath transmission factor γ into the code - γ has observed to vary significantly as SOL plasma conditions change in JET [179]. However, the success of this approach would be dependent on how compatible employing such a boundary condition is with the nonlocal heat flux model in question. More attention needs to be given to deriving appropriate nonlocal boundary conditions that can be used for different models based on nonlocal transport theory.

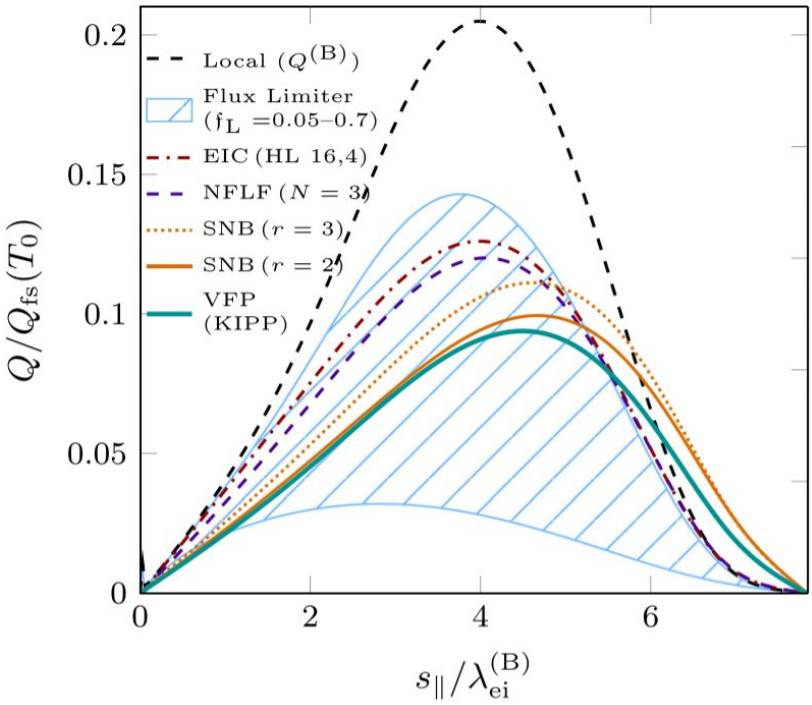

Figure 7.15: Plot of heat flux ratio Q/Q_{fs} (where Q_{fs} is the free-streaming limit $Q_{fs} = n_e T_0 v_{te}$) calculated using local and nonlocal thermal conduction models over a steep-gradient temperature profile, compared to results from the kinetic VFP code KIPP in a study by Brodrick *et al* [169]. Spitzer ($Q^{(B)}$) and flux-limited Spitzer are shown alongside Ji-Held (labelled EIC), Non-Fourier Landau Fluid (NFLF) [166], and SNB [149] nonlocal models. The Ji-Held model proves to underestimate the flux-limitation upstream compared to the kinetic KIPP results, and does not exhibit the preheat effect ahead of the heat front. The SNB nonlocal model most closely matched the KIPP code results. Figure reproduced from Reference [169] with permission from the author.

Chapter 8

Summary and Conclusions

8.1 ARC divertor modelling

The performance of long-legged, tightly baffled divertor configurations in application to the ARC fusion reactor concept [17] has been studied for the first time using the UEDGE edge plasma transport code [78]. Both Super-X divertor (SXD) [65] and X-point target divertor (XPTD) [69] configurations were explored, with the latter being the baseline divertor configuration considered for ARC [105]. Scrape-off layer (SOL) power e-folding widths ($\lambda_{q||}$) are based on empirical data [21, 181], which project to a characteristic $\lambda_{q||}$ value of 0.4 mm, mapped to the outboard midplane. A range of power exhaust was explored, accommodating the baseline operational scenario for ARC (35% core radiation, P_{SOL} = 93 MW) as well as higher power scenarios (105 MW) corresponding to peak parallel heat fluxes entering into the divertor of ∼10 GW m^{-2}. SOL density profiles were chosen to correspond to ARC's baseline I-mode scenario, with a nominal separatrix density of 1x10^{20} m^{-3} and a flattened profile in the far SOL, consistent with observations on Alcator C-Mod. The former is based on the assumption of I-mode operation to allow for the separatrix density to be equal to the edge density of the core profiles in the ARC design paper [17], and the latter required certain assumptions about the anomalous plasma transport in the far SOL, consistent with the large body of experimental data obtained on C-Mod and other tokamaks, i.e. the main chamber recycling phenomena due to non-diffusive blob transport of plasma density. It was assumed that similar diffusive and convective cross-field transport occurred in the divertor leg. Sensitivity studies revealed that divertor solutions obtained were insensitive to diffusive and convective coefficients, admitting more that factor of 4 variation in each.

Passively-stable, fully-detached divertor solutions were found for both SXD and XPTD configurations, accommodating the full exhaust power of ARC. For the SXD configurations a small neon impurity ion fraction (0.5%) was required to handle the baseline scenario with separatrix density of 1x10^{20} m^{-3}. This led to a significant hysteresis in relationship between exhaust power level and detachment power threshold ('hot' and 'cold' branch solutions), which may be a concern for handling power exhaust transients. The XPTD configuration was found to have improved power handling compared to the SXD, depending on the spacing between main plasma and divertor X-point flux surfaces. By raising the separatrix density to 1.5x10^{20} m^{-3}, passively-stable, fully-detached divertor solutions were found at X-point separations of 2 x $\lambda_{q||}$ - fully accommodating the exhaust power of ARC without the need for any impurity ion radiation at all. Solutions without impurity radiation are particularly attractive as they avoid controversial assumptions about impurity ion impacts and containment in the divertor (which is poorly understood in the present-day machines). Moreover, these solutions did not exhibit a large hysteresis effect in detachment power, making them attractive from a control point of view in which fast power exhaust transients (e.g. H-L transitions) cannot be avoided.

As the spacing between main plasma and divertor X-point flux surfaces approaches the range of 1 x $\lambda_{q||}$, further improvement in XPTD performance is evident: divertor target electron temperatures at full exhaust power (105 MW) drop by a factor of 10. This overall trend projects to the XPTD configuration attaining a passively-stable, fully detached, impurity-free scenario for X-point spacings of 1 x $\lambda_{q||}$ or less. Whilst the modelling has significant shortcomings - particularly regarding poor radial resolution in relation to $\lambda_{q||}$ and the lack of inclusion of drift effects - these results clearly motivate further study into this potentially interesting parameter range.

Overall, these results suggest that it is possible to achieve, in numerical modelling at least, benign power flux levels to plasma facing surfaces of the tightly-baffled, long-legged divertors integrated into the ARC fusion reactor design - accommodating the full level of power exhaust possible, accounting for the narrow heat flux width that is now being projected, meeting the requirements of no or low-impurity seeding levels - and doing so with a passively-stable divertor detachment response.

8.2 Nonlocal thermal transport for ITER

While much attention has been given to perpendicular transport in the SOL, relatively little has been done to improve the sophistication of parallel transport models. Reduced-kinetic models of nonlocal parallel transport provide a potential solution to addressing this problem. The 'Ji-Held' model [162] for nonlocal heat flux, previously implemented into BOUT++ by Dr John Omotani [154], has been integrated into the SD1D complex 1D SOL code [74] to create 'SD1D-nonlocal', for use in studying nonlocal thermal transport effects in the ITER SOL. Simulations were performed with the code for relevant 1D ITER steady-state parameters consistent with a 100 MW SOL exhaust power and a $\lambda_{q||} \sim 3.5$ mm [126, 173], over a range of upstream densities typically considered for simulation studies of the ITER SOL (n_{sep} = 3-5x10^{20} m^{-3}) [173]. The simulation results were compared to Spitzer-Härm and flux-limited Spitzer-Härm (FL) thermal conduction models - the standard models used in large scale SOL code - to assess the impact of including nonlocal thermal transport effects on predictions for the ITER SOL modelling. Results suggest a significant relevance of nonlocality in the ITER SOL, with notable discrepencies observed in the temperature profiles predicted by the Ji-Held model against both the Spitzer-Härm and FL models, typically showing elevated T_e profiles. Strong sensitivity in this discrepency is observed for small changes in the upstream density conditions, with much stronger divergence of the T_e profiles in the lower density ITER case studied (n_{sep} = 3x10^{20} m^{-3}). Global flux limiters were shown to be inadequate to capture the changing SOL conditions/physics across the domain, both spatially and temporally.

An analysis was performed for typical metrics used in nonlocality studies for their ability to predict/assess the nonlocality of a tokamak SOL. The 'inverse Knudsen number' $K_n^{-1} = L_T/\lambda_e$ did not correctly predict the relevance of nonlocality in the ITER simulations explored. A likely explanation is identified as the impact of the sheath boundary conditions on the SOL conditions and the resulting value of L_T/λ_e in the domain. The collisionality parameter $\nu^*_{SOL} = L/\lambda_e$ was found to have better predictive properties for nonlocality in the SOL, giving values of ν^*_{SOL} = 53.3, 34.9 and 19.2 across the ITER density cases studied using the FL model, all well below 100 and correlating with the observed relevance of nonlocality in the Ji-Held model ITER simulations. Use of this parameter suggests that nonlocal effects will also be very significant for future devices like DEMO and ARC, that had comparable values for ν^*_{SOL} of 18.3 and 22.9 respectively, for which nonlocality could not be ignored even

in steady-state.

The impact of nonlocal transport as conditions approach detachment was investigated by applying a fixed-fraction carbon impurity to the ITER simulations. Whilst the Ji-Held model proved unable to handle the low target temperatures associated with detachment, the model was able to demonstrate increasing divergence between the Ji-Held and FL model predictions as impurity fraction was increased. Despite the two models initially having target temperatures within 5 eV of each other without any impurity seeding, the FL model detached as the carbon impurity fraction was increased over 28%, whilst the Ji-Held model results maintained a target temperature > 100 eV under the same conditions. This effect is linked to less effective impurity radiation for the elevated T_e profiles using the Ji-Held model, and the reducing level of flux limitation predicted by the model as radiative losses increase the collisionality of the SOL conditions. This result presents a potential concern for designs of divertor detachment systems on ITER, if such a discrepency is observed between code predictions and experiment.

Despite the limitations of the Ji-Held model investigated, the results in this ITER SOL study provide insight to how the incorporation of nonlocal thermal transport models could impact ITER SOL simulation outputs, in particular demonstrating the potential of nonlocal transport effects to change predictions for the ITER SOL and divertor target, which are important to model accurately for divertor design and target heat flux considerations. These results therefore motivate further study into nonlocal models and for full 2D modelling with nonlocal thermal transport in order to properly assess the impact of nonlocality for ITER.

Appendix A

Effect of sheath boundary condition on L_T/λ_e metric

Calculation of the L_T/λ_e metric in Figure 7.8 did not show the expected behaviour for the Spitzer-Härm and α=0.2 FL steady state ITER solutions, with no correlation observed with decreasing collisionality and the increasing relevance of nonlocality in these runs. To gain insight into why this might be occuring in these simulations, we consider the interaction of the SOL sheath boundary condition with the local thermal conduction model.

Definitions of the terms in the L_T/λ_e metic are given as:

$$L_T = T_e/\frac{dT_e}{dx} \tag{A.1}$$

and

$$\lambda_e = \beta\frac{{T_e}^2}{n_e} \tag{A.2}$$

where $\beta = \frac{1.5\times10^{54}}{\sqrt{2}\ln(\Lambda)}$ is a constant, and $\ln(\Lambda)$ is the Coulomb logarithm. In the local Spitzer-Härm model, the electron parallel heat flux $q_{||e}$ is defined by the equation:

$$q_{||e} = \kappa_{oe}T_e^{5/2}\frac{dT_e}{dx} \tag{A.3}$$

where κ_{oe} is the plasma electron thermal conductivity. K_n^{-1} will be at a minimum where the temperature gradient is steepest, which occurs towards the divertor target. Rearranging

Equation A.3, inserting the value for $\frac{dT_e}{dx}$ into Equation A.1, and substituting values of T_e and n_e for their values at the target plate gives a new function for K_n^{-1}:

$$\frac{L_T}{\lambda_e} = \frac{\kappa_{oe}}{\beta} \frac{{T_t}^{3/2} n_t}{q_{||e}} \tag{A.4}$$

The heat flux at the target is subject to the boundary condition:

$$q_{||e} = \gamma n_t T_t c_s \tag{A.5}$$

where γ is the sheath heat transmission coefficient and the plasma sound speed c_s is given by

$$c_s = \mu \sqrt{\frac{T_t}{m_i}} \tag{A.6}$$

where μ is a constant.

Substituting these equations into Equation A.4, a value for the minimum is found to be:

$$\frac{L_T}{\lambda_e} \approx \frac{\kappa_{oe}}{\beta} \frac{\sqrt{m_i}}{\gamma \mu} = constant \tag{A.7}$$

All terms in this resulting equation are constants. Therefore, for simulations run to steady-state with conduction only using the local Spitzer-Härm heat flux model and sheath boundary condition assumptions, the minimum value of K_n^{-1} will simply be a constant, determined by the γ factor set for the target boundary. A constant value of the L_T/λ_e minimum would then not provide an indication of the degree of nonlocality of the SOL. In reality, the convective component of the heat flux and radiative losses would alter this result to not be an exact constant. But this analysis demostrates as an example how the sheath boundary can impact on the simulation results and the value for the L_T/λ_e metric, irrespective of the collisionality of the system, which undermines the use of K_n^{-1} for evaluating the potential nonlocality of the SOL.

List of References

[1] Huba J D 2016 *NRL Plasma Formulary* (Naval Research Laboratory) p44

[2] Wesson J 2004 *Tokamaks* (Oxford University Press Inc.) pp24-25

[3] U.S. Geological Survey 2019 Lithium Statistics and Information (https://www.usgs.gov/centers/nmic/lithium-statistics-and-information, accessed 4th October 2019)

[4] Hamacher T and Bradshaw A M 2001 Fusion as a Future Power Source: Recent Achievements and Prospects *18th World Energy Conference (Buenos Aires)*

[5] Wesson J 2004 *Tokamaks* (Oxford University Press Inc.) pp10-12

[6] Harms A A, Schoepf K F, Miley G H, Kindgon D R 2000 *Principles of Fusion Energy* (World Scientific Publishing Co.) pp155-159

[7] Wesson J 2004 *Tokamaks* (Oxford University Press Inc.) pp15-18

[8] De Tommasi G 2009 *J. Fusion Energy* **38** 406–436

[9] Wesson J 2004 *Tokamaks* (Oxford University Press Inc.) pp617-645

[10] Litaudon X *et al* 2017 *Nucl. Fusion* **57** 102001

[11] Keilhacker M *et al* 1998 *Nucl. Fusion* **39** 209

[12] Aymar R *et al* 2001 *Nucl. Fusion* **41** 1301

[13] Tobita K *et al* 2017 *Fusion Science and Technology* **72**(4) 537-545

[14] Kim K *et al* 2013 *Fusion Eng. Des.* **88**(6-8) 488-491

[15] G. Zhuang *et al* 2019 *Nucl. Fusion* **59** 112010

[16] Federici G *et al* 2017 *Nucl. Fusion* **57** 092002

[17] Sorbom B N *et al* 2015 *Fusion Eng. Des.* **100** pp378-405

[18] Hartwig Z S, Haakonsen C B, Mumgaard R T and Bromberg L 2012 *Fusion Eng. Des.* **87**(3) pp201–214

[19] Whyte D G *et al* 2016 *Journal of Fusion Energy* **35** 41

[20] Pitts R A *et al* 2011 *J. Nucl. Mater.* **415**(1) S957-S964

[21] Eich T *et al* 2013 *Nucl. Fusion* **53**(9) 093031

[22] Loarte A *et al* 2007 *Nucl. Fusion* **47** S203

[23] Mandrekas J *et al* 1996 *Nucl. Fusion* **36** 917

[24] Pitts R A *et al* 2009 *Phys. Scr.* **2009** 014001

[25] Kukushkin A S *el al* 2009 *Nucl. Fusion* **49**(7) 075008

[26] Zohm H *et al* 2013 *Nucl. Fusion* **53**(7) 073019

[27] Wischmeier M *et al* 2015 *J. Nucl. Mater.* **463** pp22-29

[28] Zinkle S 2005 *Fusion Eng. Des.* **74**(1-4) pp31-40

[29] Bell A *et al* 1981 *Phys Rev. Lett.* **46** pp243-246

[30] Gray D *et al* 1977 *Phys Rev. Lett.* **39** pp1270-1273

[31] Epperlein E M, Rickard G J, A R Bell A R 1988 *Phys Rev. Lett.* **61** 2453

[32] Batishchev O V *et al* 1997 *Phys. Plasmas* **4** 1672

[33] Wesson J 2004 *Tokamaks* (Oxford University Press Inc.) pp457-458

[34] Wesson J 2004 *Tokamaks* (Oxford University Press Inc.) pp466-473

[35] Ward D J and Wesson J A 1992 *Nucl. Fusion* **32** 1117

[36] Stangeby P 2000 *The Plasma Boundary of Magnetic Fusion Devices* (Taylor & Francis Group) pp17-19

[37] Stangeby P 2000 *The Plasma Boundary of Magnetic Fusion Devices* (Taylor & Francis Group) pp212-220

[38] Wagner F *et al* 1982 *Phys. Rev. Lett.* **49** 1408

[39] Stangeby P 2000 *The Plasma Boundary of Magnetic Fusion Devices* (Taylor & Francis Group) pp73-78

[40] Roth C 2012 *Nanoscale Plasma Surface Modification of Powders* (ETH Zurich) p17

[41] Self S A 1963 *Phys. Fluids* **6** 1762

[42] Stangeby P 2000 *The Plasma Boundary of Magnetic Fusion Devices* (Taylor & Francis Group) pp92-95

[43] Wesson J 2004 *Tokamaks* (Oxford University Press Inc.) pp453-457

[44] Pitcher C and Stangeby P 1997 *Plasma Phys. Control. Fusion* **39** p779

[45] Krasheninnikov S 1998 *Contr. Plasma Phys.* **38** pp293-303

[46] Matthews G F 1995 *J. Nucl. Mater.* **220–222** pp104-116

[47] Wesson J 2004 *Tokamaks* (Oxford University Press Inc.) pp413-415

[48] Huber A *et al* 2013 *Nucl. Fusion* **438** S139-S147

[49] Togo S *et al* 2012 *Plasma and Fusion Research: Regular Articles* **7** 2403087

[50] Stangeby P 2000 *The Plasma Boundary of Magnetic Fusion Devices* (Taylor & Francis Group) pp155-158

[51] Wesson J 2004 *Tokamaks* (Oxford University Press Inc.) pp195-198

[52] Wesson J 2004 *Tokamaks* (Oxford University Press Inc.) pp477-489

[53] D'Ippolito D A, Myra J R and Zweben S J 2011 *Phys. Plasmas* **18** 060501

[54] Lipshultz B *et al* 1999 *Phys. Plasmas* **6** 1907

[55] Harrison J R 2010 *Characterisation of Detached Plasmas on the MAST Tokamak* (Doctoral thesis, University of York, York, UK) p11 (accessed on 01/12/19 at https://core.ac.uk/download/pdf/1145562.pdf)

[56] Pitts R A *et al* 2019 *Nuclear Materials and Energy* **20** 100696

[57] R A Pitts *et al* 2009 *Phys. Scr.* 014001

[58] Soukhanovskii V A 2017 *Plasma Phys. Control. Fusion* **59** 064005

[59] Meier E T *et al* 2015 *J. Nucl. Mater.* **463** pp1200-1204

[60] Umansky M V *et al* 2017 *Nuclear Materials and Energy* **12** pp918-923

[61] Theiler C *et al* 2017 *Nucl. Fusion* **57** 072008

[62] Reimerdes H *et al* 2015 Towards an Assessment of Alternative Divertor Solutions for DEMO *42nd EPS Conference on Plasma Physics (Lisbon)* P4.117

[63] Brunner D, Kuang A Q, LaBombard B and Terry J L 2018 *Nucl. Fusion* **58** 076010

[64] Kotschenreuther M *et al* 2004 Scrape off layer physics for burning plasmas and innovative divertor solutions *20th IAEA Fusion Energy Conference (Vilamoura)* IC/P6-43.

[65] Valanju P M, Kotschenreuther M, Mahajan S M, and Canik J 2009 *Phys. Plasmas* **16** 056110

[66] Katramados I *et al* 2011 *Fusion Eng. Des.* **86**(9–11) pp1595-1598

[67] Ryutov D D and Soukhanovskii V A 2015 *Phys. Plasmas* **22** 110901

[68] Kotschenreuther M *et al* 2013 *Phys. Plasmas* **20** 102507

[69] LaBombard B *et al* 2015 *Nucl. Fusion* **55** 053020

[70] LaBomard B 2013 X-point Target Divertor Concept and Alcator DX High Power Density Divertor Test Facility *55th Annual Meeting of APS Division of Plasma Physics (Denver)* C04.00002

[71] Braginskii S 1965 *Reviews of Plasma Physics* **1** pp205-311

[72] Boyd T and Sanderson J 2003 *The Physics of Plasmas* (Cambridge University Press) Chapter 12.5

[73] Wesson J 2004 *Tokamaks* (Oxford University Press Inc.) pp88-93

[74] Dudson B *et al* 2019 *Plasma Phys. Control. Fusion* **61** 065008

[75] Koan M *et al* 2008 *Plasma Phys. Control. Fusion* **50** 125009

[76] Goswami R *et al* 2001 *Phys. Plasmas* **8** 857

[77] Togo S *et al* 2013 *Plasma and Fusion Research: Regular Articles* **8** 2403096

[78] Rognlien T D, Milovich J L, Rensink M E and Porter G D 1992 *J. Nucl. Mater.* **196–198** p347

[79] Rognlien T D, Ryutov D D, Mattor N and Porter G D 1999 *Phys. Plasmas* **6** p1851

[80] Rognlien T D and M.E. Rensink 2015 *Users Manual for the UEDGE Edge-Plasma Transport Code* (LLNL) (accessed on 13/11/19 at https://github.com/LLNL/UEDGE)

[81] Rognlien T D and Ryutov D D 1997 Analysis of Classical Transport Equations for the Tokamak Edge Plasma *6th Workshop on Plasma Edge Theory (Oxford)* UCRL-JC-127390

[82] Curtiss C F and Hirschfelder J O 1952 *Proc Natl Acad Sci USA* **38**(3) pp235–243

[83] Knoll D A and Keyes D E 2004 *Journal of Computational Physics* **193**(2) pp357-397

[84] Saad Y and Schultz M H 1986 *SIAM J. Sci. Stat. Comput.* **7** p856

[85] Lawrence Livermore National Laboratory *CVODE* (accessed on 13/11/19 at https://computing.llnl.gov/projects/sundials/cvode)

[86] LeVeque R 2002 *Finite Volume Methods for Hyperbolic Problems* (Cambridge University Press) p5

[87] Holm A 2018 *UEDGE-predicted impact of molecules on plasma detachment in DIII-D* (Masters thesis, Aalto University, Espoo, Finland) p26 (accessed on 01/12/19 at https://pdfs.semanticscholar.org/c781/471eab30a7c7c65d4857685dc4c03bef6577.pdf)

[88] Troyon F *et al* 1984 *Plasma Phys. Control. Fusion* **26** 209

[89] Troyon F *et al* 1988 *Plasma Phys. Control. Fusion* **30** 1597

[90] Bruzzone P *et al* 2018 *Nucl. Fusion* **58** 103001

[91] Aymar R *et al* 2002 *Plasma Phys. Control. Fusion* **44** 519

[92] Troyon 1987 *Philosophical Transactions of the Royal Society of London. Series A, Mathematical and Physical Sciences* **322** pp163-171

[93] Greenwald M *et al* 1988 *Nucl. Fusion* **28** 2199

[94] Stambaugh R D *et al* 1992 *Nucl. Fusion* **32** 1642

[95] Lee J *et al* 2017 *Nucl. Fusion* **57** 066051

[96] Whyte D G *et al* 2010 *Nucl. Fusion* **50** 105005

[97] Bécoulet M *et al* 2003 *Plasma Phys. Control. Fusion* **45** A93

[98] Hubbard A E *et al* 2017 *Nucl. Fusion* **57** 126039

[99] Hubbard A E *et al* 2017 *Nucl. Fusion* **57** 126039

[100] Stangeby P 2000 *The Plasma Boundary of Magnetic Fusion Devices* (Taylor & Francis Group) pp221-230

[101] Whyte D G *et al* 2012 *Fusion Eng. Des.* **87**(3) pp234-247

[102] Senatore C *et al* 2016 *Supercond. Sci. Technol.* **29** 014002

[103] Fischer D X *et al* 2018 it Supercond. Sci. Technol. **31** 044006

[104] Snyder P B *et al* 2019 *Nucl. Fusion* **59** 086017

[105] Kuang A Q *et al* 2018 *Fusion Eng. Des.* **137** p221

[106] Devoto R S *et al* 1992 *Nucl. Fusion* **32** 773

[107] Lackner K and Zohm H 2013 *Fusion Science and Technology* **63** 43

[108] Luxon J L 2002 *Nucl. Fusion* **42** 614

[109] Marmar E S *et al* 2007 *Fusion Science and Technology* **51**(3) pp261-265

[110] Lister J B *et al* 1997 *Fusion Technology* **32**(3) pp321-373

[111] Reinke M L 2017 *Nucl. Fusion* **57** 034004

[112] Umansky M V *et al* 2017 *Phys. Plasmas* **24** 056112

[113] Rognlien T D and Rensink M E 2002 *Fusion Eng. Des.* **60**(4) pp497-514

[114] Wising F *et al* 1996 *Contrib. Plasma Physics* **36**(2–3) pp309-313

[115] Rensink M E et al 2007 *J. Nucl. Mater.* **363–365**(1–3) p816

[116] Christem N *et al* 2017 *Plasma Phys. Cont. Fusion* **59** 105004

[117] Umansky M V *et al* 2009 *Nucl. Fusion* **49** 075005

[118] Tani K, Azumi M and Devoto R S 1992 *Journal of Computational Physics* **98** 332

[119] Devoto R S *et al* 1992 *Nucl. Fusion* **32** 773

[120] Rognlien T D *et al* 2010 Advances in Understanding Tokamaks Edge/Scrape-Off Layer Transport *23rd IAEA Fusion Energy Conference (Daejeon)* THD/P3-05

[121] LaBombard B *et al* 2001 *Phys. Plasmas* **8** 5

[122] LaBombard B *et al* 2005 *Nucl. Fusion* **45** 1658-1675

[123] LaBombard B *et al* 2000 *Nucl Fusion* **40** 12

[124] Krasheninnikov S I 2001 *Phys. Lett. A* **283** 368

[125] Dippolito D A and Myra J R 2001 *Phys. Plasmas* **9** 222

[126] Kukuskin A S *et al* 2001 *J. Nucl. Mater.* **290-293** pp887-891

[127] Harrison J M, Fishpool G M and Dudson B D 2015 *J. Nucl. Mater.* **463** pp757-760

[128] Scotti F *et al* 2018 *Nucl. Fusion* **58**(12) 126028

[129] LaBombard B *et al* 2004 *Nucl. Fusion* **44** p1047

[130] Brunner D, LaBombard B, Kuang A Q and Terry J L 2018 *Nucl. Fusion* **58** 094002

[131] Erents S K and Stangeby P C 1998 *Nucl. Fusion* **38** p1637

[132] Brunner D, LaBombard B, Kuang A Q and Terry J L 2018 *Nucl. Fusion* **58** 094002

[133] Umansky M V *et al* 1999 *Phys. Plasmas* **6** p2791

[134] Brunner D, Kuang A Q, LaBombard B and Terry J L 2018 *Nucl. Fusion* **58** 076010

[135] Kirk A *et al* 2004 *Plasma Phys. Cont. Fusion* **46**(3) p551

[136] Umansky M V, Krasheninnikov S I, LaBombard B and Terry J L 1998 *Phys. Plasmas* **5** 3373

[137] Krasheninnikov S I *et al* 1995 *Phys. Plasmas* **2** p2717

[138] Sun H J *et al* 2017 *Plasma Phys. Control. Fusion* **59** 105010

[139] Reinke M L *et al* 2019 *Nucl. Fusion* **59** 046018

[140] Hutchinson I H *et al* 1995 *Plasma Phys. Cont. Fusion* **37** 1389

[141] Spitzer L and Härm R 1953 *Physical Review* **89**(5) pp977-981

[142] Bale S *et al* 2013 *Astrophysical Journal Letters* **769** L22

[143] Fundamenski W 2005 *Plasma Phys. Cont. Fusion* **47** R163-R208

[144] Zhao M, Chankin A and Coster D 2019 *Computer Physics Communications* **235** pp133-152

[145] Churchill R M *et al* 2017 *Nuclear Materials and Energy* **12** pp978-983

[146] Tskhakya D *et al* 2013 *J. Nucl. Mater.* **438** S522-S525

[147] Albritton J *et al* 1986 *Phys Rev. Lett.* **57** pp1887-1890

[148] Luciani J F, Mora P and Virmont J 1983 *Phys Rev. Lett.* **51** pp1664-1667

[149] Schurtz G P, Nicolaï Ph D and Busquet M 2000 *Phys. Plasmas* **7** 4238

[150] Shvarts D *et al* 1981 *Phys. Rev. Lett.* **47** pp247-250

[151] Wiesen S *et al* 2015 *J. Nucl. Mater.* **463** pp480-484

[152] Radford G J *et al* 1995 *Contrib. Plasma Phys.* **38** pp183-188

[153] Kukushkin A and Runov A 1994 *Contrib. Plasma Phys.* **34** p204

[154] Omotani J and Dudson B 2013 *Plasma Phys. Control. Fusion* **55** 055009

[155] Tskhakya D *et al* 2008 *Contrib. Plasma Phys.* **48** pp89-93

[156] Rosen M D *et al* 2011 *High Energy Density Phys.* **7** pp180-190

[157] Jones O S *et al* 2017 *Phys. Plasmas* **24** 056312

[158] Gregori G *et al* 2004 *Phys. Rev. Lett.* **92** 205006

[159] Batishchev O *et al* 2002 *Phys. Plasmas* **9** 2302

[160] Epperlein E and Short R 1991 *Phys. Fluids B* **3** 3092

[161] Ciraolo G *et al* 2018 *Contrib. Plasma Phys.* **58** 457–464

[162] Ji J, Held E, and Sovinec C 2009 *Phys. Plasmas* **16**(2) 022312

[163] Manheimer W, Colombant D and Schmitt A J 2012 *Phys. Plasmas* **19** 056317

[164] Igitkhanov Y *et al* 1994 *Contrib. Plasma Phys.* **34** pp216-220

[165] Cohen R and Rognlien T 1994 *Contrib. Plasma Phys.* **34** pp198-203

[166] Dimits A M, Joseph I and Umansky M V 2014 *Phys. Plasmas* **21** 055907

[167] Hammett G W and Perkins F W 1990 *Phys. Rev. Lett.* **64** 3019

[168] Igitkhanov Yu L and Pigarov A Yu 1990 *J. Nucl. Mater.* **176–177** pp557-561

[169] Brodrick J *et al* 2017 *Phys. Plasmas* **24** 092309

[170] Sherlock M, Brodrick J P, Ridgers C P 2017 *Phys. Plasmas* **24** 082706

[171] Marocchino A *et al* 2013 *Phys. Plasmas* **20** 022702

[172] Stangeby P C 2000 *The Plasma Boundary of Magnetic Fusion Devices* (Taylor & Francis Group LLC) pp92-95.

[173] Pacher H D *et al* 2015 *J. Nucl. Mater.* **463** 591–595

[174] Loarte A *et al* 2007 *Nucl. Fusion* **47** S203

[175] Igitkhanov Y, Bazylev B and Fetzer R 2015 *The quantification of the key physics parameters for the DEMO fusion power reactor and analysis of the reactor relevant physics issues* (KIT Scientific Publishing) p75

[176] Leonard A W *et al* 2007 *J. Nucl. Mater.* **363–365** pp1066–1070

[177] Erents S K and Stangeby P C 1998 *Nucl. Fusion* **38** 1637

[178] Rubino G, Ambrosino R, Calabrò G, Pericoli Ridolfini V and Viola B 2017 *Nuclear Materials and Energy* **12** pp864–868

[179] Chankin A V *et al* 2018 *Plasma Phys. Control. Fusion* **60** 115011

[180] Goldston R J *et al* 2017 *Plasma Phys. Control. Fusion* **59** 055015

[181] Brunner D, LaBombard B, Kuang A Q and Terry J L 2018 *Nucl. Fusion* **58** 094002